INL/LTD-16-38121 R1
DE-EE0007159

The Snake River Geothermal Consortium is a research partnership focused on advancing geothermal energy, hosted by Idaho National Laboratory.

Geologic Conceptual Model

April 2016

SRG Consortium | Snake River Geothermal

FORGE U.S. Department of Energy

INL/LTD-16-38121 R1

Geologic Conceptual Model

James St. Clair, University of Idaho
Colleen Barton, Baker Hughes
William Hackett, WRH Associates, Inc.
Thomas Wood, University of Idaho
Mike McCurry, Idaho State University
Michael Janis, University of Oklahoma
Robert Podgorney, Idaho National Laboratory
Mitch Plummer, Idaho National Laboratory
Travis McLing, Idaho National Laboratory
Richard Smith, Smith Geologic and Photographic Services, LLC
Lee Liberty, Boise State University
Ahmad Ghassemi, University of Oklahoma
Suzette Payne, Idaho National Laboratory
John Wellhan, Idaho State University

April 2016

Snake River Geothermal Consortium
Hosted by Idaho National Laboratory
Idaho Falls, Idaho

www.snakerivergeothermal.org

Prepared for the
U.S. Department of Energy
Office of Energy Efficiency and Renewable Energy
Under DOE Idaho Operations Office
Contract DE-AC07-05ID14517

EXECUTIVE SUMMARY

This document provides a geologic model of the proposed site for the Frontier Observatory for Research in Geothermal Energy (FORGE) on the northern margin of the Eastern Snake River Plain (ESRP). FORGE marks the U.S. Department of Energy's (DOE's) largest effort to advance the deployment of enhanced geothermal systems (EGS). EGS has the potential to tap into the earth's heat through engineered geothermal reservoirs, transforming the energy future for the United States and the world. The FORGE initiative aims to develop methodologies and technologies that will bring this resource into the nation's energy portfolio. This project is being conducted by the Snake River Geothermal Consortium at the 110-km^2 (42.6-mi^2) Geothermal Resource Research Area (GRRA) on the Idaho National Laboratory (INL) Site.

The goals of our conceptual modeling effort and this report are to (1) develop a set of conceptual model scenarios of the subsurface beneath the GRRA that honor the existing data, (2) demonstrate that the subsurface beneath the GRRA meet the criteria for FORGE, (3) develop a preliminary geomechanical model to assist in well and reservoir development planning, (4) develop a characterization plan to reduce uncertainty in the geologic model and reduce the risks for establishing FORGE, and (5) argue that our proposed site is representative of the EGS potential throughout the ESRP, demonstrating that lessons learned at FORGE may be applicable to a much larger EGS resource.

The INL Site, one of DOE's largest laboratories (2,300 km^2 [890 mi^2]), is located within the track of the Yellowstone Hotspot. Over the past 17 Ma, as the North American plate has moved southwest over the stationary hotspot, mantle-derived magmas were injected into the upper crust, melting the silicic upper crust and producing numerous rhyolitic eruptions that formed calderas similar to those observed in and around Yellowstone National Park. Today, these calderas in the ESRP and the associated rhyolitic deposits are buried under 1 to 2 km (0.6 to 1.5 mi) of interbedded basalt flows and sediments. Deep boreholes throughout the ESRP document the widespread occurrence of low-permeability hydrothermally altered rhyolites and high heat flows (>110 mW/m^2) beneath the basalt layer. These potential EGS reservoir rocks are encountered in every deep well that penetrates through the overlying basalts and sediments on the ESRP.

Selection criteria for the FORGE site are a permeability of less than 10^{-16} m^2 (100 μD) and a temperature between 175 and 225°C (347 and 437°F) at a depth between 1.5 and 4 km (4,900 and 13,100 ft). Our target reservoir rocks for EGS at the GRRA include intra- or extra-caldera rhyolite flows or extra-caldera ignimbrite deposits. Permeability measurements have been completed on samples from representative lithologies in deep boreholes near the GRRA. Intra-caldera facies sampled from depths of 1.485 and 3.15 km (4,872 and 10,335 ft) depth have permeabilities of 7×10^{-20} to 1.8×10^{-17} m^2 (0.068 to 18.2 μD), and an extra-caldera sample from 1.34 km (4,396 ft) depth has a permeability of 2×10^{-18} m^2 (2 μD). Conductive temperature gradients measured in deep boreholes nearest the GRRA range between 44.4 and 76.6°C/km (2.4 and 4.2°F/100 ft) and predict that the 175°C (347°F) isotherm will be encountered between 2.4 and 3.8 km (7,874 and 12,460 ft) depth. Based on all available data and under every potential conceptual scenario, our site meets the temperature, depth, and permeability criteria defined by DOE.

We present models of the subsurface that synthesize existing geologic, deep-borehole, and geophysical data. The GRRA sits on the northern margin of the ESRP. As a risk mitigation measure, we developed two geologic structural models that differ in how the geometry of the subsurface is interpreted. One end-member structural model is based on published estimates of caldera boundaries and eruptive volumes. It depicts a system of four nested calderas butted up against the mountains to the north of the GRRA, with rhyolites persisting to a depth of 6.25 km (20,500 ft). The other end-member structural model is based on the attitude of Mesozoic fold hinges north of the GRRA, which record subsidence of the ESRP due to the emplacement of a dense, ~10-km (32,808-ft)-thick, mid-crustal sill. This structural model depicts a uniformly dipping flexural surface defining the lower boundary of the ESRP rhyolites

and shows extra-caldera rhyolite units thickening to the south. Overlaying the thermal gradients discussed above with the structural scenarios, in all geologic and thermal scenarios, we find an acceptable reservoir volume for FORGE at our site.

We developed a preliminary one-dimensional geomechanical model to assess suitability of the site for fracture stimulation by fluid injection and present a workflow for extending this model into three dimensions. The preliminary model is based on rock strength measurements and well logs from a deep borehole known as INEL-1 located ~2.1 km (1.3 mi) east of the GRRA. These data indicate that the relative stress magnitudes are $S_v \geq S_{Hmax} > S_{Hmin}$ consistent with a transition between a strike-slip and normal faulting regime. Fracture analysis of ca. 1990 borehole televiewer data indicate that there are multiple fracture populations that can provide a base reservoir volume for stimulation.

Finally, we present our characterization plans for Phase 2 of FORGE. These plans are broken into three subphases. Phase 2A is a 4-month period of permitting, planning, and design. Phase 2B is a 12-month period, during which we will characterize our site using a variety of geophysical methods, drill one corehole, and reexamine an existing deep borehole near our proposed FORGE site; the data collected in Phase 2B will be used to refine our conceptual and geomechanical models. Phase 2C is a 9-month period of extensive characterization and testing, during which we will drill a 3- to 4-km (9,842- to 13,123-ft)-deep characterization hole (the "pilot well") and a shallow 250-m (820-ft) groundwater-supply well.

Based on the available data, we conclude that the GRRA meets the DOE requirements for a FORGE site. We find evidence for a low-permeability rhyolite reservoir with temperatures greater than 175°C (347°F) within the target depth range of 1.5 to 4 km (4,921 to 13,123 ft). The available data indicate a well-developed fracture network, providing a base volume for stimulation, and our preliminary geomechanical model indicates favorable conditions for fracture stimulation. Our site has additional favorable characteristics, including an abundance of onsite water from the ESRP aquifer and easy access in all seasons due to its proximity to U.S. Highway 20.

CONTENTS

FIGURES

TABLES

ACRONYMS

1D	one-dimensional
3D	three-dimensional
DFN	discrete fracture network
DITF	drilling-induced thermal fracture
DOE	U.S. Department of Energy
DSWI	deep shear wave imaging
EGS	enhanced geothermal systems
ESRP	Eastern Snake River Plain
FORGE	Frontier Observatory for Research in Geothermal Energy
GRRA	Geothermal Resource Research Area
INL	Idaho National Laboratory
ka	thousand years
LIDAR	light detection and ranging
LWD	logging while drilling
Ma	million years
M_s	surface wave magnitude
MT	magnetotelluric
R&D	research and development
SRGC	Snake River Geothermal Consortium
SRP	Snake River Plain
UCS	unconfined compressional strength
USGS	United States Geological Survey

Geologic Conceptual Model

1. INTRODUCTION

This document presents the geologic model of the proposed site for the Frontier Observatory for Research in Geothermal Energy (FORGE) on the Eastern Snake River Plain (ESRP). FORGE marks the U.S. Department of Energy's (DOE's) largest effort to advance the deployment of enhanced geothermal systems (EGS). EGS has the potential to tap into a conservatively estimated 100 GW of baseload power-generating capacity by harnessing the earth's heat through engineered geothermal reservoirs. The FORGE initiative aims to develop methodologies and technologies that will bring this resource into the nation's energy portfolio (Metcalfe, 2015). This project is being conducted by the Snake River Geothermal Consortium (SRGC) at the 110-km^2 (42.6-mi^2) Geothermal Resource Research Area (GRRA) on the Idaho National Laboratory (INL) Site. See Figure 1.

INL, which was originally named the National Reactor Testing Station, was established in 1949 as a site of federal energy research and development (R&D). The safety requirements of nuclear facilities at INL have supported decades of natural-hazard analyses and geotechnical investigations, yielding a body of work that we cite extensively throughout this document. Key publications and documents directly related to our FORGE geologic conceptual model are attached as appendixes. These include papers on the regional geologic setting (McCurry et al., 2016, Appendix A), rock physics modeling (Grana, et al., 2016, Appendix B), the geochemistry of the ESRP aquifer (McLing et al., 2016, Appendix C; Welhan, 2016, Appendix D; and Dobson et al., 2015, Appendix E); and the geomechanical characterization of rock core and borehole (Bakshi, et al., 2016, Appendix F; also see Appendix G).

The development of geothermal energy on the ESRP, where the INL Site is located, is intimately tied to an understanding of its magmatic and tectonic history. Our conceptual model places strong emphasis on rhyolitic volcanic processes of the ESRP, because these rocks and their deep crustal roots have the necessary heat for a state-of-the-art EGS.

We begin with a regional geologic overview, describing the origin of this extensive igneous province. Rhyolite calderas and their eruptive products are emphasized, because these are the products of early volcanism and comprise the target rocks for our EGS. We have weighed the available geotechnical evidence to select a promising site for EGS R&D, and we focus on this site in our conceptual model, describing the lithology and physical properties of subsurface volcanic materials and the thermal regime at depth. We develop a geomechanical model to show that the subsurface temperatures, rock properties, and state of stress are ideal for an EGS reservoir, and we point out other favorable characteristics (Table 1), such as the availability of abundant fresh water and the presence of multiple fracture sets at depth. Finally, we identify geologic risks to the successful completion of a FORGE facility on the INL Site.

It is important to note that the anticipated long-term outcome of this project is not a single geothermal R&D facility; this is a gateway demonstration of EGS principles that can be applied across a wide region—e.g., the entire ESRP—having subsurface stratigraphy, reservoir rocks, and geophysical properties similar to those in the INL area. Given the heat flow of this large igneous province and the potential for replication of the FORGE results, our project could pave the way for energy abundance in the northern Rockies, along the Wasatch Front, and into the Pacific Northwest for a century or more, accelerating an energy transition nation- and world-wide. We seek to build on the legacy of other federal energy projects such as the Bonneville Power Administration, which supplied hydropower that helped win a world war and continues to support the industrial base of several states. However, we will do so with minimal environmental consequences.

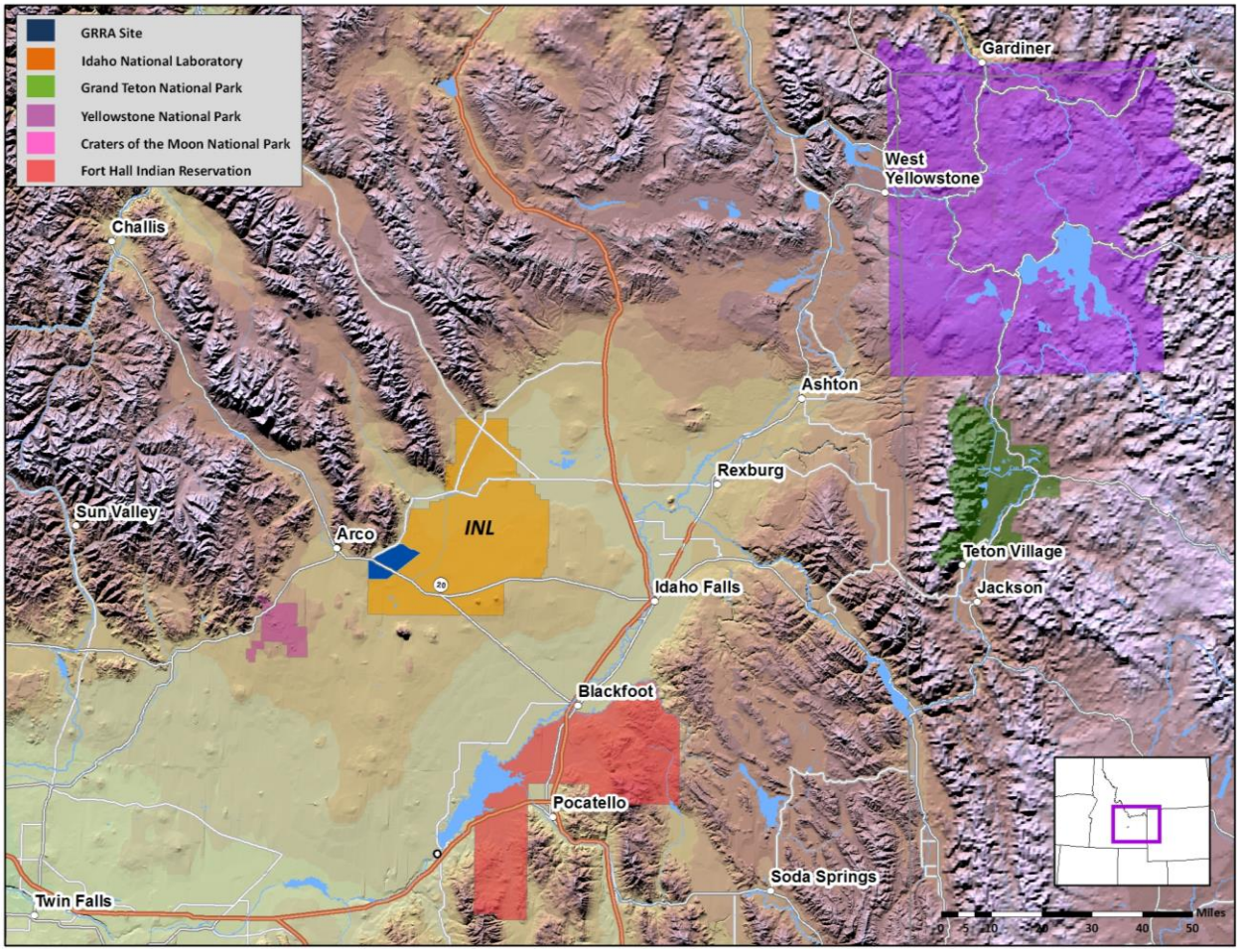

Figure 1. Map of INL, the GRRA, and the surrounding area.

Table 1. Summary of favorable characteristics for the proposed EGS reservoir at INL.

Temperature at Depth	In Situ Stress	EGS Reservoir Properties	Drilling Conditions	Infrastructure	Site Preparation and Access	Water
175°C between 2.4- and 3.8-km (1.5- and 2.4-mi) depth	At 3,500 m (11,500 ft) S_v=82 MPa S_{Hmax}=89±11 MPa S_{Hmin}=58±2 MPa	Reservoir permeability 6.7×10^{-20} to 1.79×10^{-17} m^2 (0.068 to 18.2 µD); readily fractured at reasonable fluid pressure	INL/U.S. Geologic Survey drilled hundreds of water wells in basalt/ sediment (difficult); underlying rhyolites easily drilled, with stable boreholes	FORGE site is near a paved highway and a power line; INL emergency responders within 11 km (7 mi)	Flat, level, stable terrain; easily excavated rock and soil	Abundant fresh water with low total dissolved solids for reservoir stimulation and FORGE operations

2. GEOLOGIC SETTING

High heat flow in the western United States (Figure 2) is broadly associated with crustal extension, lithospheric thinning, Basin and Range Province magmatism, and the presence of the Yellowstone Hotspot. The highest heat flow of North America is measured in the Pacific Northwest, within the Yellowstone–Snake River Plain (SRP) volcanic province of northwestern Wyoming, southwestern Montana, southern Idaho, and central Oregon. The Yellowstone Hotspot is the source of this immense trail of volcanism that began about 17 Ma with flood-basalt eruptions of the Columbia Plateau in Oregon and eastern Washington and with synchronous caldera-related silicic volcanism near the Oregon-Idaho border.

Volcanism progressed northeastward at a rate of about 2.4 cm (0.94 in.) per year, a pattern attributed to the southwestward motion of the North American plate over a fixed mantle plume. The ESRP and Yellowstone caldera system compose the younger part of this large igneous province, which during the past 17 Ma has produced enough magma to fill the Great Lakes, mostly as rhyolite lava flows and ash-flow tuffs. The ESRP encompasses 26,000 km^2 (10,000 mi^2) of volcanic terrain and is a region of voluminous rhyolitic volcanism that occurred between about 10 and 4.5 Ma (Figure 3). The early rhyolite deposits and associated calderas are now largely buried beneath younger basalt lava flows and sediment, but their presence is inferred from surface geology around the margins of the ESRP, the presence of rhyolite in deep boreholes, and geophysical observations. The prodigious volcanic output is dwarfed by the inferred volume of intrusive igneous rocks that must be present at upper- and mid-crustal depths beneath the ESRP. The presence of a large mid-crustal "sill" of dense intrusive rock is required in order to explain the results of regional seismic and gravity surveys, as well as the pronounced subsidence of the ESRP.

The large-scale, lithospheric structure of the ESRP is known from seismic, gravity, and magnetotelluric (MT) studies. The seismically imaged plume-like body beneath Yellowstone is evidence of a deeply rooted thermal anomaly in the mantle (Schmandt et al., 2012) (Figure 4). More important for EGS in the ESRP is the legacy of that anomaly, which is evident from both seismic and MT studies and extends more than 300 km (186 mi) southwest of Yellowstone (Schmandt et al., 2012; Kelbert et al., 2012) (Figure 4). Reduced seismic velocities and high conductivities indicate elevated temperatures and partial melt beneath the Moho along the entire length of the ESRP (Kelbert et al., 2012). At mid-crustal levels, a ~10-km (~20,300 ft)-thick, high-density, high-seismic-velocity body spans the length of the ESRP (Wagner et al., 2012) and extends up to 40 km (25 mi) south of the plain (DeNosaquo et al., 2009). The mid-crustal sill is thought to be formed by intrusion of mantle-derived melts, which rose to a depth of neutral buoyancy and either melted the upper crust or underwent fractionation to produce the extensive rhyolitic volcanism that characterizes the plain (Figure 5). Crustal subsidence resulting from the emplacement of the high-density, mid-crustal sill is estimated to be between 4.5 and 8.5 km (14,700 and 28,000 ft) (McQuarrie and Rodgers, 1998).

Volcanic rocks of the ESRP have a distinctly bimodal (basalt-rhyolite) distribution (Leeman et al., 2009). It is estimated that more than 140 caldera-forming silicic eruptions have occurred within the ESRP over the past 10 Ma (Perkins and Nash, 2002). Volume estimates for individual eruptions range from tens to thousands of cubic kilometers (Branney et al., 2008) and indicate that calderas similar to, or greater in size than, the currently active Yellowstone caldera system are distributed throughout the ESRP. Although structures and volcanic rocks from these events are largely buried underneath up to 2 km (1.2 mi) of tholeiitic basalts and interbedded sediments, remnants are preserved in ignimbrite flows in the Basin and Range Province to the north and south of the plain. Space-time patterns of both rhyolitic and basaltic volcanism indicate that rhyolitic eruptions were primarily focused in distinct volcanic fields centered over the position of the hotspot, while subsequent basaltic activity was more diffuse in both space and time. For example, basaltic volcanism as recent as 2 ka has occurred at Craters of the Moon National Monument (Kuntz et al., 1986), which is ~200 km (~124 mi) southwest of the current hotspot position

beneath Yellowstone and ~35 km (~22 mi) west of the GRRA. Such recent volcanism reflects long-term, persistently high temperatures at depth and is supported by elevated $^{3}He/^{4}He$ isotopic ratios, indicating that mantle-derived He is being introduced to the upper crust and hydrosphere of the ESRP (Dobson, et al., 2015).

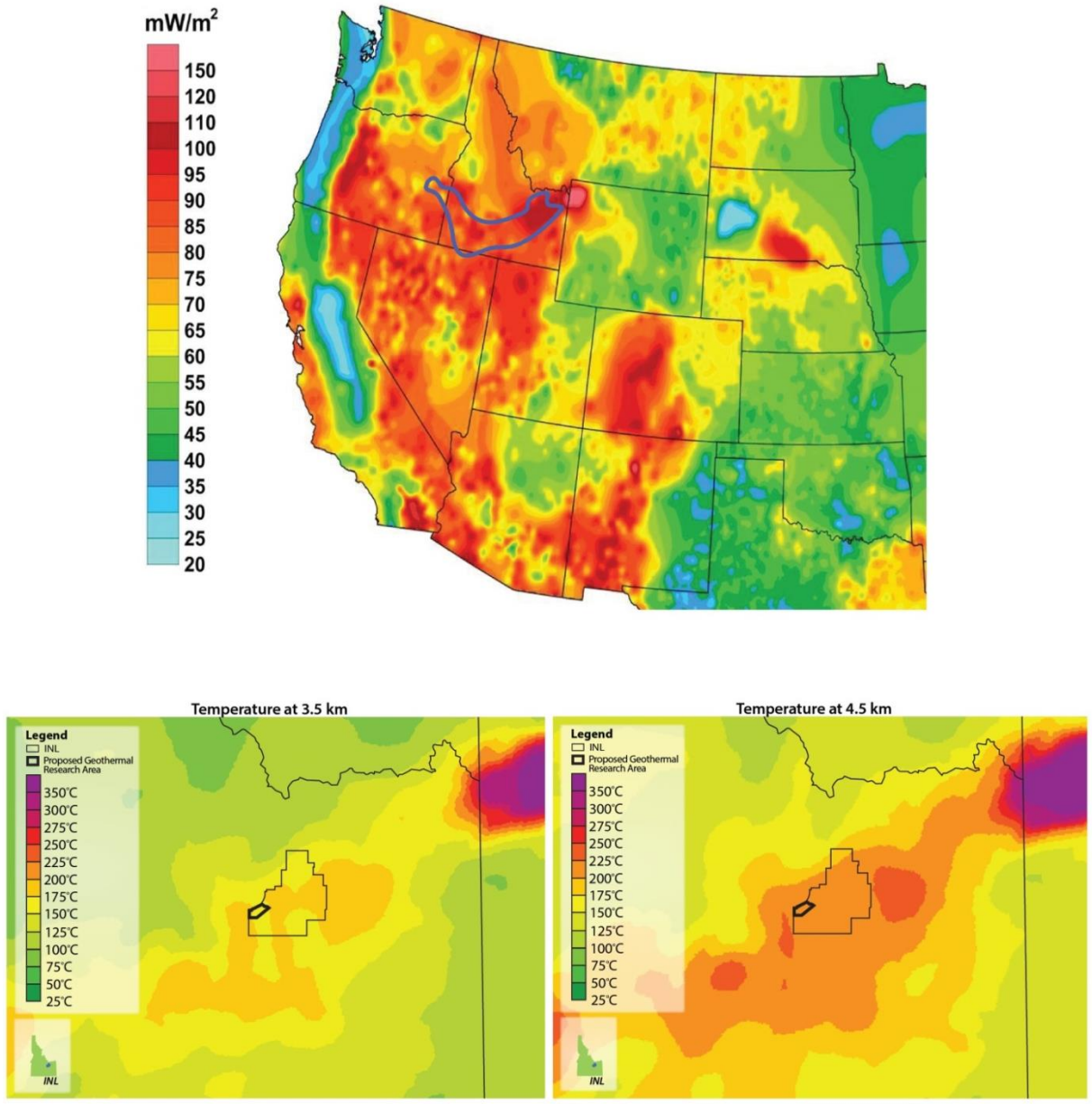

Figure 2. Heat flow maps of the western United States from Blackwell et al. (2011). Heat flow of the ESRP in southeastern Idaho exceeds 100 mW/m^{-2} over a region of about 26,000 km^2 (10,000 mi^2). Lower panels show predicted temperatures at 3.5- and 4.5-km (11,500- and 14,800-ft) depths for the region. The outlined area in the center of the lower panels shows the location of the INL Site; the bold outline shows the location of the GRRA.

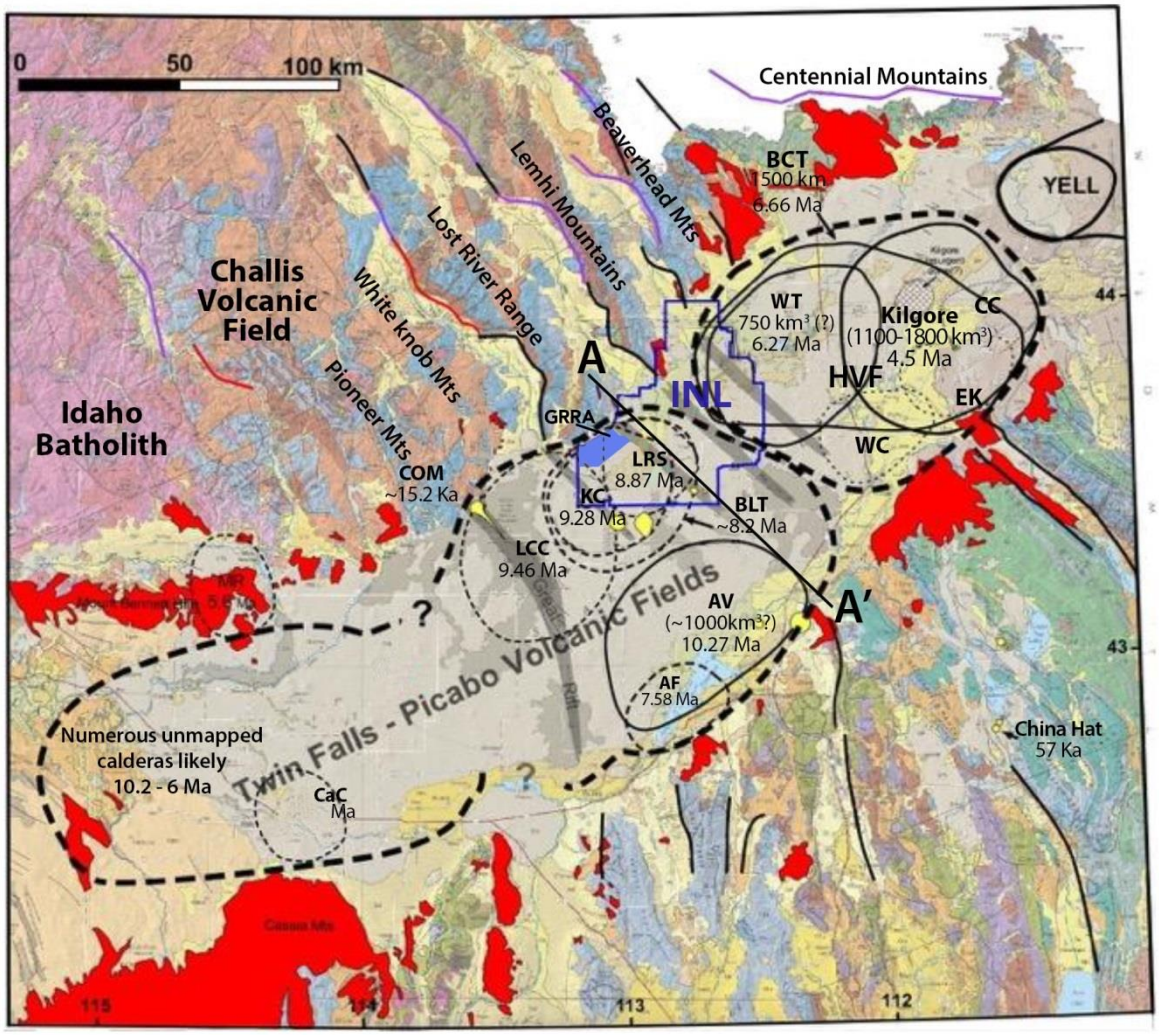

Figure 3. Geologic map of the ESRP and its surroundings. ESRP caldera related ignimbrite deposits are shown in red. Inferred calderas of the Twin Falls, Picabo, Heise, and Yellowstone volcanic fields are indicated. For a more detailed explanation see Appendix A.

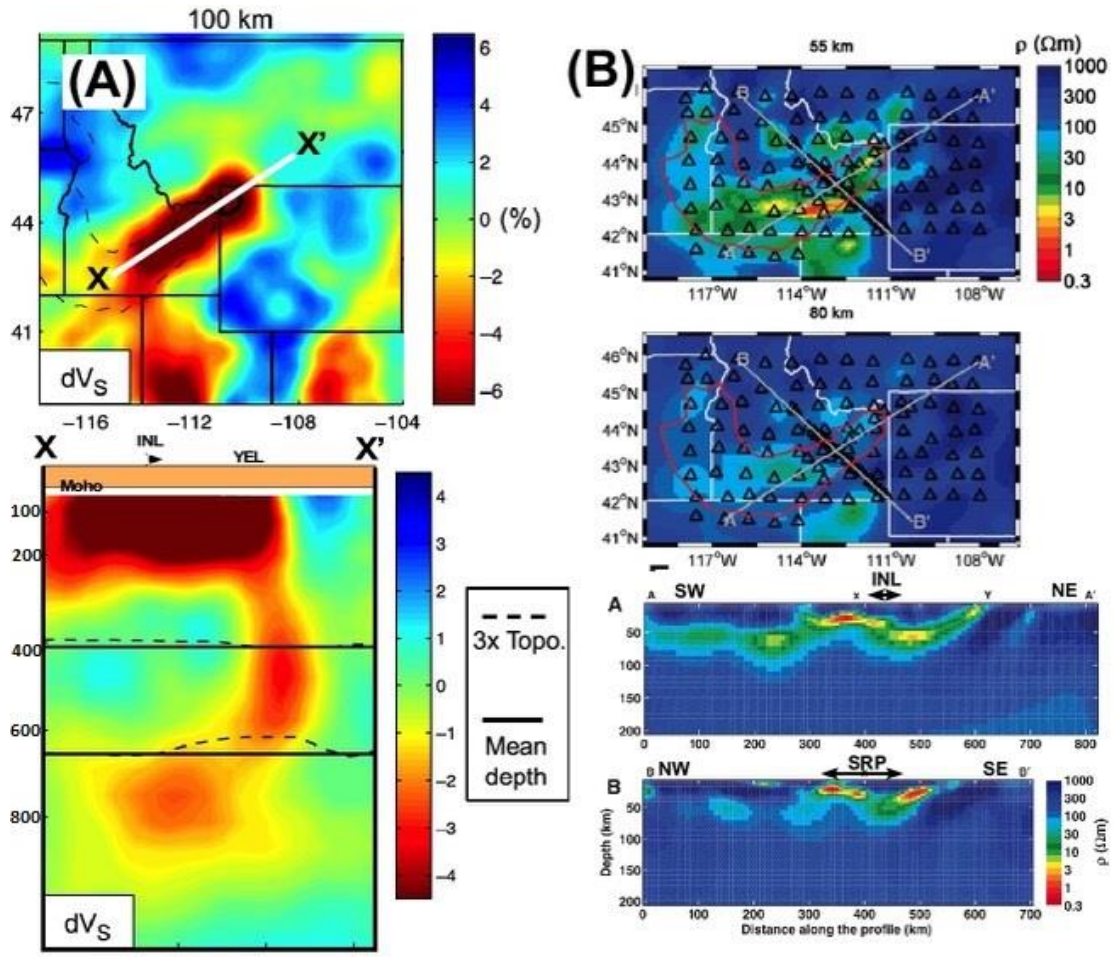

Figure 4. (A) Shear wave velocity structure beneath the ESRP (Schmandt et al., 2012) showing reduced mantle velocities beneath the entire ESRP and indicating elevated temperatures and a plume-like body beneath Yellowstone; depth scale is in kilometers. (B) Regional resistivity structure from inversion of MT data (from Kelbert et al., 2012) showing a conductive body at Moho depths beneath the ESRP.

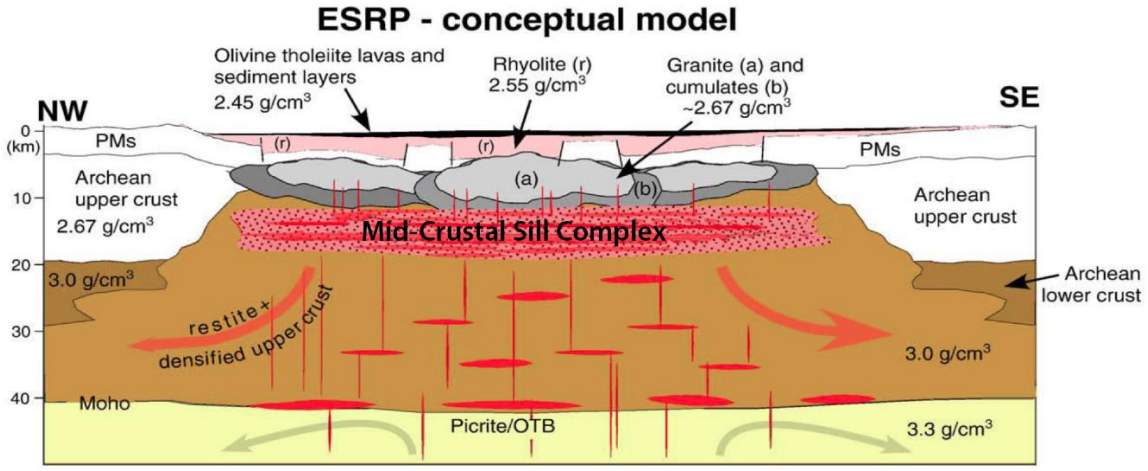

Figure 5. A cross section of the crust and upper mantle (modified from McCurry and Welhan, 2012; Peng and Humphreys, 1998) along A-A' (Figure 2).

Up to 2 km (1.2 mi) of mantle-derived, tholeiitic basalts interbedded with sediments have accumulated over the past ~6 Ma (Shervais et al., 2013; Potter, 2014) and overlie the ESRP rhyolites. While these units shield the underlying rhyolites and associated calderas from view, they also host the prolific ESRP aquifer. The ESRP aquifer is composed of two systems (McLing et al., 2016). The shallow system is fed by snowmelt from the surrounding mountains and is characterized by high flow rates (~1.52 to 10.51 m [5 to 34.5 ft] per day) and relatively cold water (9 to 15°C [48 to 59°F]). The deeper system is characterized by slow-moving (0.6 to 9.1 cm [0.24 to 3.6 in.] per day) and warm (>30°C [86°F]) water (Mann, 1986). The shallow system will provide large volumes of fresh water for EGS development.

The ESRP is bound to the north and south by Basin and Range extensional provinces. As indicated by the 1983 Borah Peak earthquake ~89 to 110 km (~55 to 68 mi) north of the GRRA, extensional faulting in the Basin and Range Province continues to the present. Although the region around the ESRP is seismically active, no earthquakes larger than M_s 3 have been detected in the period since 1961 beneath the plain. However, a number of linear volcanic rift zones oriented north-northwest suggest that the plain is extending in the same direction as the surrounding province. A number of explanations have been put forth regarding the lack of seismic activity beneath the plain. These include ductile deformation beneath the plain, a consequence of elevated subsurface temperatures (e.g., Furlong, 1979), a dike intrusion mechanism of extension on the plain (Parsons et al., 1998), and anomalously high strength of mafic intrusive rocks beneath the plain resulting in conditions that resist tensile failure (Anders et al., 1989).

2.1 Calderas in the Eastern Snake River Plain

Caldera-related silicic volcanism is a defining characteristic of the Yellowstone–SRP igneous province during the past 17 Ma. The Yellowstone output of the past 2 Ma is conservatively estimated as 6,000 km^3 (1,449 mi^3) (Christiansen, 2001). Assuming the volume of rhyolitic magma erupted from the ESRP during the past 10 Ma is equal to that of Yellowstone (also conservative), and adding 10,000 km^3 (2,399 mi^3) of rhyolite erupted between 10 and 13 Ma from the central SRP (Leeman et al., 2008), gives a total volume of rhyolite erupted from the Yellowstone–SRP volcanic system during the past 13 Ma of about 22,000 km^3 (5,300 mi^3). This output would fill all of the Great Lakes. The rhyolite was erupted mostly as ash-flow tuffs and rhyolite lava flows, and the largest eruptions—mainly ash-flow tuffs—are among the largest known from the geologic record. Individual eruptive volumes of several rhyolite ash flows from Yellowstone, the ESRP, and central SRP are estimated to exceed 1,500 km^3 (360 mi^3), not including the associated voluminous and widely dispersed ash-fall deposits that blanketed the surrounding region during the past 13 Ma (Perkins and Nash, 2002). The petrologic and isotopic features of Yellowstone–SRP rhyolite indicate melting of crustal rocks at about the 15-km (9-mi) depth, magma storage at the 5- to 10-km (3- to 6-mi) depth, interaction with upper-crustal meteoric fluids, and large-volume plinian eruptions. The magma origin, storage, volume, and dispersal all suggest eruption from calderas that have been mapped in southern Idaho as Miocene surface features (where not covered), in the older part of the Yellowstone–SRP in eastern Oregon and southwest Idaho, and on the Quaternary Yellowstone Plateau volcanic field. The latter region includes several large nested calderas formed in the past 2 Ma, the site of contemporary seismicity and vigorous hydrothermal activity in Yellowstone National Park (Christiansen, 2001; Smith et al., 2009). On the ESRP, rhyolite calderas of similar origin and size are inferred to have formed about 10 to 4.5 Ma but are covered by younger basalts and sediment. The presence of calderas at depth is confidently inferred from the characteristics of voluminous caldera-related rhyolite lava flows and ash-flow tuffs exposed around the margins of the ESRP (Morgan and McIntosh, 2005; Pierce and Morgan, 1992, 2009; Anders et al., 2014). Based on the scaling relationships observed worldwide for caldera areas versus erupted volume (deSilva and Gregg, 2014), the largest ESRP ash-flow tuffs were likely erupted from calderas about 50 km (31 mi) in diameter (Figure 3).

A variety of caldera geometries and subsidence styles are known from continental settings (Lipman, 1997); typical caldera features are shown in Figure 6. Buried calderas beneath the ESRP are likely to exhibit these features and rock types, as shown by mapped volcanic deposits around the margins of the ESRP (outflow ignimbrite sheets and lava flows) and by the thick rhyolite lava flows and welded ash flows intersected in several deep boreholes of the INL area (Figures 7 through 9). Several deep boreholes bottom in rhyolite after penetrating silicic lava flows, ash-flow tuffs, airfall tuffs, and minor volcaniclastic sediment (Anders et al., 2014; Doherty et al., 1979). The region's deepest borehole—INEL-1, which is 3.15 km (10,365 ft) total depth—is interpreted to have bottomed in subcaldera intrusive rhyodacite after penetrating 2.1 km (6,890 ft) of rhyolite caldera fill (Doherty et al., 1979). Within the GRRA, Borehole USGS 142 bottomed in rhyolite after penetrating 150 m (492 ft) of rhyolite, interpreted as a single ash-flow tuff that either filled its source caldera or erupted from another caldera nearby (McCurry et al., 2016; Appendix A).

Unlike areas with exposed caldera structures and associated mappable volcanic deposits, the locations, sizes, and shapes of ESRP buried calderas are not precisely known. However, their presence is demonstrated by the evidence cited above, with one or more rhyolite calderas thought to underlie the GRRA based on borehole lithologies, the characteristics of associated eruptive products in outcrops along the northwestern margin of the ESRP, and seismic-refraction data suggesting the northwest margin of the ESRP is an abrupt structural boundary (Pankratz and Ackermann, 1982; Sparlin et al., 1982). This boundary can be interpreted as having been formed partly by caldera subsidence (Figure 9).

Large calderas are commonly filled with low-density volcanic rocks, and these calderas commonly produce large, circular anomalies in both gravity and magnetic fields. Interpretations of gravity and magnetic data from the ESRP are confounded by dominant remanent magnetization of the overlying basalt lava flows and feeder dikes, which have both normal and reversed polarity, and by the apparent lack of density contrast between caldera fill and surrounding rocks, which may also be of volcanic origin. An early gravity and magnetic investigation of the ESRP (Mabey, 1978) discovered that ESRP gravity anomalies did not have the same character as anomalies in the adjacent Basin and Range. Large gravity highs and lows within the ESRP are approximately twice as broad as those of the surrounding Basin and Range, reflecting the volcanic versus nonvolcanic origins of the adjacent regions and their contrasting tectonic evolution, making identification of specific, rhyolite volcanic features difficult using gravity and magnetic signatures alone.

During Phase 1, our team examined the possibility of imaging caldera boundaries using the existing gravity and MT data sets. A regional gravity data set is available from the Pan American Center for Environmental Earth and Environmental Studies, and magnetotelluric data are available from Earth-Scope. Sparse data coverage near the GRRA in both data sets and non-uniqueness associated with gravity hampered these efforts. After reinverting a regional MT data set from the Earth-Scope array with a refined mesh near the GRRA, we found that the data were not able to resolve features in the shallow crust with lateral dimensions relevant to FORGE.

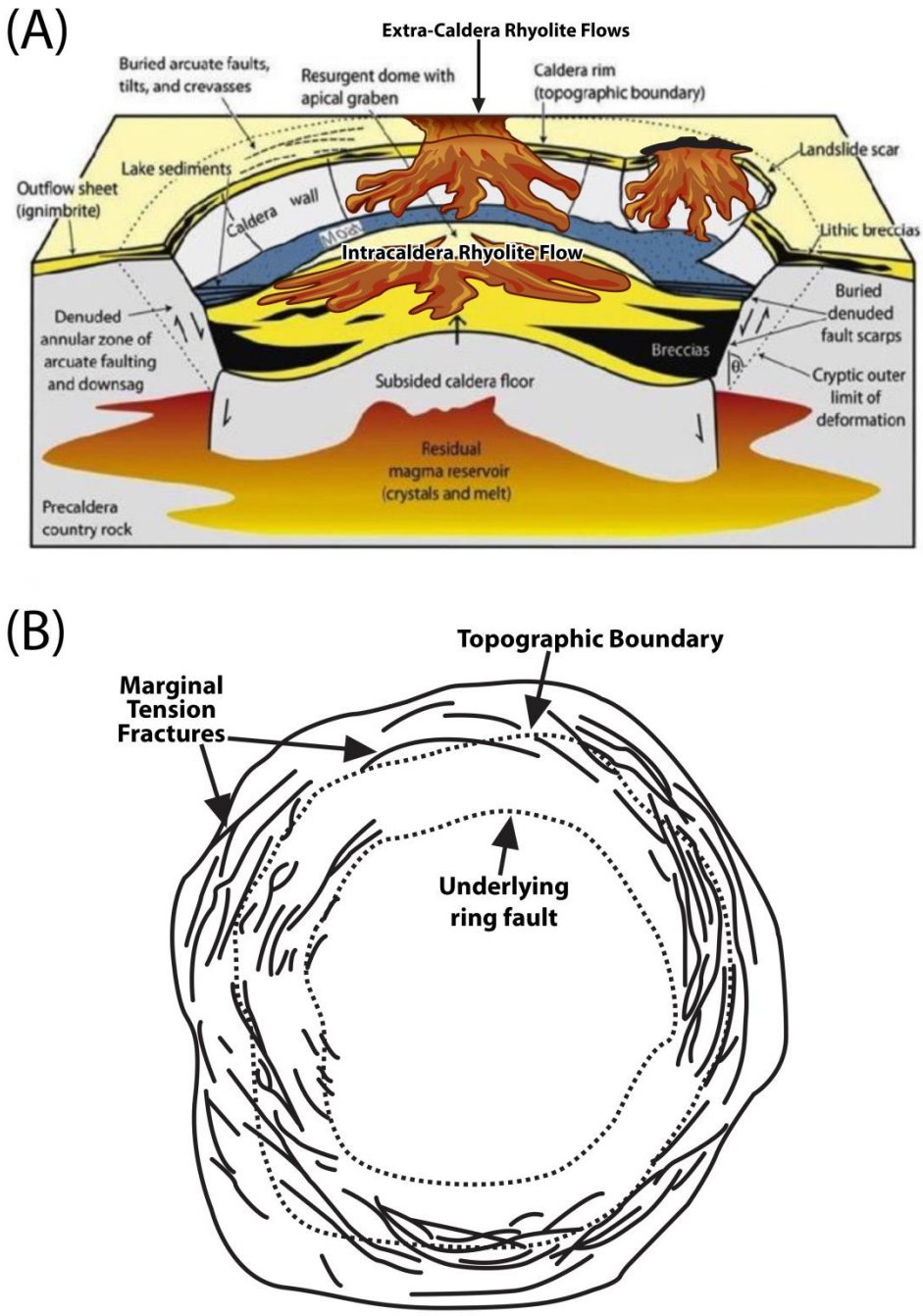

Figure 6. **(**A**)** Summary figure illustrating major features of a resurgent caldera (after Branney and Acocella, 2015). (B**)** Detailed features of caldera border zones (after Cole, 2005).

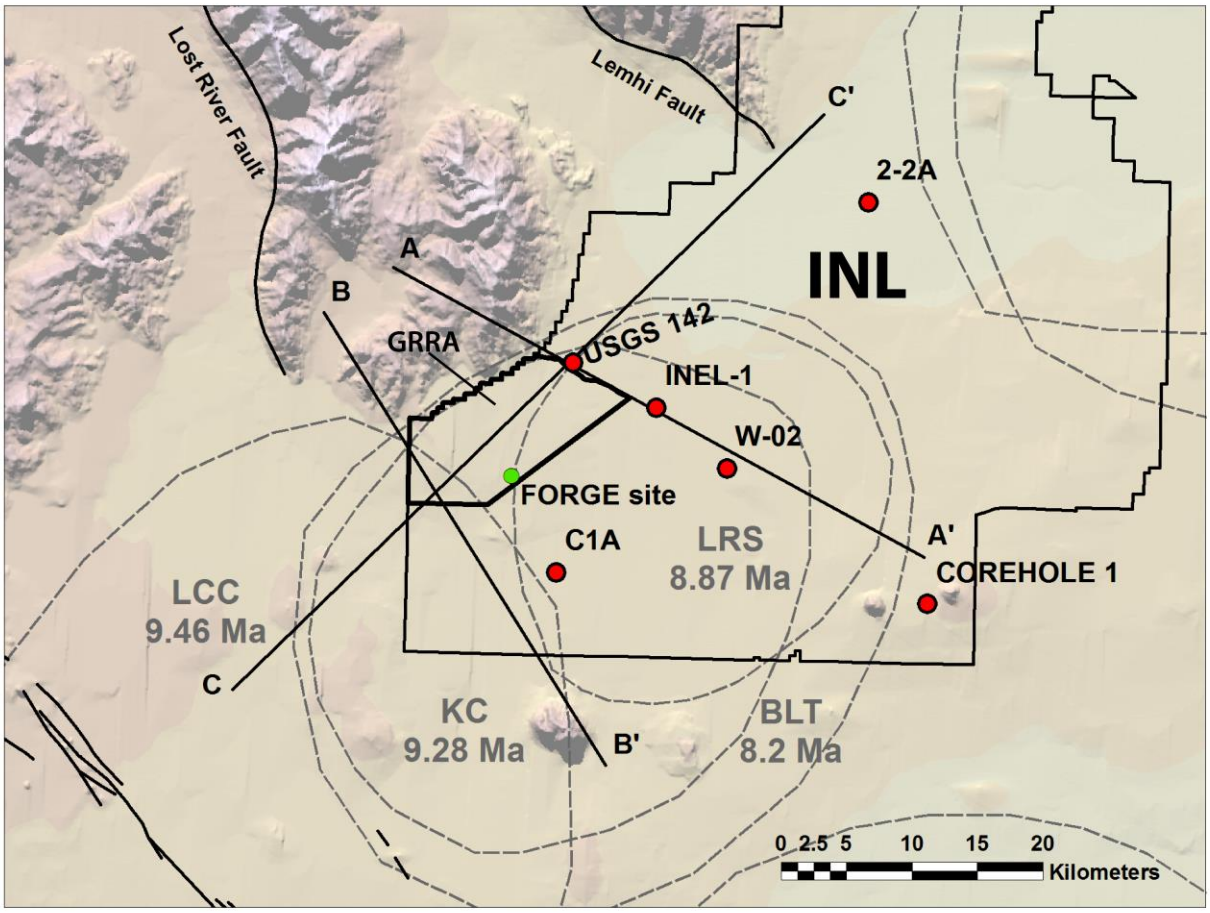

Figure 7. Regional map showing the INL, GRRA, caldera boundaries, and deep boreholes. Inferred caldera boundaries are shown as dashed lines (LCC – Little Choke Cherry; KC – Kyle Canyon; LRS – Little Lost River; BLT – Big Lost Trough). Locations of the LCC, KC, and LRS caldera boundaries are from Anders et al. (2014), and the BLT boundary is from McCurry et al. (2016; Appendix A). Locations of cross-sections A-A', B-B', and C-C' (Figure 9) and the proposed FORGE site are also indicated.

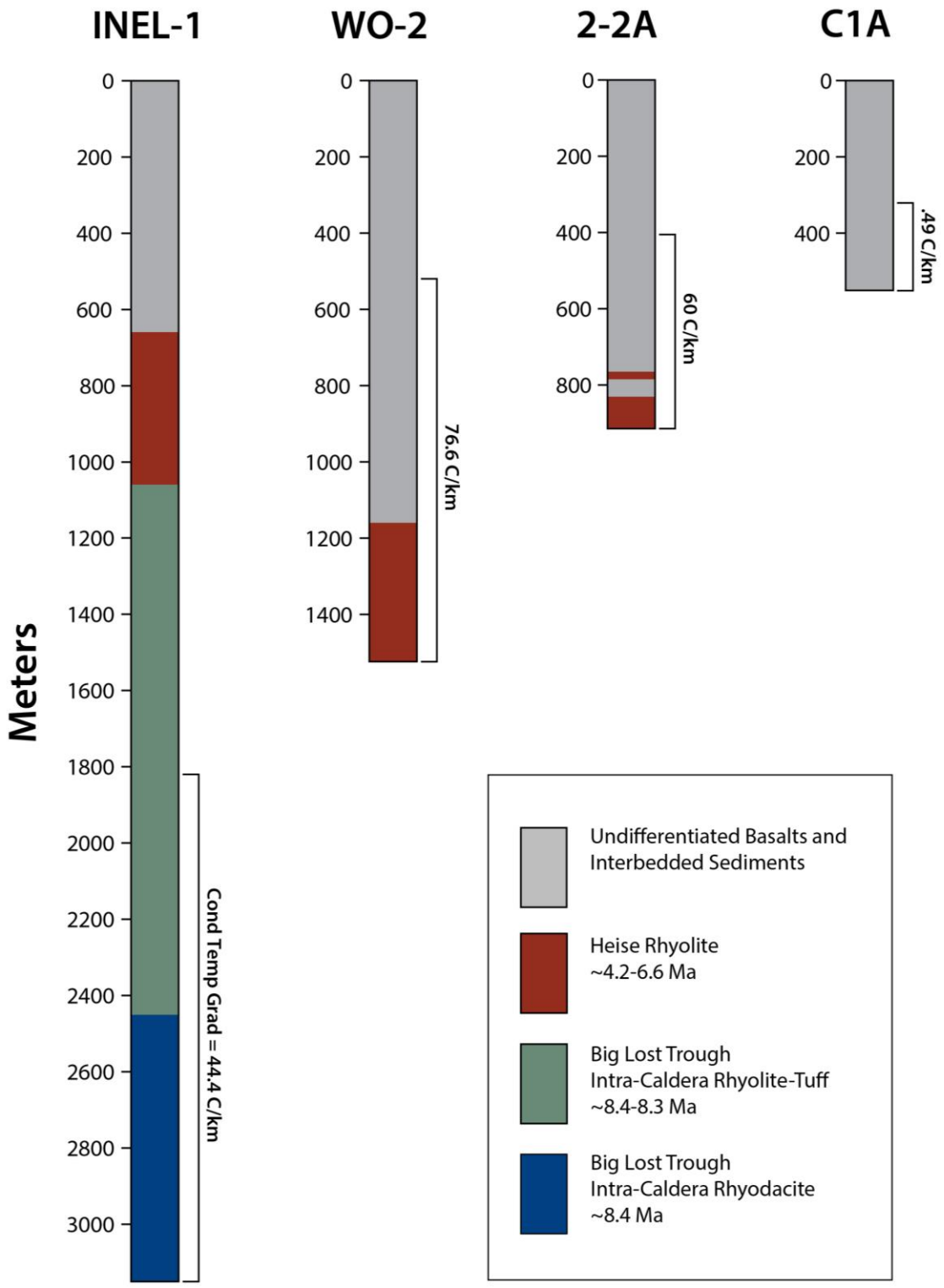

Figure 8. Summary lithologic logs for deep Boreholes INEL-1, WO-2, 2-2A, and C1A. Well locations are shown in Figure 6.

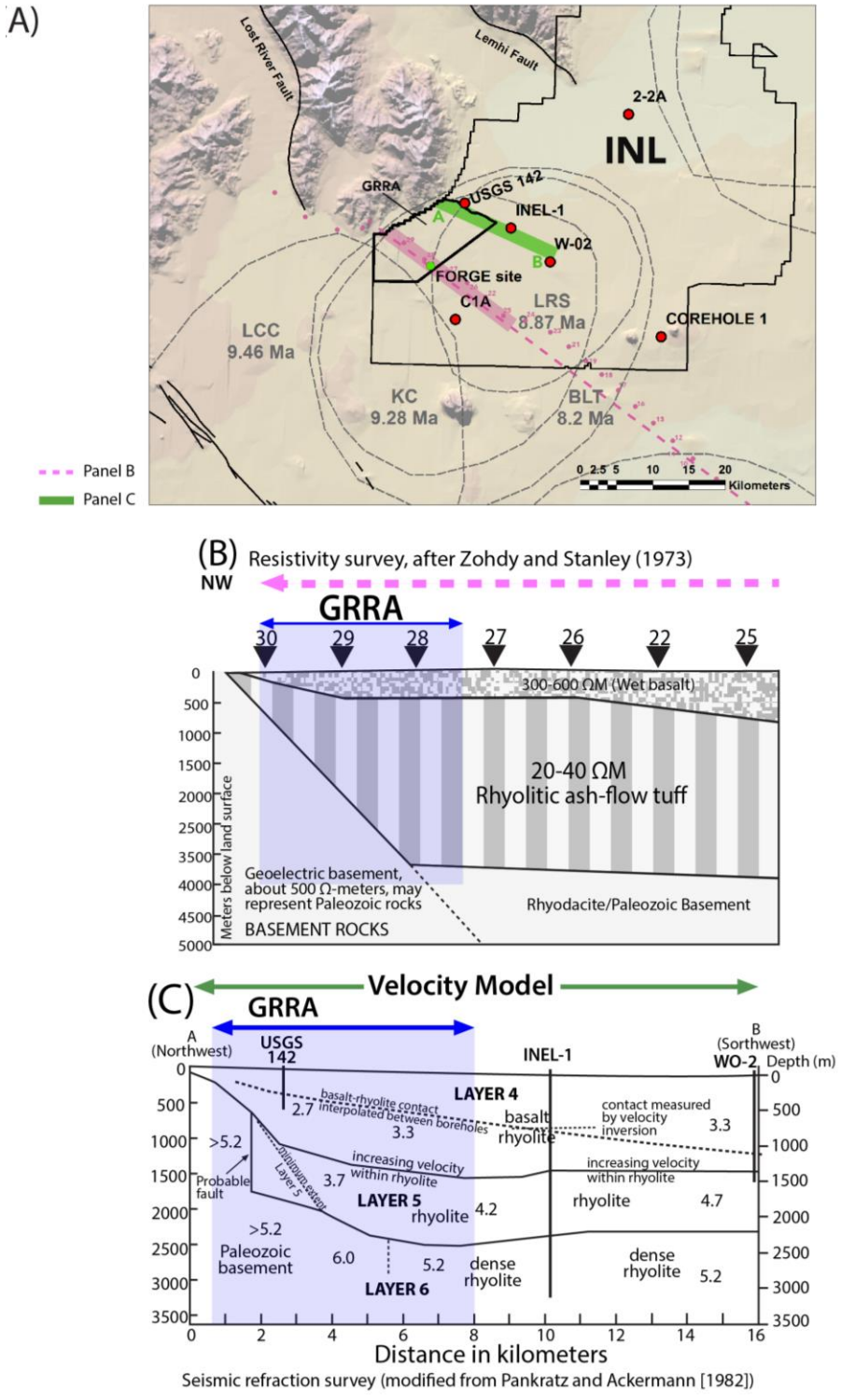

Figure 9. **(**A**)** Geologic map of the GRRA and surroundings, emphasizing the locations of key geophysical surveys in the region. (B**)** Resistivity survey cross-section interpretation of Zohdy and Stanley (1973). (C**)** Seismic refraction survey cross-section interpretation of Pankratz and Ackermann (1982).

2.2 Geology of the Geothermal Resource Research Area

The GRRA is an approximately 110-km^2 (42.6-mi^2) area located on the northern margin of the ESRP within the 10.2–8 Ma Picabo volcanic field (Figures 3 and 7). The GRRA was established as part of INL's long-term land use and mission planning, which focused on a sitewide "energy park" vision, where various renewable and low-carbon energy generation processes can be studied and integrated for both research and commercial purposes. This INL planning processes coincided with the SRGC's screening-level analysis for EGS feasibility on the ESRP (Podgorney et al., 2016), and the results informed selection of the GRRA boundaries. Interestingly, completely independent of our analysis, the Snake River Plain Play Fairway analysis team (Shervais et al., 2016) also identified the GRRA region as a strong candidate for EGS development because of the region's high heat flow and low permeability characteristics, giving us confidence in our site selection.

The GRRA is bound to the northwest by the Arco Hills, which are composed of Mesozoic and Paleozoic sedimentary rocks that were extensively folded during late-Mesozoic to early-Tertiary compressional orogenesis and then underwent several periods of Tertiary to Quaternary extension. Northwest of the Arco Hills, the Lost River Range is bound to the west by the Lost River fault (Figure 7), a Basin and Range structure that produced the 1983 M_W 6.9 Borah Peak earthquake. The Lost River fault terminates in the ESRP about 10 km (6 mi) west of the GRRA, although the distance that the fault extends southward into the ESRP is uncertain.

A number of deep boreholes are in the vicinity of the GRRA (Table 2). The three deep boreholes with reliable data and nearest the location selected for FORGE are INEL-1, WO-2, and C1A (Figure 7).

Table 2. Summary of selected deep boreholes within or near the GRRA and SRGC FORGE site that either penetrate into rhyolite or have geothermal gradient information available.

Borehole Name	Distance from GRRA (distance from FORGE location)		Depth		Geothermal Gradient	
	km	mi	km	ft	°C/km	°F/100 ft
INEL-1	2.1 (12)	1.3 (7.5)	3.15	10,365	44.4	2.4
WO-2	9.1 (16.2)	5.7 (10)	1.52	4,986	76.6	4.2
C1A	7.2 (8)	4.5 (5)	0.55	1,805	49	2.6
2-2A	23.5 (34.4)	14.6 (21.3)	0.91	2,985	60	3.2
USGS 142	0 (9.8)	0 (6.1)	0.573	1,880	67.7[a]	3.7
Corehole 1	28.4 (33.1)	17.6 (20.6)	0.609	2000	41	2.3

a. Gradient measure in upper ~50 m (~160 ft) of conductive zone. Flow in borehole prevented reliable measurement in deeper sections.

Summaries of the salient aspects of borehole stratigraphy near the GRRA are illustrated in Figure 8. Rhyolites intersected in Boreholes WO-2 (Anders et al., 2014; McCurry and Rodgers, 2009) and 2-2A (Doherty, 1979) are dominated by two rhyolite lava flows and thin outflow ignimbrites (i.e., deposited outside of their source calderas) of the Heise volcanic field, which lies to the northeast. The WO-2 borehole terminates in the Black Creek tuff, the most voluminous of the Heise ignimbrite units.

The INEL-1 borehole penetrates approximately 2.4 km (7,900 ft) of rhyolite below about 750 m (2,500 ft) of basalt lava flows and sediments over its total depth of 3.15 km (10,365 ft). Three cored intervals from INEL-1, extending over a depth range of 1.1 to 3.15 km (3,600 to 10,365 ft), yielded rhyolites with overlapping U-Pb ages of ~8.2 Ma (McCurry and Rodgers, 2009; Drew et al., 2013). These deep rhyolites are extensively hydrothermally altered, obscuring some of their textural features. Differences in the phenocryst assemblages and bulk compositions (major and trace elements as well as Nd-isotopic ratios) of core samples suggest these rocks represent separate eruptive or intrusive events. Drew et al. (2013) note

that the rhyolite at 1.5 km (4,900 ft) depth bears striking geochemical similarities to a possible lava-like ignimbrite near Pocatello, Idaho (rhyolite of west Pocatello). If correlative, these deposits display the great volume and dispersal (85-km [53-mi] distance) of some ESRP ignimbrites that were apparently deposited across the entire width of the ESRP. Most of the 8.2 Ma rhyolites of INEL-1 are extrusive and strong evidence for the existence of a Picabo-age caldera in the area near the GRRA (referred to here as the Big Lost Trough caldera).

Based on the distribution, ages, and petrographic characteristics of ignimbrites found in the southern Pioneer, White Knob, Lost River, and Lemhi ranges, as well as those found in the mountains west of Pocatello, Anders et al. (2014) identified the general locations of five calderas of the Picabo volcanic field (Figure 3). Of these, three are located in the vicinity of the GRRA (Figure 7); these are the Little Choke Cherry (LCC; 9.46 Ma), the Kyle Canyon (KC; 9.28 Ma), and the Lost River Sinks calderas (LRS; 8.87 Ma) (ages from Anders et al., 2014). Based on the borehole stratigraphy described above, we also include the Big Lost Trough caldera (8.2 Ma).

Seismic refraction and electrical resistivity surveys traversing the GRRA identify a steeply dipping structure separating the SRP from the sedimentary rocks to the north (Figures 9B and 9C; Pankratz and Ackerman, 1982; Zohdy and Stanley, 1973). The nature of this structure allows for two end-member geologic structural interpretations:

1. A system of four nested calderas butted up against the mountains to the north of the GRRA, with rhyolites persisting to a depth of 6.25 km (20,500 ft). This model is consistent with published estimates of caldera boundaries and eruptive volumes discussed above and the seismic refraction of Pankratz and Ackerman (1982).
2. Subsidence of the ESRP due to the emplacement of a dense, ~10-km (32,800-ft)-thick, mid-crustal sill, based on the attitude of Mesozoic fold hinges north of the GRRA that depict a uniformly dipping flexural surface (McQuarrie and Rodgers, 1998) defining the lower boundary of the ESRP rhyolites and showing extra-caldera rhyolite units thickening to the south. This model is consistent with the resistivity data of Zohdy and Stanley (1973).

The refraction data (Figure 9C) indicate a near-vertical boundary between ~700- and 1,700-m (~2,300- and 5,600-ft) depth separating Paleozoic basement rocks from ESRP rhyolites (Layer 5 in Pankratz and Ackerman, 1982). This feature likely represents the northern boundary of the Big Lost Trough caldera. The nature of the contact is not well constrained by the refraction data, either in regard to the spatial position of the caldera boundary or the structure at greater depths.

The resistivity results (Figure 9B) image a moderately dipping (~30 degrees) structure separating the highly resistive (>500 Ohm-m) basement from a less resistive (20–40 Ohm-m) unit representative of rhyolite tuffs. This boundary is imaged at about 3.7-km (12,000-ft) depth beneath the GRRA and was originally interpreted as the depth to Paleozoic basement by Zohdy and Stanley (1973). However, their survey was completed prior to drilling INEL-1, where the mean resistivity observed in the lower 500 m (1,640 ft) of the borehole was 1,025 Ohm-m, suggesting that the geoelectric basement in the more southern area of the GRRA consists of rhyodacites similar to those observed in INEL-1.

Under both structural models, the data suggest that there is a high probability of encountering rhyolite to a depth of at least 4 km (13,000 ft), and likely much deeper, beneath the proposed FORGE site. Data from all of the nearby deep wells encountered rhyolitic rocks and suggest that within the GRRA intra-caldera rhyolite lava flows and welded tuffs are likely to be encountered between ~1.2 and 4 km (~3,900 and 13,000 ft) depth. Thus, our target lithologies for EGS are likely to be present within the required depth interval of 1.5 to 4 km (4,900 to 13,000 ft). Gaining a better understanding of this northern and potential basal contact is a main focus of planned Phase 2 characterization.

Interpretive End-Member 1 cross sections based on surface geology, borehole data, refraction data, and inferred caldera locations in the GRRA are shown on Figure 10.

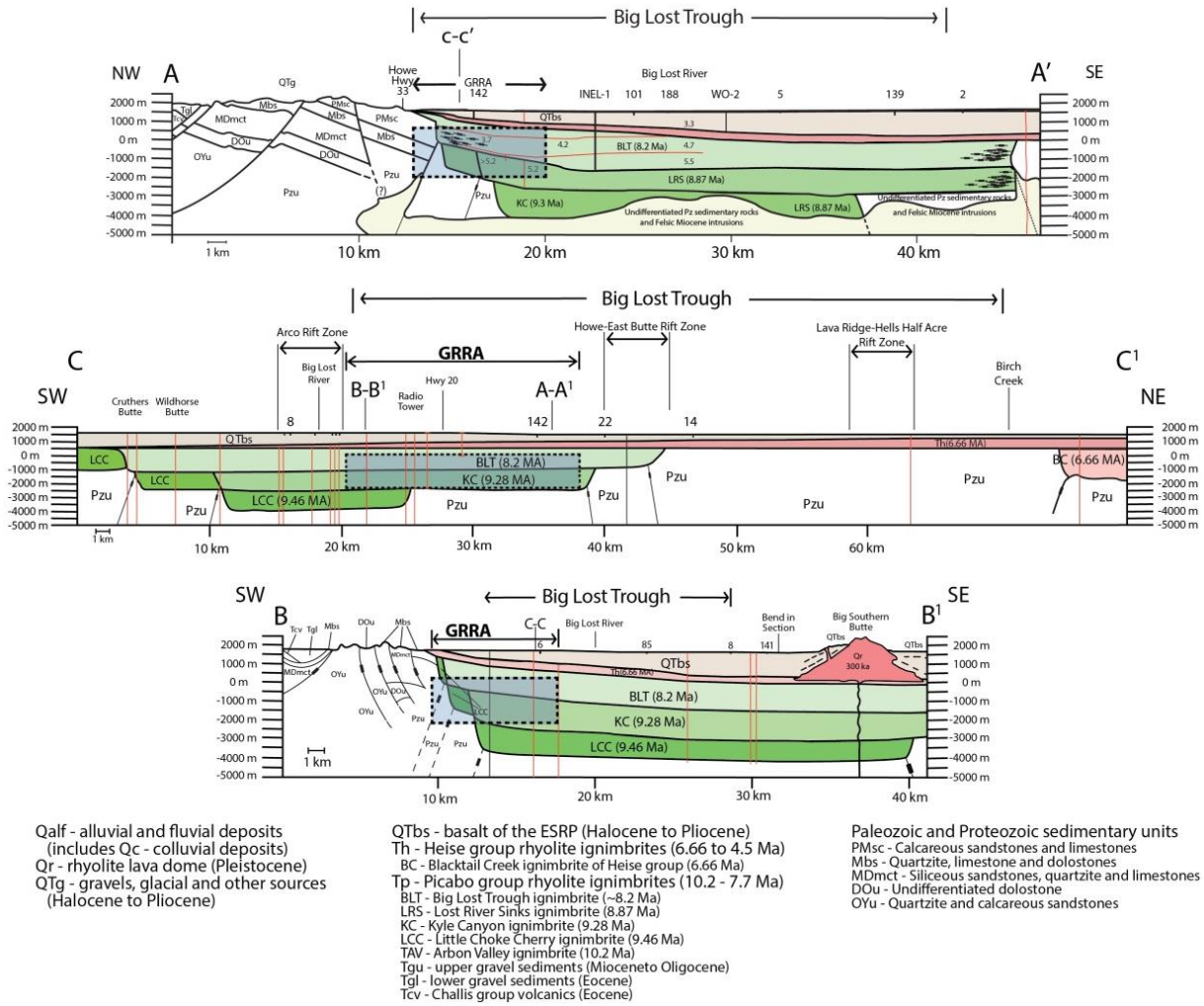

Qalf - alluvial and fluvial deposits (includes Qc - colluvial deposits)
Qr - rhyolite lava dome (Pleistocene)
QTg - gravels, glacial and other sources (Halocene to Pliocene)

QTbs - basalt of the ESRP (Halocene to Pliocene)
Th - Heise group rhyolite ignimbrites (6.66 to 4.5 Ma)
BC - Blacktail Creek ignimbrite of Heise group (6.66 Ma)
Tp - Picabo group rhyolite ignimbrites (10.2 - 7.7 Ma)
BLT - Big Lost Trough ignimbrite (~8.2 Ma)
LRS - Lost River Sinks ignimbrite (8.87 Ma)
KC - Kyle Canyon ignimbrite (9.28 Ma)
LCC - Little Choke Cherry ignimbrite (9.46 Ma)
TAV - Arbon Valley ignimbrite (10.2 Ma)
Tgu - upper gravel sediments (Mioceneto Oligocene)
Tgl - lower gravel sediments (Eocene)
Tcv - Challis group volcanics (Eocene)

Paleozoic and Proteozoic sedimentary units
PMsc - Calcareous sandstones and limestones
Mbs - Quartzite, limestone and dolostones
MDmct - Siliceous sandstones, quartzite and limestones
DOu - Undifferentiated dolostone
OYu - Quartzite and calcareous sandstones

Figure 10. Cross-sections A-A', B-B', and C-C' after McCurry et al. (2016; Appendix A). Cross-section locations are shown in Figure 6. Thin red lines in AA' show the Pankratz and Ackerman (1982) velocity model. Blue shaded region indicates extent of GRRA at a depth of 1.5 to 4 km (4,900 to 13,000 ft).

3. SITE SUITABILITY

In this section, we present data demonstrating the favorable temperature and permeability conditions of target lithologies within the GRRA, meeting the DOE requirements for the FORGE site. We then present additional support for the FORGE site, including the expected drilling conditions, the onsite availability of water, and the land-surface conditions of the GRRA. The subsurface data are primarily from deep Boreholes INEL-1 (3.15 km [10,365 ft]), WO-2 (1.52 km [4,986 ft]), 2-2A (910 m [2,985 ft]), and USGS 142 (573 m [1,880 ft]).

3.1 Thermal Regime at Target Depth

A key requirement for the EGS reservoir at the FORGE site is a subsurface temperature range of 175 to 225°C (347 to 437°F) at a depth of less than 4 km (13,000 ft). Evidence for temperatures at depth beneath the GRRA is primarily from deep boreholes that penetrate the cold, basalt-hosted ESRP aquifer to measure the underlying conduction-dominated geothermal gradients within dry, low-permeability rhyolites. Several boreholes are close to the GRRA and provide direct evidence of the probable temperature at depth (see Table 2), with the three boreholes closest to the selected FORGE location

(INEL-1, WO-2, C1A) being used to bracket our interpretations. Other deep boreholes in the ESRP provide supporting data and demonstrate the high regional heat flux of the ESRP.

INEL-1, located ~2.1 km (~1.3 mi) to the east of the GRRA boundary and 12 km (7.5 mi) away from the proposed site (Figure 7), was drilled in 1979 to investigate hydro-geothermal resource potential near the INL Site (Prestwich and Bowman, 1980). It is the deepest borehole near the site chosen for FORGE operations and is the reference for the lowest observed geothermal gradient. Blackwell et al. (2011) obtained the most precise temperature data for that hole between 1982 and 1990. Blackwell (1990) reports that thermal conditions in the borehole are generally undisturbed and conductive below the aquifer, with a few local perturbations of the temperature profile due to ascending or descending water flow in the wellbore. The gradient in zones with linear temperature-depth relationships is 40 +/- 5°C/km (2.2 +/- 0.27°F/100 ft) in the upper interval and 44.4 +/- 0.1°C/km (2.4 +/- 0.005° F/100 ft) in the deeper interval. Based on thermal conductivity measurements of INEL-1 core samples and the measured borehole temperature gradient, heat flow in this well is 107 mW/m^2. Extrapolation of the deep INEL-1 temperature trend indicates that a temperature of 175°C (347°F) would be reached at 3.8 km (12,500) depth at its location.

Other deep boreholes on the INL Site also have deep, conduction-dominated temperature profiles. These boreholes include WO-2, INEL-C1A, and Coreholes 1 and 2-2A (Figures 7 and 11). The hottest of these boreholes and our reference for highest observed temperature gradient, WO-2, has an average gradient of 76.6°C (4.2°F/100 ft) between a depth of 550 and 1,200 m (1,800 and 3,900 ft) (Blackwell, 1990). WO-2 is 9.1 m (5.7 mi) from the GRRA and 16.2 m (10 mi) from the selected FORGE location. Extrapolating this temperature gradient indicates a 175°C (347°F) target temperature at approximately 2.4-km (7,800-ft) depth. Borehole C1A, which is the other borehole nearest the selected FORGE site, has a temperature gradient between the INEL-1 and WO-2 gradients (Table 2 and Figure 11). The lowest geothermal gradient measure in the region, Corehole 1, is more than 25 km (15.5 mi) to the east of the GRRA and likely represents a cooling trend to the south (McLing et al., 2016).

Extrapolation of these thermal data suggests a temperature of 175°C (347°F) between 2.4- and 3.8-km (7,800- and 12,500-mi) depth. Together, these borehole data demonstrate a high probability that an EGS reservoir temperature of at least 175°C (347°F) will be achieved within the depth range of 1.5 to 4 km (4,900 and 13,000 ft) specified by DOE.

3.2 Permeability at Target Depth

Permeability requirements for the FORGE site are less than 10^{-16} m^2 (100 μD) at EGS reservoir depths. Target lithologies for EGS are best represented by the rhyodacites cored in INEL-1 and rhyolites cored in the WO-2 borehole. Permeability data from these rocks are shown in Table 3.

Bakshi et al. (2016; Appendix F) performed permeability measurements on rock cores at 1,485-m (4,872-ft) and 3,159-m (10,364-ft) depths from INEL-1. Permeability ranged from 6.8×10^{-20} to 1.82×10^{-17} m^2 (0.068 to 18.2 μD). As shown, unfractured permeability was observed to be below the specified range at depths from 1,485 to 3,159 m (4,872 to 10,364 ft) in the INEL-1 borehole.

In addition to the laboratory measurements made on core samples from INEL-1, several hydraulic tests were conducted in the uncased INEL-1 borehole (Mann, 1986), with the deepest testing in the interval from 1,300 to 3,200 m (4,000 and 10,500 ft) below ground surface. The open hole was pumped for 7 days. The average reservoir permeability for the 1,900-m (6,500-ft) open interval was calculated as 7.2×10^{-16} m^2 (730 μD). This pumping test clearly demonstrates that the low permeability specified by DOE extends over a large depth range (1,900 m [6,500 ft]) in the rocks penetrated by INEL-1. Specifically, the data show a high level of homogeneity without the interception of fracture permeability that is common in volcanic provinces. This is a very favorable factor for well drilling and EGS reservoir creation.

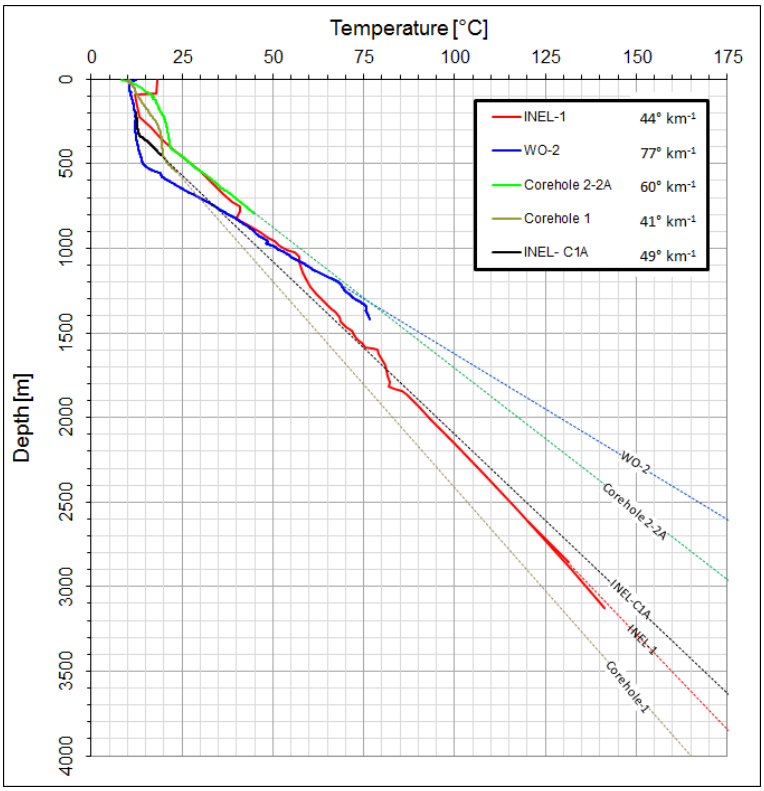

Figure 11. Temperature depth profiles measured in boreholes near the GRRA (solid lines). Conductive gradients are used to extrapolate temperatures at greater depths (dashed lines). Profiles from WO-2 and INEL-1 bracket the estimated depth to the 175°C (347°F) isotherm between 2.4 and 3.8 km (1.5 and 2.4 mi).

Table 3. Permeability measurements in Boreholes INEL-1 and WO-2.

Borehole	Depth in km (ft)	Permeability in m2 (µD)	Method
INEL-1[a]	1.485 (4,872)	1.80 × 10−17 (18.2)	Laboratory
INEL-1[a]	1.485 (4,872)	6.7 × 10−20 (0.068)	Laboratory
INEL-1[a]	1.485 (4,872)	1.94 × 10−19 (0.197)	Laboratory
INEL-1[a]	3.15 (10,365)	8.5 × 10−20 (0.086)	Laboratory
INEL-1[b]	1.3–3.15 (4,265–10,365)	7.2 × 10−16 (730)	Pumping
WO-2[c]	1.340 (4,396)	2 × 10−18 (2.0)	Laboratory

a. Bashki et al., 2016 (Appendix F)
b. Mann, 1986
c. University of Oklahoma (Phase 1 SRGC FORGE proposal)

In 2014, our project team analyzed core samples from W-02 for mechanical and reservoir properties. Core samples from approximately 1,340-m (4,396-ft) depth were measured to have an air permeability less than 2×10^{-18} m^2 (2.02 μD) at 27.6 MPa (4,000 psi) confining stress. Porosity ranged from 3 to 15%. The low permeability values from the laboratory core tests as compared to the field test results (approximately 100 times less permeable) suggest that there is some minor heterogeneity in the permeability in the field, as measured at scales of tens to hundreds of meters.

Lithologies similar to those encountered in INEL-1 and WO-2 are expected at GRRA reservoir depth, and we anticipate a similar range of permeabilities, all of which are lower than the FORGE permeability limits, even at large scales of observation.

3.3 Expected Drilling Conditions

The best reference for estimating conditions for drilling within the GRRA is Borehole INEL-1. It was drilled in search of a hydrothermal resource for use at INL's Idaho Nuclear Technology and Engineering Center, formerly known as the Idaho Chemical Processing Plant. Drilling began on February 15, 1979, and the drilling rig was released on May 27, 1979, yielding an overall drilling rate of 31 m (103 ft) per day. Because the overall rate includes considerable downtime for coring, testing, and breakdowns, the rate is higher for most of the active drilling period. The most difficult and slowest portion of drilling INEL-1 was the upper 300 m (1,000 ft). The overall drilling rate for 0 to 296 m (0 to 973 ft) was 23 m/day (78 ft/day). In contrast, the drilling rate for the interval from 1,490 to 2,990 m (4,900 to 9,810 ft) was 68 m/day (223 ft/day). The contrast in the drilling rate for the upper basalt and the deeper rhyolite is attributed to the high permeability of the upper basalt (which caused loss of circulation), the broken nature of the basalt, and sedimentary interbeds that created unstable borehole conditions and the large-diameter (66 cm [26-in.]) of the surface hole drilled to 465 m (1,524 ft). Advances in drilling techniques, drilling additives, and drilling equipment over the past 40 years will undoubtedly increase the daily drilling rate.

3.4 Additional Favorable Characteristics of the GRRA

Subsidence of the ESRP due to the isostatic effect of the dense mid-crustal intrusive complex created a basin structure that was later filled by many small-volume basalt flows and interbedded sedimentary deposits. As a result, the lithologies of the upper 1.5 to 2 km (4,920 to 6,560 ft) have several characteristics that are beneficial to EGS development at the INL Site. First, the highly fractured basalt lava flows hosting the prolific ESRP aquifer will provide an onsite source of fresh water with low total dissolved solids that is available for drilling operations, reservoir stimulation, and energy production. Second, the interbedded sediments and basalt flows efficiently damp seismic waves, thus minimizing the ground motion due to induced and natural seismicity at the FORGE facility, as described in the FORGE *Preliminary Induced Seismicity Plan* (Templeton et al., 2016). Finally, the flat topography of the ESRP provides level, stable terrain for drilling operations and well pad construction, and this topography simplifies transportation logistics during all phases of construction and production.

4. THREE-DIMENSIONAL GEOLOGIC MODEL

To better visualize the plausible range of geologic structures beneath the GRRA, we constructed three-dimensional (3D) models of the intra- and extra-caldera facies using the JewelSuite software (Figures 12 and 14). To bracket the uncertainty of the boundary that separates ESRP volcanic units from the potentially underlying Paleozoic basement rocks, we present two plausible end-member scenarios. We have a high level of confidence that the actual site lithology will fall within these end members. The first scenario, described in Section 2.2, is based on the inferred distribution of Picabo-aged calderas, all of which have caldera boundaries near the edge of the plain (Anders et al., 2014; McCurry et al., 2016 [Appendix A]). The second scenario is based on the flexural model describing subsidence of the ESRP in response to the mid-crustal sill (McQuarrie and Rodgers, 1998; Rodgers et al., 2002). In this model, the

caldera boundaries are moved to the south, and the top of the Paleozoic basement is assumed to dip uniformly beneath the volcanic section before merging with the nested caldera system, south of the GRRA. We note that although both models are consistent with the available data, the Phase 2 characterization plan calls for seismic reflection and refraction surveys that will improve our understanding of the vertical and lateral extent of the rhyolitic system.

4.1 Model 1

Our first model (Figures 12 and 13) is based on boundaries of Picabo-aged calderas inferred by Anders et al. (2014) and the boundary of the Big Lost Trough caldera, as described in Section 2.2. This model is a 3D extension of the cross-sections shown in Figure 10 and depicts four nested calderas beneath the GRRA. Each caldera is assumed to contain approximately 1 km (3,200 ft) of caldera fill that extends to the top of the ring-fracture normal faults. Deeper, older calderas (Kyle Canyon and Little Lost River) are inferred to tilt more strongly into the plain than the younger Big Lost Trough caldera (following the subsidence constraints of Rodgers et al. [2002]).

Model 1 predicts that our EGS reservoir will be hosted within the 9.28-Ma Kyle Canyon caldera and is supported in part by the seismic refraction model of Pankratz and Ackermann (1982), which depicts a nearly vertical, fault-like structure separating ESRP volcanics from the Paleozoic basement rocks to the north. To the south, along U.S. Highway 20, the resistivity model of Zohdy and Stanley (1973) shows the contact between a 20–40 Ohm-m layer and the >500 Ohm-m geoelectric basement dipping at ~30 degrees to the south and leveling out at a depth of ~3.7 km (~12,100 ft). Along this same profile, our model depicts the structure dipping at ~38 degrees before leveling out at ~4.0 km (~13,100 ft) below land surface, well within the uncertainties in modeling 1D resistivity soundings across a dipping structure. Zohdy and Stanley (1973) interpreted the geoelectric basement to represent the Paleozoic rocks beneath the ESRP volcanic system, which is what our model shows. However, the resistivity observations made in the bottom of INEL-1 are >500 Ohm-m, suggesting that this boundary could represent the transition from welded rhyolitic tuffs to dense, hydrothermally altered rhyodacites.

4.2 Model 2

Our second model (Figures 14 and 15) is based primarily on the flexural surface model of McQuarrie and Rodgers (1998) and the Zohdy and Stanley (1973) resistivity model. In this model, the top of the Paleozoic basement dips at ~30 degrees to the south, and the system of nested calderas is shifted to the south. The depth to the Paleozoic basement is ~4 km (13,100 ft) below the surface, and we note that although the geoelectric basement presented in the resistivity model was originally interpreted as the Paleozoic section, this boundary is equally likely to represent a transition from rhyolitic tuffs to rhyodacite, as indicated by the resistivities measured near the bottom of INEL-1. The northern boundary of the Big Lost Trough caldera, which was inferred from the lithologies found in INEL-1, extends just to the north of the INEL-1 borehole location; there are no calderas beneath the GRRA.

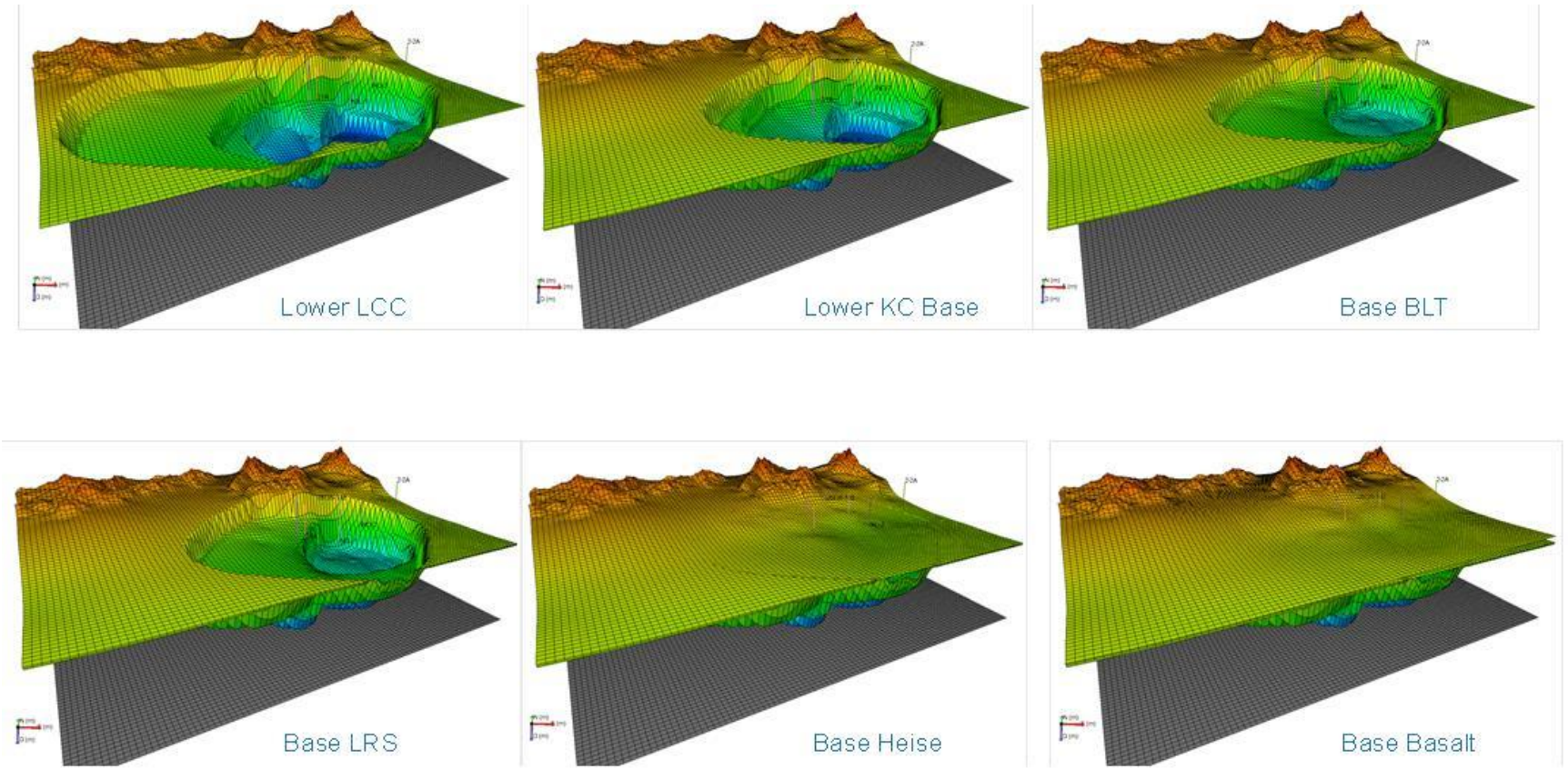

Figure 12. Model 1 as described in the text showing nested calderas against the Basin and Range mountains.

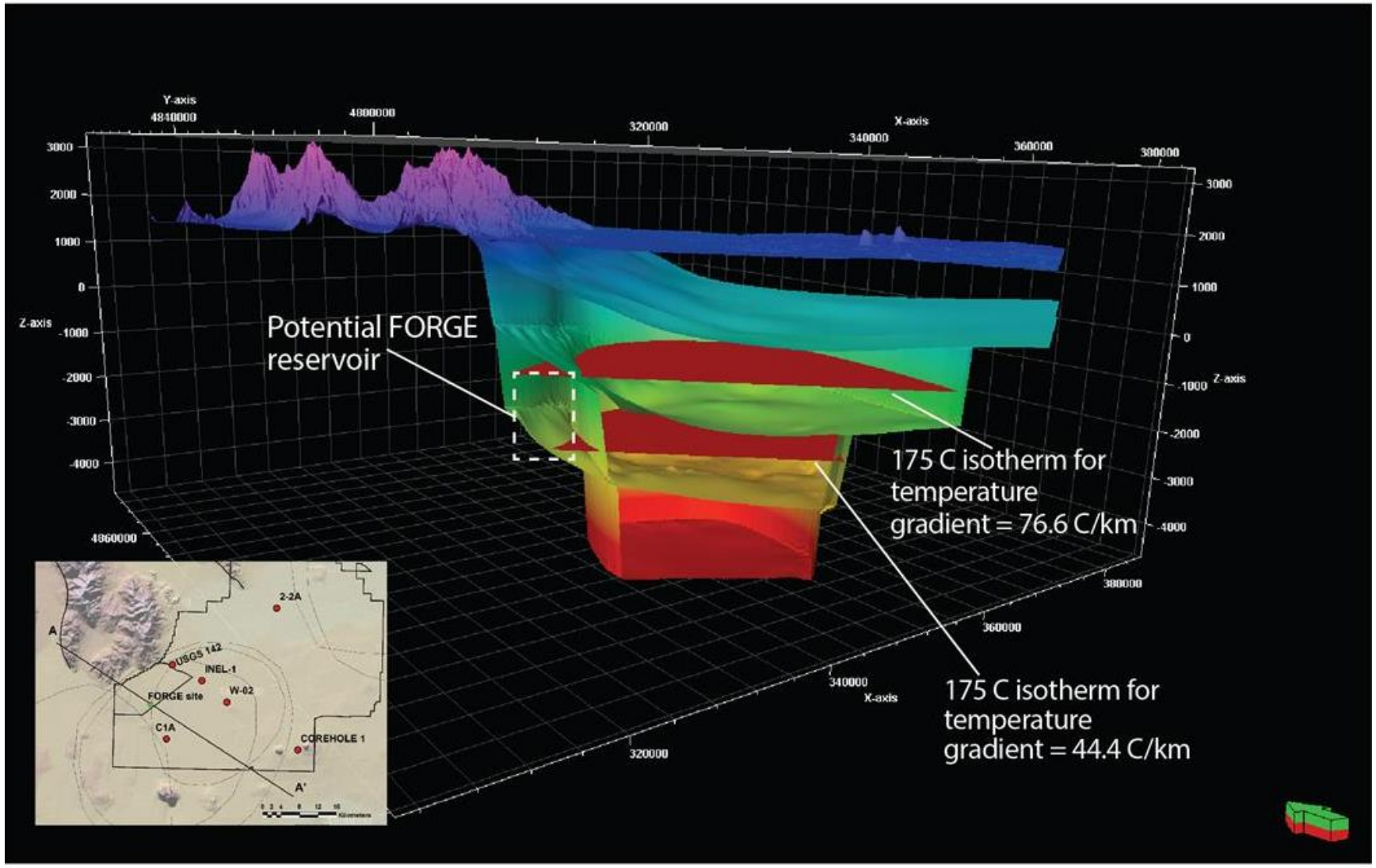

Figure 13. Cross-section of Model 1 along Highway 20 through the GRRA.

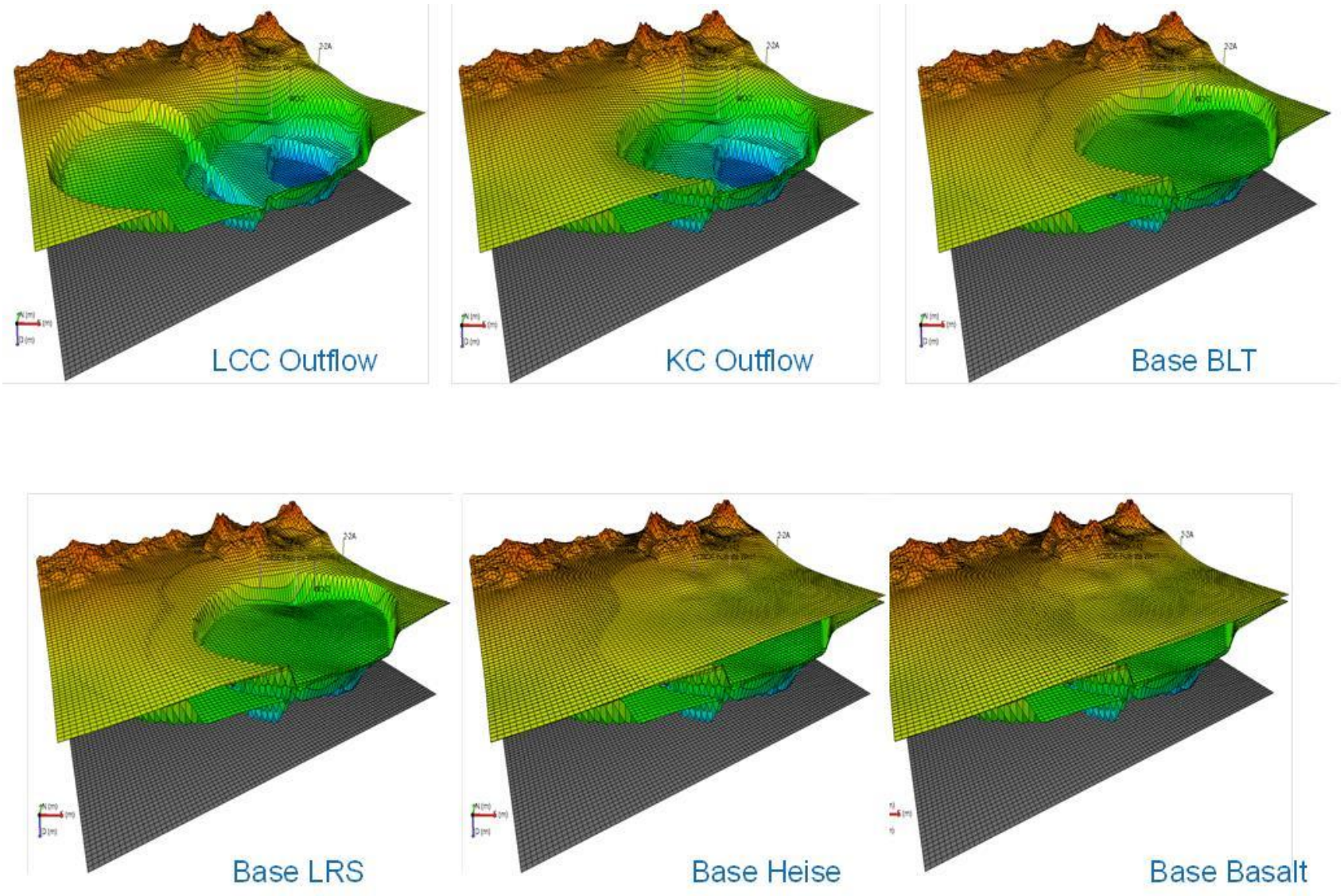

Figure 14. Model 2 as described in the text. Beneath the GRRA, the contact between Paleozoic basement and the rhyolite section is defined by a uniformly dipping flexural surface. Nested calderas are shifted to the south with respect to Model 1.

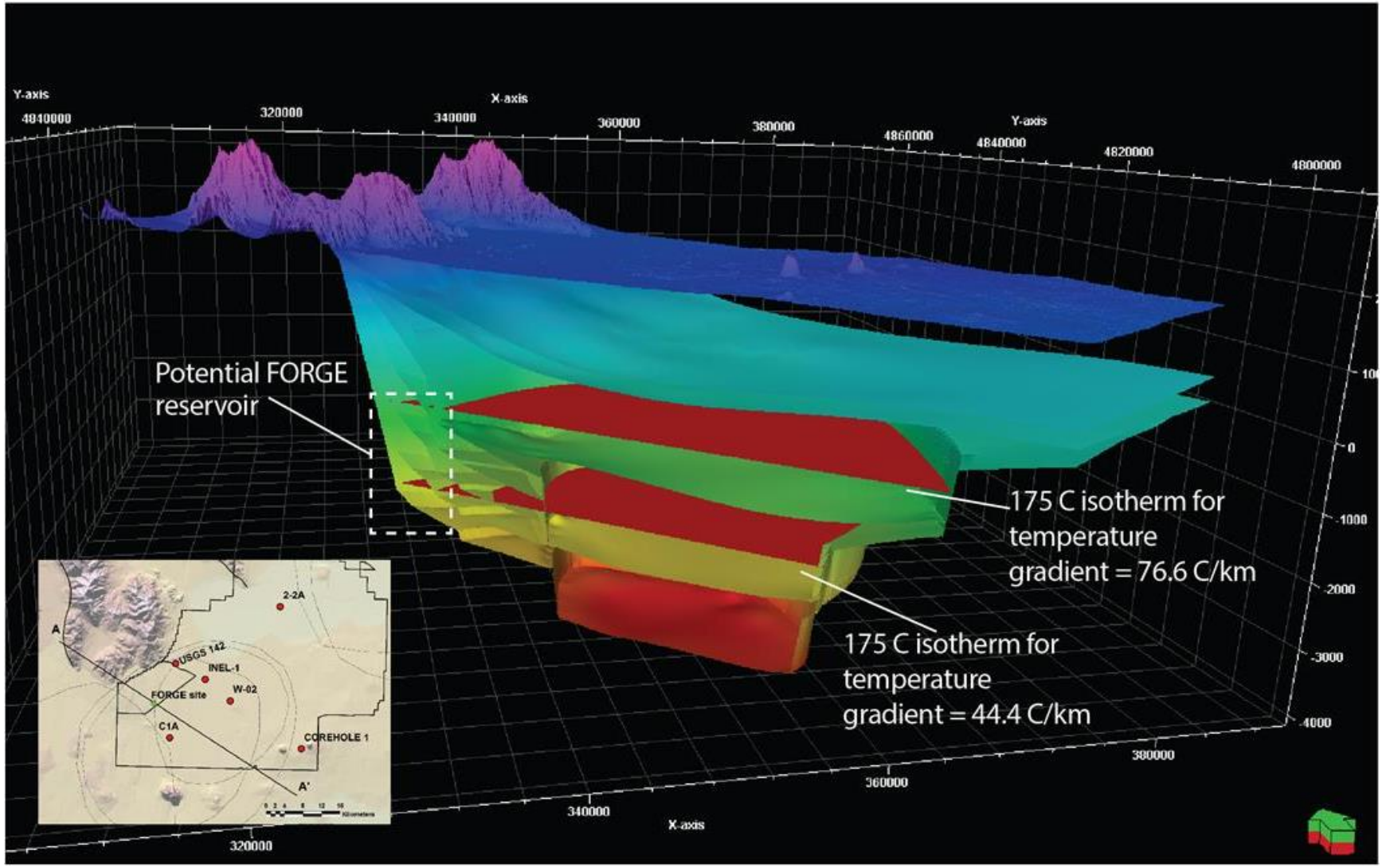

Figure 15. Cross-section of Model 2 along U.S. Highway 20 through the GRRA.

Model 2 differs from Model 1 primarily in the location of the calderas. Because there are no calderas beneath the GRRA in this model, it predicts that our FORGE reservoir will be hosted by extra-caldera rhyolites.

The implications for EGS development within extra-caldera rhyolites can be evaluated by comparing the extra-caldera rhyolites observed in Boreholes WO-2 and USGS 142 to the intra-caldera rhyolites observed in INEL-1. WO-2 bottomed in rhyolite at a depth of 1.5 km (4,900 ft) after penetrating ~350 m (~1,148 ft) of rhyolites, including several thin (meters-thick) ignimbrite sheets and two thick (100- to 200-m [328- to 656-ft]) rhyolite lava flows. USGS-142 penetrated 150 m (492 ft) of rhyolite, a single ignimbrite outflow sheet. Of primary concern for EGS is that the reservoir rock be of low intrinsic permeability (less than 10^{-16} m^2 [100 μD]). In 2014, our project team measured permeability values less than 2×10^{-18} m^2 (2 μD) at 27.6 MPa (4,000 psi), confining stress in samples from 1,340 m (4,396 ft) depth in WO-2. Extra-caldera rhyolite deposits are suitable EGS targets.

For both of these structural model scenarios, we superimposed the bounding thermal gradients from INEL-1 (the colder thermal scenario) and WO-2 (the hotter thermal scenario) to use the 3D model to calculate the volume of rhyolite in the study area that meets the FORGE criteria, that being between 1.5 and 4 km (4,900 and 13,000 ft) and 175 and 225°C (347 and 437°F). Table 4 summarizes the volume calculations, which indicate there is an extremely large target for FORGE operations. Figure 16 shows these volumes graphically.

Table 4. Modeled volumes of rhyolite meeting FORGE suitability criteria under a combination of two structure and two thermal models of the SRP study area.

Structural Model	Temperature Gradient	Volume of Rhyolite in Temperature Range in km^3 (mi^3)
a) Model 1	WO-2	1,200 (289)
b) Model 2 (flexural surface)	WO-2	1,800 (434)
c) Model 1	INEL-1	220 (53)
d) Model 2 (flexural surface)	INEL-1	330 (78)

4.3 Site Selection

As discussed above, there is a huge volume of target rock for FORGE within the SRP study area. In fact, every deep well in the vicinity of the GRRA encountered rhyolitic rocks and exhibited a geothermal gradient that extrapolates to meeting the required conditions for FORGE. The final selection of a site for FORGE in the GRRA comes down to choosing a location with the least possible risk of unforeseen conditions, highest potential geothermal gradient (to minimize drilling costs), proximity to support services and existing infrastructure, and greatest ease of access. The greatest risks posed by the uncertainties in our knowledge of subsurface geology beneath the GRRA are (1) the possibility of encountering Paleozoic sedimentary rocks beneath the volcanics and (2) the possibility of encountering a localized region of high permeability due to either caldera ring fractures or a regional structure, such as a Basin and Range fault.

Because the locations of calderas are uncertain, so are the locations of potential ring fractures. Therefore, avoidance criteria cannot be established based on the available data. The GRRA is located southeast of Lost River fault, which dips to the west (away from the GRRA). The next nearest surface trace of a Basin and Range normal fault is the Lemhi fault (Figure 7), about 20 km (12 mi) north of the central GRRA. Major tectonic features are therefore unlikely to influence subsurface conditions at the GRRA. In addition, the GRRA was identified as an EGS target by the Snake River Plain Play Fairway team, because potential permeable structures are not expected to exist (Shervais et al., 2016).

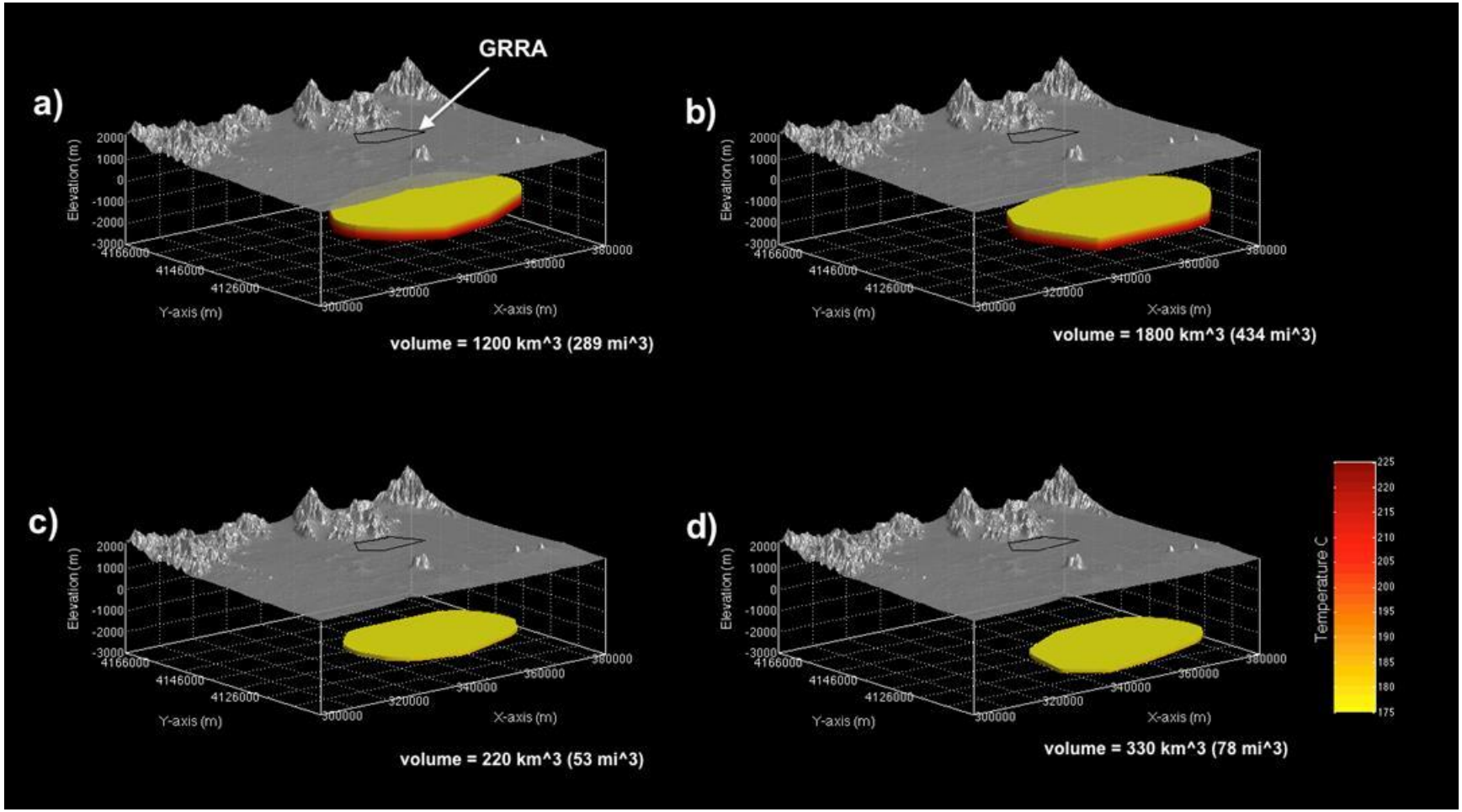

Figure 16. Reservoir volumes from the structural and temperature scenarios, colored by reservoir temperature. Letters a–d correspond to scenarios identified on Table 4.

Conductive temperature gradients measured in deep boreholes near the GRRA suggest that the 175°C (347°F) isotherm lies between 2.4- and 3.8-km (7,900- and 12,500-ft) depth. Given the available data, we can only provide upper and lower bounds on the temperature structure beneath the GRRA or the degree to which the temperatures within this area vary. We do know that the thickness of the rhyolite section increases eastward with distance from the mountain front. Thus, the risk of encountering sedimentary rocks prior to reaching 175°C (347°F) can be reduced by choosing a FORGE location that is far away from the mountain front or choosing a location where the temperature gradient is steepest. We chose a site that is 8.5 km (5.3 mi) from the mountain front along U.S. Highway 20 (Figure 7), where our models depict rhyolitic lithologies to a depth of at least 4 km (13,100 ft).

We can use our 3D conceptual models to make preliminary estimates of the volume of rock that is accessible from the well site and meets the FORGE criteria. To estimate the minimum volume of rock available for FORGE, we use the INEL-1 temperature gradient, which predicts that the 175°C (347°F) isotherm lies 3.8 km (12,500 ft) below the surface, and the structural model depicting the depth to Paleozoic rocks as a uniformly dipping flexural surface. Because FORGE requires the reservoir to be less than 4 km (13,100 ft) from the surface, we use 4-km depth as the lower boundary of the potential reservoir. This scenario provides a 200-m (656-ft)-thick reservoir. Within a radius of 1 km (0.6 mi) from the proposed well site, there is 0.62 km^3 (0.24 mi^3) of available reservoir rock.

An upper bound on the reservoir volume can be found by assuming that the 175°C (347°F) isotherm lies 2.4 km (7,900 ft) beneath the surface (as predicted by Borehole WO-2) and using the structural scenario depicted in Model 1, which has the nested caldera system beneath the GRRA. In this scenario, our reservoir is bound on the bottom by the 225°C (437°F) isotherm, which is predicted to be 3.0 km (10,000 ft) beneath the surface. This scenario yields an upper bound on the potential reservoir volume of 2.1 km^3 (0.49 mi^3).

5. GEOMECHANICAL MODEL

In low-matrix-permeability reservoirs such as the rhyolitic rocks of the INL region, reservoir-stimulation response is controlled largely by the properties of natural and induced fracture networks. In situ stresses, in turn, control the distribution, connectivity, and hydraulic behavior of the fractures. Knowledge of the present-day stress field at the reservoir scale is therefore required for effective and efficient stimulation.

The methodology to characterize the subsurface at the FORGE site integrates three field-scale models derived from a multidisciplinary data set. A geologic model provides the structural framework, lithology, and reservoir properties; a 3D geomechanical model describes the magnitudes and orientations of reservoir stresses, pore pressure evolution, and rock mechanical properties; and a discrete fracture network (DFN) model describes the fracture properties and distribution.

Interpreting rock types and distributions within a volcanic setting is complicated by the heterogeneity and discontinuity of the rocks. However, the common difficulty of heterogeneity is tempered at our FORGE site by the relative homogeneity of permeability as measured in INEL-1. To develop the 3D geologic framework, we will apply geostatistical methods within a structural grid-cell model built using the JewelSuite software. For the base-case model, the identified formation boundaries from drilled wells are matched to interpreted boundaries as a set of well-tie cross sections. This information is used to generate a 3D structural volume with a coherent set of rock types within a region of interest.

A complete geomechanical model consists of estimates of the contemporary in situ stresses (both orientation and magnitude), the rock strength and rock properties, and the pore pressure or formation pressure. In keeping with current paradigms of rock mechanics, tectonophysics, and structural geology, we use the convention that compressive stress is positive. We use this convention because in situ stresses at depths greater than a few tens of meters in the earth—confining pressure in apparatus, and fluid pressure in pores—are always compressive. Positive compressive stress is also the convention used in the field of soil mechanics. This is the opposite of the convention adopted in work on the theory of elasticity

and continuum mechanics where stresses are assumed positive when tensile (Jaeger and Cook, 1979; Zoback, 2007).

In geologically simple reservoirs, a 3D static geomechanical model can be developed based on sufficient well control, with attributes derived from geophysical data and structural information. 3D dynamic geomechanical models are necessary where we need to calculate pressures in more complex reservoirs such as areas with large topographic relief, e.g., beneath mountain ranges or with large lateral density contrasts such as those adjacent to salt bodies. Dynamic models are also required to calculate stress continuity across faults, stress perturbations due to active fault slip, and changes in stress magnitudes with depletion.

5.1 One-Dimensional Geomechanical Modeling Workflow

The initial phase of 3D geomechanical modeling involves the development of calibrated 1D geomechanical models based on well data. The 1D models are an essential step toward creation of a 3D geomechanical model, because they are used to develop and verify static stochastic 3D geomechanical models and 3D dynamic geomechanical finite-element simulations of the more complex or time-dependent aspects of reservoir evolution, e.g., reservoir pressure and temperature evolution with time.

For the FORGE study, offset well data will be utilized to derive 1D profiles of vertical stress, S_v, maximum horizontal stress, S_{Hmax}, minimum horizontal stress, S_{hmin}, pore pressure, P_p, and rock mechanical properties (unconfined compressive strength, T_0, Young's modulus, etc.). For 1D geomechanical models, we assume that one of the principal stresses acts vertically and that the other two principal stresses act horizontally.

To constrain the stresses within the proposed FORGE site, we will utilize a suite of historical and newly acquired well data to map in detail the magnitudes and orientations of in situ stress across the field. The methodology requires characterization of drilling-induced wellbore failures through analysis and interpretation of available wellbore image data. We will use least principal stress values (S3) inferred from leak-off tests or mini fractures, information about vertical stress from density logs, and pore-pressure information obtained by direct measurement or inferred from drilling data, along with the observed wellbore failures to constrain the full stress tensor in the reservoir.

We use a suite of data recorded in the 3.15-km (10,365-ft)-deep INEL-1 borehole to demonstrate our proposed approach (Moos and Barton, 1990). Standard well logs include a density log, neutron porosity, sonic slowness, electrical resistivity, formation temperature, natural gamma ray, and caliper hole-size measurements. In addition, analog acoustic televiewer data were recorded over the interval 2.066 to 3.12 km (6,778 to 10,236 ft) and digitized after logging.

We will compare values of compressive rock strength obtained in triaxial laboratory measurements against effective in situ rock strength determined through the down-hole logging analysis. Log-based rock mechanical properties are derived through application of empirical relationships to the wireline data to calculate depth profiles of unconfined compressional strength (UCS), Young's Modulus, Poisson's ratio, and internal friction. The fundamental INEL-1 log data and the computed geomechanical parameter profiles are shown in Figure 17.

Log-derived rock strength must be calibrated against laboratory triaxial rock-strength measurements. Newly acquired rock-strength measurements (Bakshi, et al, 2016; Appendix F) are plotted Figure 17 and show excellent correlation with the log-derived values. A histogram of computed UCS values over the interval 1.5 to 3.0 km (4,900 to 9,800 ft) yield a P_{10} of 121 MPa and P_{90} of 183 MPa (Figure 18). These values will help to constrain the possible magnitudes of the horizontal stresses based on the presence or absence of wellbore breakouts in the well.

We provide an example of this approach, again based on preliminary modeling of data recorded in the INEL-1 borehole. Figure 19 plots S_{Hmax} versus S_{hmin} for a fixed value of S_v (at a depth of 3.5 km [11,480 ft]) to graphically illustrate all possible stress states as constrained by Coulomb frictional-faulting theory (Moos and Zoback, 1990). The perimeter of the figure polygon indicates the limiting values of S_{hmin} and S_{Hmax} for which the state of stress is in equilibrium with the frictional strength of preexisting faults, a condition often observed in the earth (e.g., Zoback and Healy, 1992). For any point around the perimeter of the polygon, construction of a Mohr diagram would show that the circle would be exactly touching the Coulomb frictional failure line for an optimally oriented fault. We utilize a coefficient of friction of 0.6, consistent with the results from laboratory tests (Byerlee, 1978) conducted for many rock types in the earth's crust, including geothermal reservoirs. The only allowable stress states are those that are either along the perimeter of the polygon or within its interior. This ensures that the in situ stresses never exceed a ratio of shear to effective normal stress that would initiate earthquakes on well-oriented faults.

To apply more rigorous constraints on stress magnitudes using observations of wellbore failure, the plot also displays lines on the frictional-constraint polygon that indicate the combination of values of S_{hmin} and S_{Hmax} (for the given vertical stress, S_v) consistent with wellbore failures observed in image logs. Red lines represent the stresses consistent with observed breakouts (contoured for different rock strengths), and the blue line represents the minimum values of S_{Hmax} for the given S_{hmin} that would be required to generate drilling-induced tensile wall fractures.

For the INEL-1 example, the vertical stress, S_v, at 3,500 m (11,483 ft) is 82 MPa based on integrated density logs recorded for the INEL-1 borehole. The water table measured in INEL-1 is at 91 m (298 ft), indicating pore pressure in sub-hydrostatic at a value of 34 MPa at this depth. Wireline data and drilling experience from the INEL-1 borehole provide an estimate for the least horizontal principal stress, S_{hmin}, of 58 MPa ± 2 MPa at this depth. The lack of leak-off or mini-frac tests in any of the site boreholes currently limits our ability to accurately validate the least principal stress gradient. From the data currently available for this site, the maximum horizontal stress magnitude can only be constrained as transitional between normal faulting and strike slip faulting $S_v \geq S_{Hmax} > S_{hmin}$ (red shaded area in Figure 19) with S_{Hmax} of 89 MPa ± 11 MPa at 3,500 m (11,483 ft). Once we have acquired contemporary wellbore image data, we will use this workflow to analyze data recorded in the newly drilled and existing wells to more precisely constrain stress magnitudes.

In situ stress orientation indicators such as wellbore breakouts and drilling-induced tensile wall fractures were not observed in INEL-1 (Moos and Barton, 1990), precluding measurement of in situ stress orientation from these data. Although drilling-induced thermal fractures (DITFs) would be expected to occur at depth in the deeper INEL-1 borehole, it is likely that the relatively low-resolution circa 1990 acoustic televiewer tool could not resolve these fine-scale features. Our proposed characterization plan requires that more contemporary, higher-resolution wellbore image logging be undertaken at the FORGE site as part of the future logging program to help constrain in situ stress orientation and magnitude. A preliminary geomechanical model for INEL-1 is shown in Figure 20.

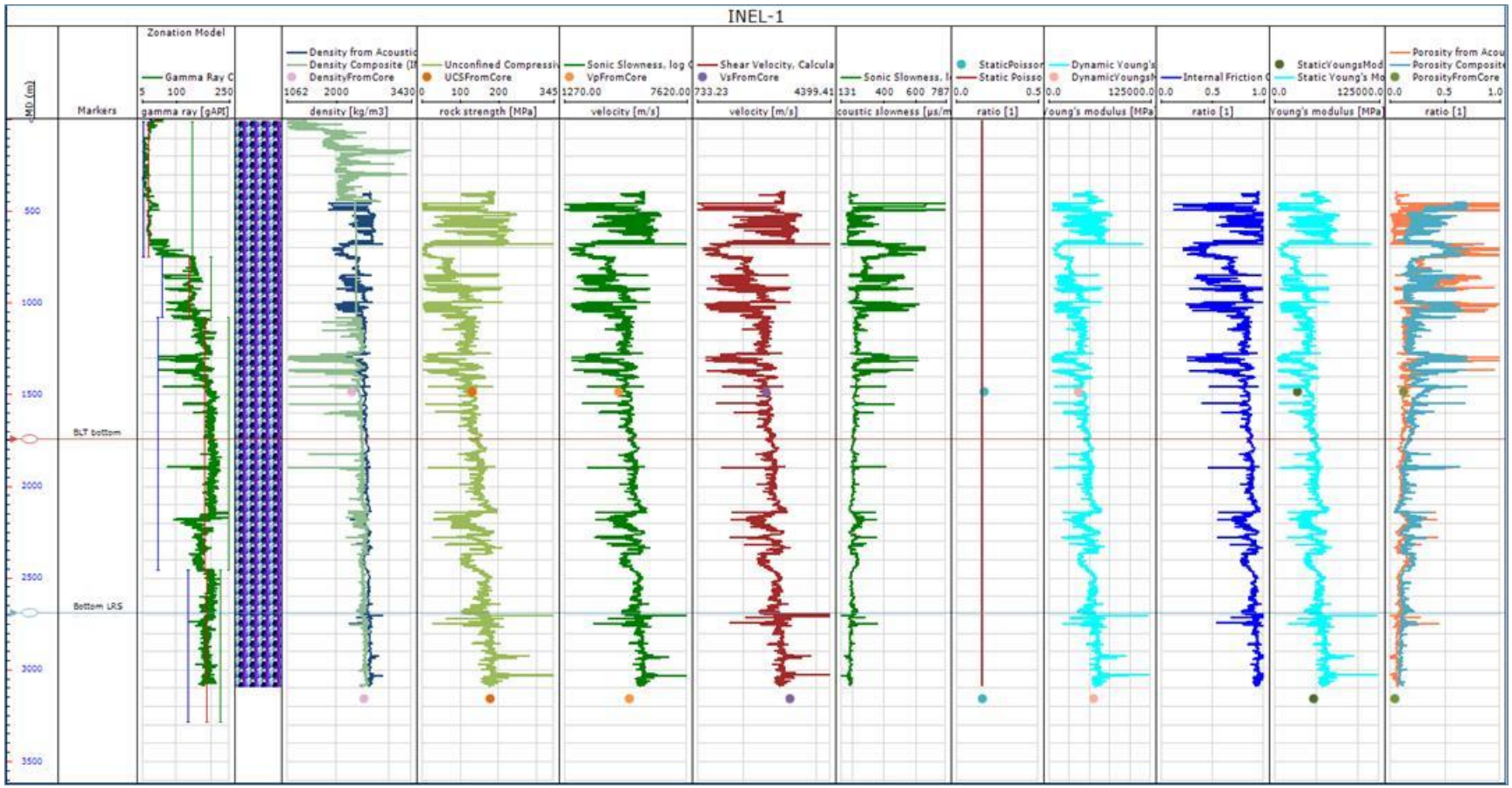

Figure 17. Well log data and geomechanical parameter profiles for INEL-1.

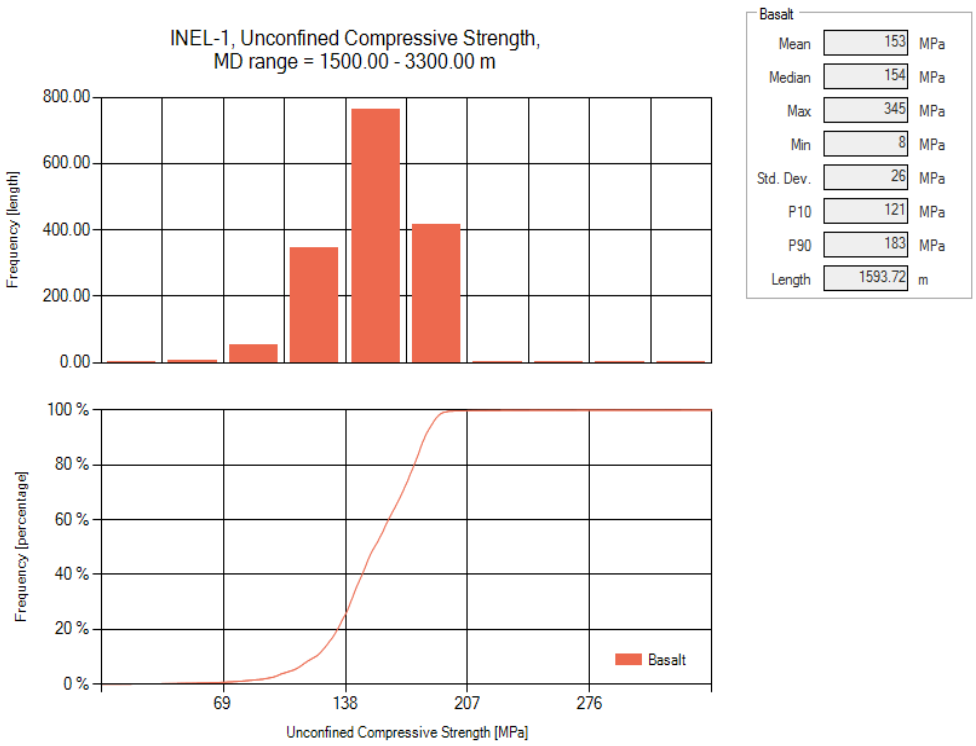

Figure 18. Histogram of log-derived unconfined compressive strength measurements on the interval 1.5 to 3.0 km (4,920 to 9,840 ft) in INEL-1 (upper panel) and cumulative distribution (lower panel).

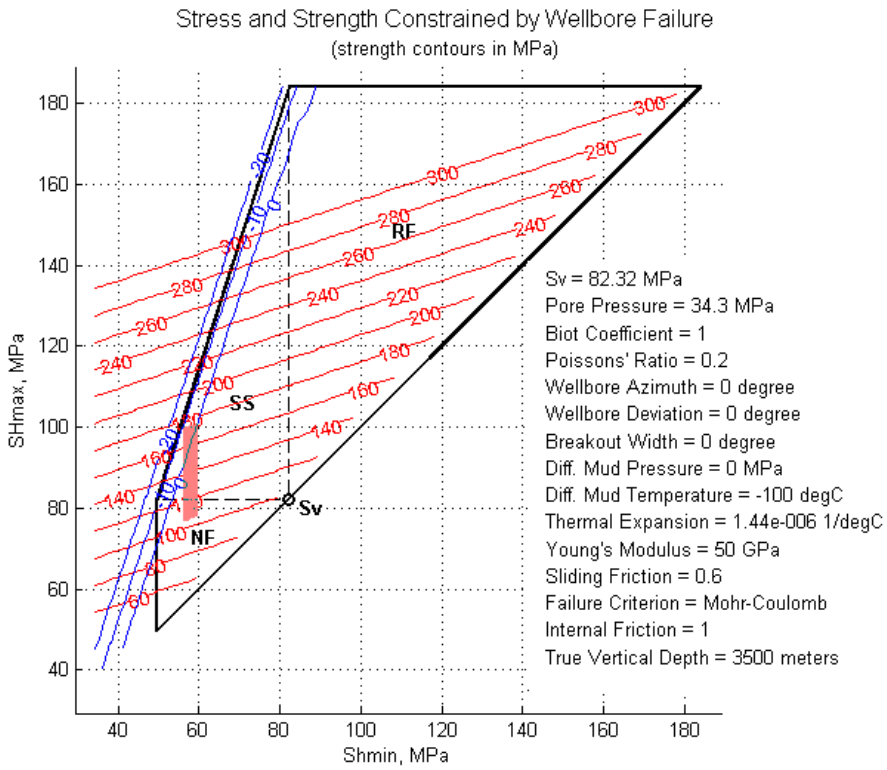

Figure 19. INEL-1 stress state at 3,500 m (11,500 ft) constrained by P_{10}–P_{90} range of rock strength values (MPa).

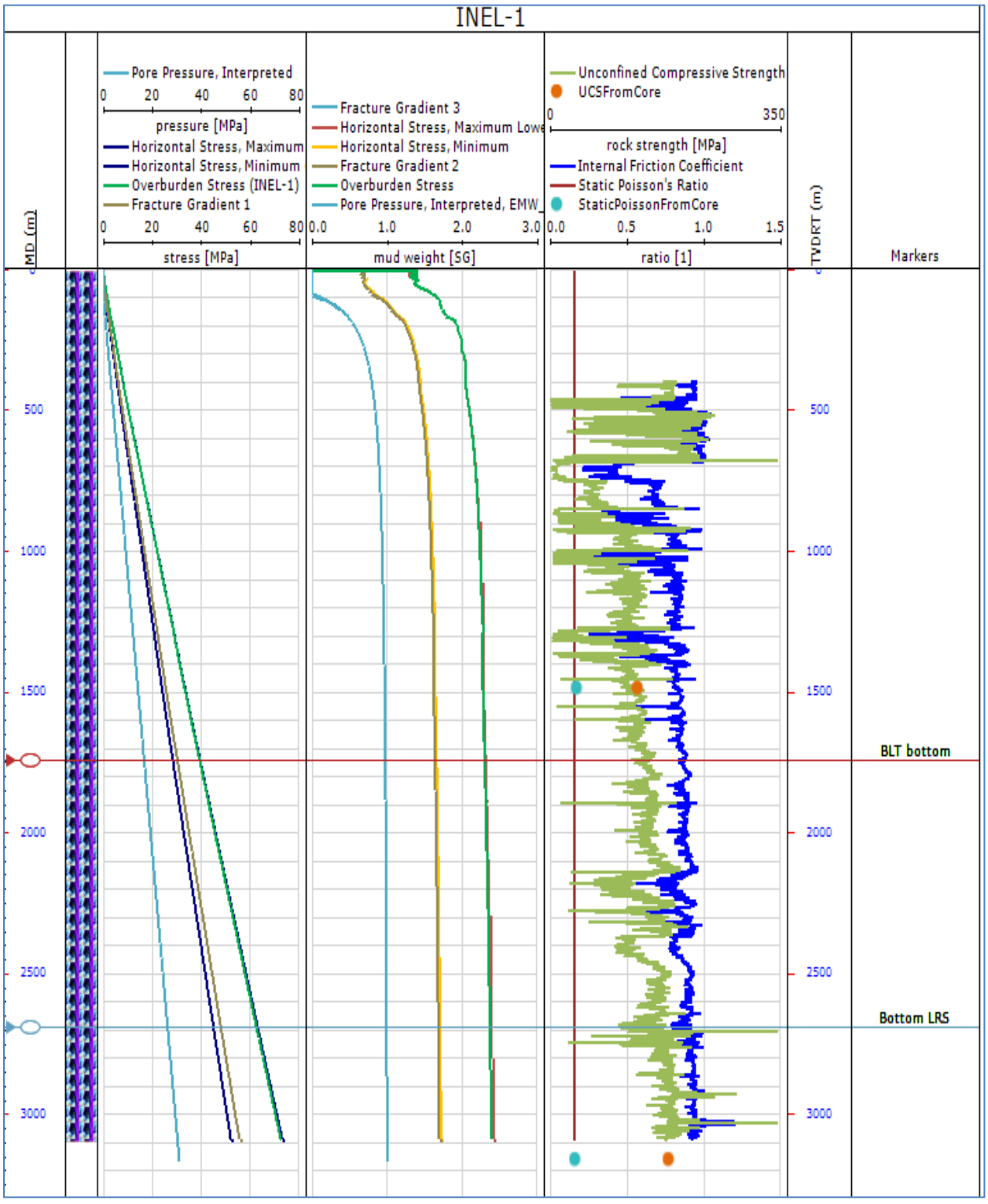

Figure 20. Preliminary geomechanical model for Borehole INEL-1

5.2 Constructing the 3D Geomechanical Model

The FORGE 3D geomechanical model will use the 1D models and the geologic structural model (i.e., subsurface lithologies, stratigraphy, and structure) to create a reservoir-scale geomechanical model, as described in Holland et al. (2010). With moderate structural complexity and relatively homogenous stress fields within the reservoir, reservoir compartment, and overburden, the full workflow can be carried out within the 3D static model. For this method, a 3D grid is used and populated with the properties of the 1D geomechanical model using geostatistical methods. Grana et al. (2016; Appendix B) have developed preliminary correlations for reservoir properties based on the INEL-1 borehole and will populate the model as part of our characterization activities.

The pore pressure and horizontal stresses are calculated using similar techniques used in the 1D models, with calculations done at the vertical, orthogonal pillars of the grid. The population of the grid with the primary properties is analogous to building a reservoir grid but using a much higher resolution over the entire vertical column. Figure 21 shows density mapped to the preliminary structural grid generated for the proposed FORGE site. The contoured horizon is reservoir temperature at 3,500-m (11,500-ft) depth (from Blackwell et al., 2011).

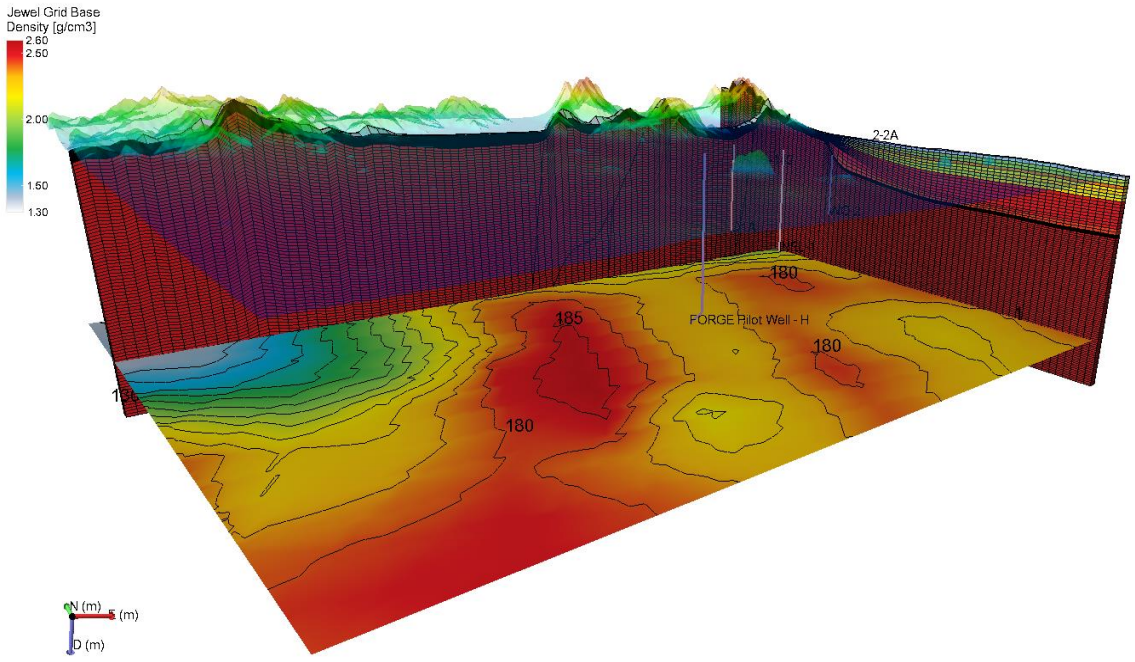

Figure 21. Density distribution (walls) mapped into structural model. Contoured horizon is the temperature distribution (°C) at 3.5 km (11,500 ft) below the surface as predicted by Blackwell et al. (2011).

Under the well-founded assumption that one of the principal stress directions is vertical, the minimum and maximum horizontal stresses are calculated based on effective stress ratios derived from the 1D modeling. These ratios relate the effective horizontal stresses to the effective overburden and are related to the rock property and the stress-field conditions. Populating these ratios allows estimating the horizontal stresses in respect to the local pore pressure, local overburden, and local rock type. As with the stresses, the pore pressure cannot simply be extrapolated along the material layers. Different methods are used, depending on the pore pressure model and the available data (Ward et al., 1994; Bowers, 1995). With the stress model and the primary rock properties in place, other secondary properties such as the fracture gradient can then be calculated from the grid properties at every cell location.

5.3 Application of the Geomechanical Model Wellbore Stability and Hydraulic Fracture Design

Knowledge of the in situ stresses allows the optimization of drilling mud weights, the design of stable wellbore trajectories, the assessment of the stability of uncased wells, and the evaluation of casing schemes. For example, based on the geomechanical model, calculating the safe mud window for drilling wells is straightforward for any well trajectory. We will use quantitative risk assessment to examine the effects of uncertainties in the geomechanical model on the predicted mud-weight window at specific depths in wellbores. Quantitative risk assessment provides the probability distribution for drilling success where achievement of success is defined by engineering design. This information is extremely useful when prioritizing data collection or when determining the new data required to increase confidence in the wellbore-stability analysis results.

In geothermal environments, it is critical that the implications of thermoplastic stress changes while drilling be assessed. Cooling increases the tensile stresses (and decreases the compressive stresses) at the wellbore wall. This affects the development of wellbore breakouts by decreasing the collapse pressure required for compressional failure at the wellbore wall. As the hole warms up after drilling, the compressional stresses increase along with the collapse pressure. Over time, the hole achieves thermal equilibrium and the increase in collapse pressure requires higher mud weight to control excessive wellbore breakout.

Application of the geomechanical model is also important to well completion design. It establishes the requirements to hydraulically fracture the rock at reservoir depth and identifies the optimal trajectory, linkage, and growth of induced fractures (Figure 22).

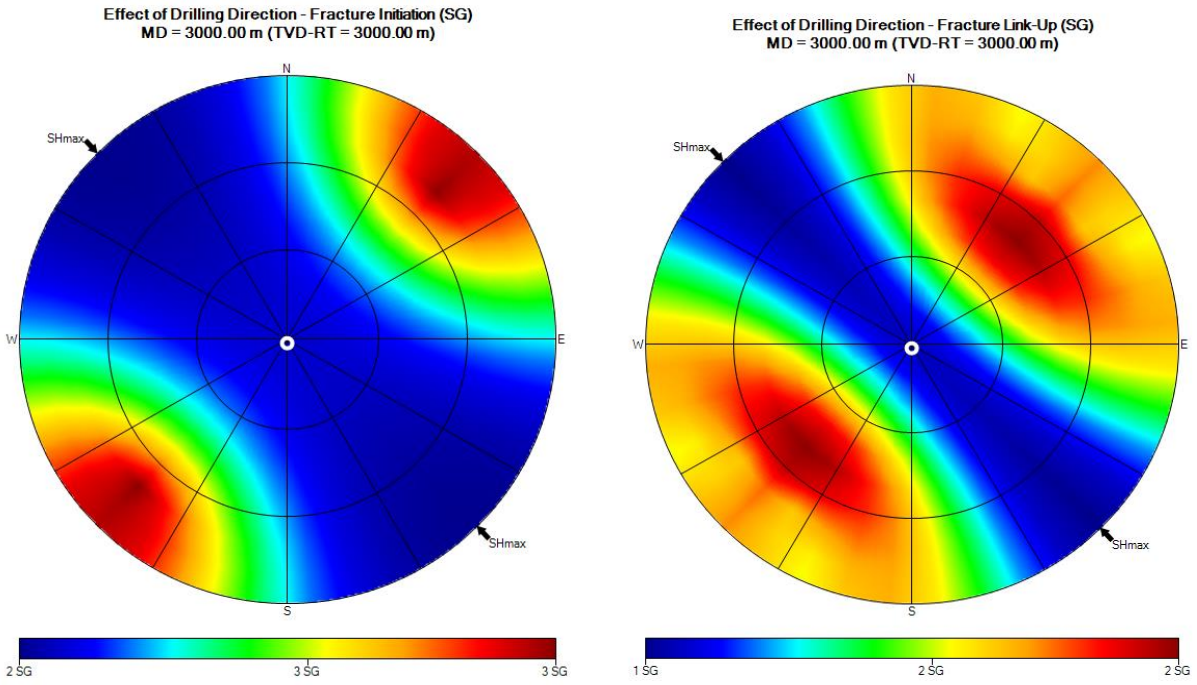

Figure 22. Optimal trajectories to initiate (left) and link-up (right) hydraulic fractures as a function of wellbore trajectory based on analysis from INEL-1.

5.4 Natural Fracture Characterization and Discrete Fracture Network Development

3D natural fracture characterization uses a variety of data to spatially map fracture occurrence, orientation, spacing, and intensity. The primary deterministic data for 3D fracture characterization are wellbore image data, microseismic data, well-test or injectivity data, advanced acoustic logging data, and 3D seismic data. Wellbore imaging tools have dramatically improved in resolution and accuracy over the past 25 years, and our proposed investigation will benefit from these improvements. Wireline tools such as the deep shear wave imaging (DSWI) tool can image fractures and faults up to 30 m (98 ft) away from the wellbore, significantly enhancing spatial knowledge of fracture distribution. Furthermore, high-resolution mineralogical logging can be used to distinguish sealed versus permeable fractures in geothermal reservoirs. Contemporary 3D seismic data analysis methods include determination of fracture attributes based on seismic coherency, augmenting wellbore data with spatial-fracture distribution.

Moos and Barton (1990) analyzed the depth distribution and orientation of fractures in three shallow wells and INEL-1 using acoustic televiewer images. The data provide an assessment of flow stratigraphy within the basalts, revealing a characteristic lithostratigraphy within each flow unit. A sampling of the depth, orientations, apparent apertures, and host lithologies of macroscopic fractures within the interval 2.067 to 3.121 km (6778 to 10,236 ft) from the INEL-1 wellbore is available from the 1990 wellbore-image analysis (Figure 23).

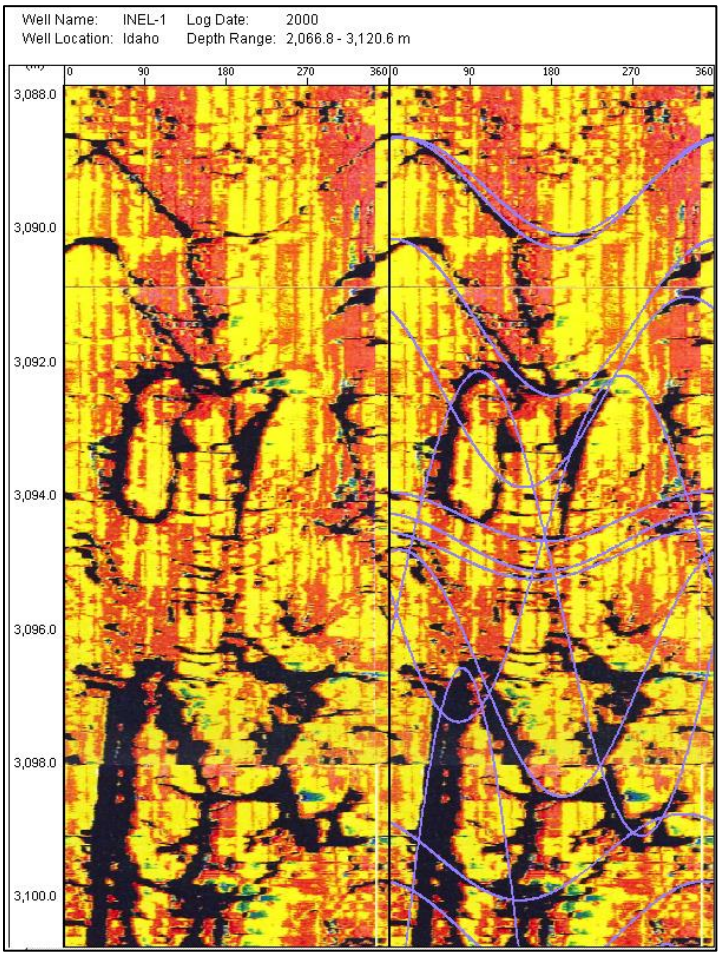

Figure 23. Typical circa 1990 wellbore image data recorded in Borehole INEL-1.

In the rhyolitic welded tuffs, there are two main fracture populations:

1. Striking northeast-southwest and dipping steeply to the northwest
3. Oriented roughly north-south and dipping steeply to the west (Figure 24).

In the deeper rhyodacites, there are three dominant fracture populations:

1. Northeast-southwest set, steeply dipping both northwest and southeast
2. East-northeast set, dipping to the south
3. South-southeast set, dipping to the north (Figure 25).

The variability of fracture trends revealed by the image data analysis indicate there is a well-developed network of existing fractures that can provide a base reservoir volume for stimulation.

Steeply dipping fractures may be relict structures related to caldera collapse and thus not formed in the present-day stress field. Shallow-dipping fractures were also found. Fracture frequency does not systematically decrease with depth in the study interval. There appears to be a cyclic repetition of high-density fracturing followed by moderate to low fracture density throughout the logged interval of INEL-1 (Figure 26). The repetition is probably due to cyclical deposition and cooling of rhyolitic tuffs and lava flows, reflecting their compositional and lithologic variations. Detailed analysis of the fracture distribution will inform the stochastic discrete fracture network (DFN) model.

5.5 3D Fracture Characterization – Discrete Fracture Network Modeling

3D fracture characterization is focused on developing a conceptual model for natural fractures by interpreting a hydro-structural model for the site and developing a 3D static DFN model. The static DFN describes where fractures are expected to occur in 3D, their intensity (measured as fracture area per unit volume), their statistical distributions of size (i.e., extent), and orientations. The DFN is built using the 3D geomechanics study, geologic model, various other well logs, microseismic and operational data, drilling logs, and interpretations. The model is then calibrated on dynamic information gathered during injection experiments in specific wells. These low-flow-rate injection tests are used to characterize the hydraulic properties of the fractures and their width, stiffness, and strength—properties that are often difficult to quantify—as shown by the typically large uncertainties in predicted response to stimulation of fractured reservoirs. Model iterations include adjusting DFN parameters such as intensity, size, and aperture. Post-stimulation tracer tests of dipole injection between two wells can also be used to validate the resulting DFN model parameterization and to select stochastic realizations of solute transport that are most similar to those observed.

An example of our DFN workflow applied to the Wayang Windu Geothermal Field in Indonesia is shown in Figure 27 (data courtesy of STAR Energy). Based on wellbore data, image logs, production logs, lithology, and microseismic data recorded under stimulation, the model provides fracture intensity and distribution, as well as hydraulic aperture. Stochastic DFN models are generated to find the optimal fit to the observed data. By integrating the results from our 3D geomechanical grid with the DFN fracture distribution, we can determine—using Coulomb failure analysis—the proximity to frictional failure of fractures in the DFN. Mapping these fracture intersections to the reservoir volume provides a means to identify “geomechanical sweet spots,” zones with the highest density of stress-sensitive fractures for stimulation design (Barton et al., 2013).

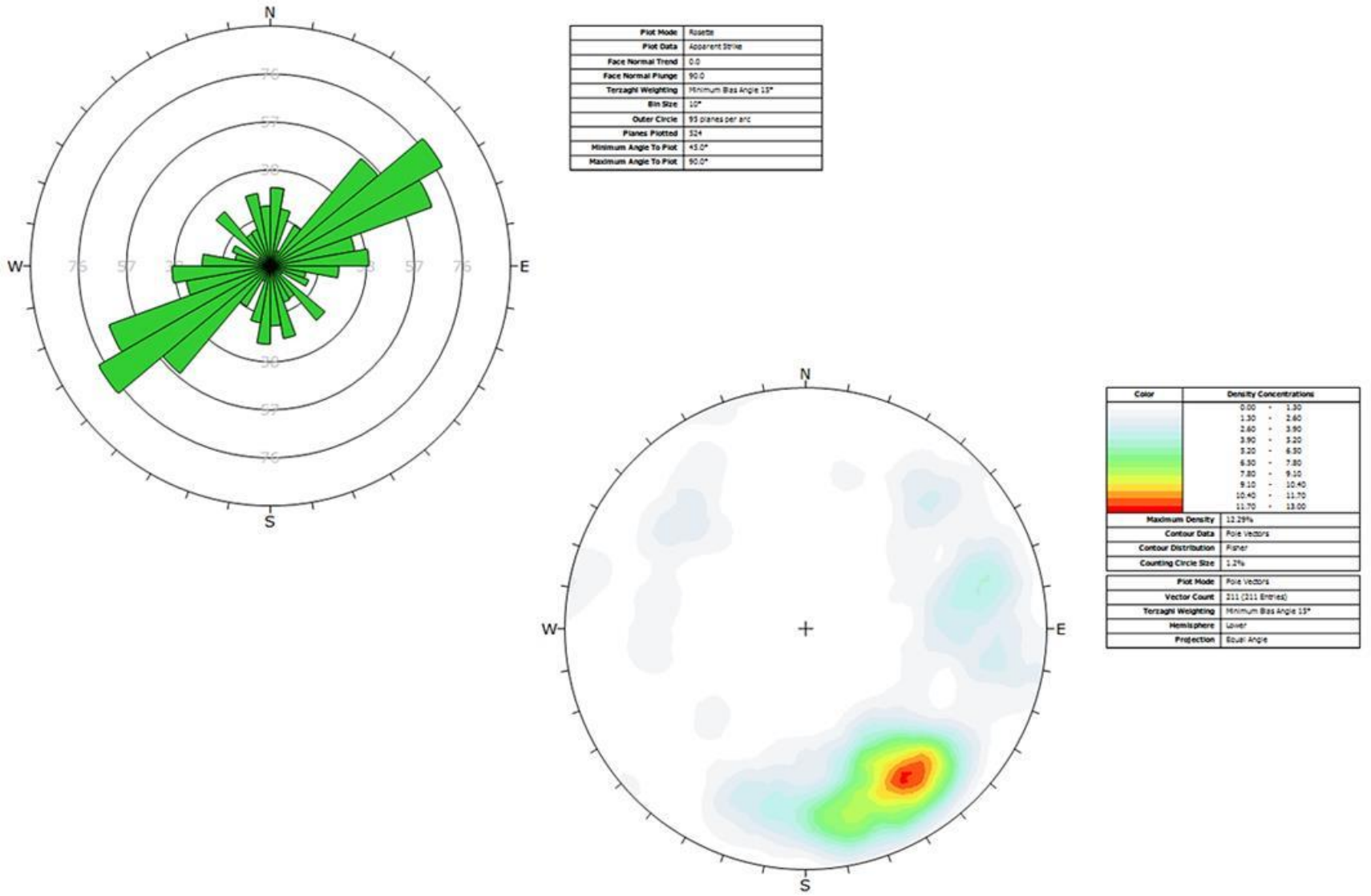

Figure 24. Fracture distribution derived from rhyolite, Borehole INEL-1.

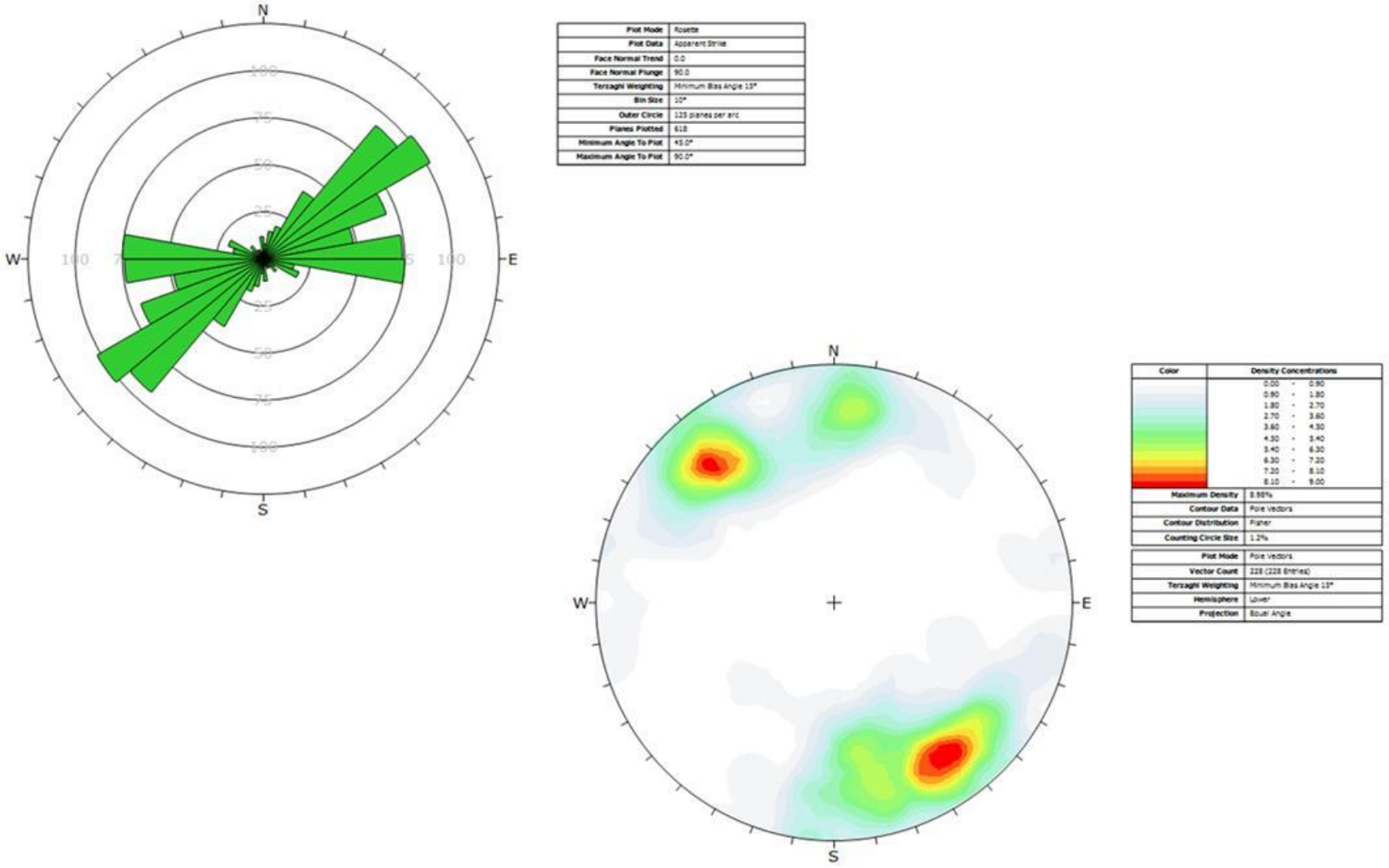

Figure 25. Fracture distribution derived from rhyodacite, Borehole INEL-1.

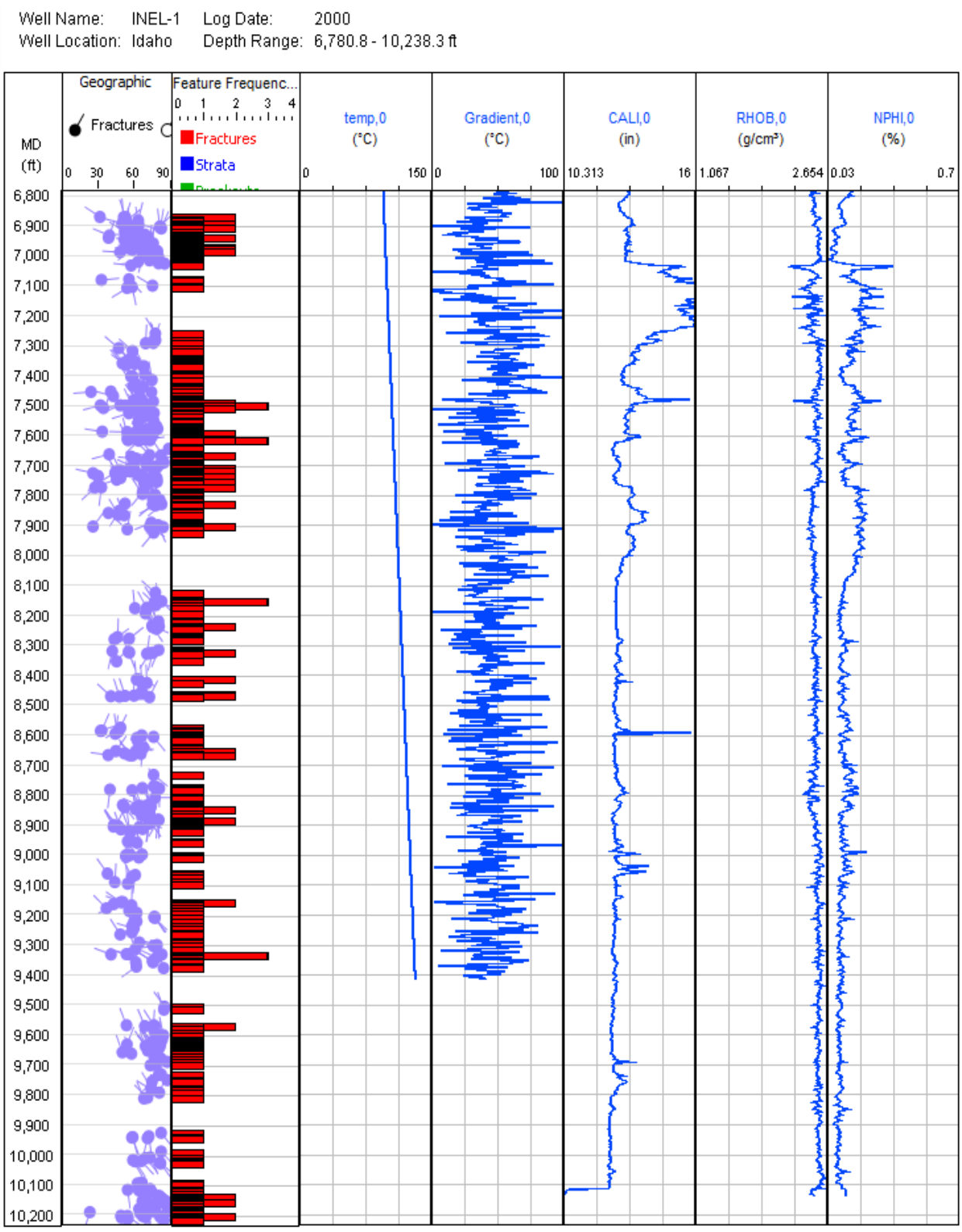

Figure 26. Fracture distribution (tadpole plot), fracture frequency per foot and associated well logs over the interval 2.06 to 3.1 km (6,780 to 10,200 ft) in Borehole INEL-1.

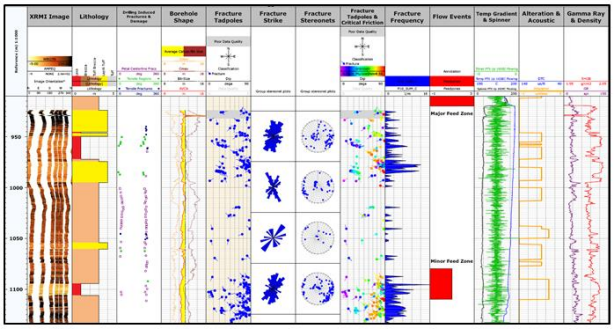

Fracture characterization from wellbore data

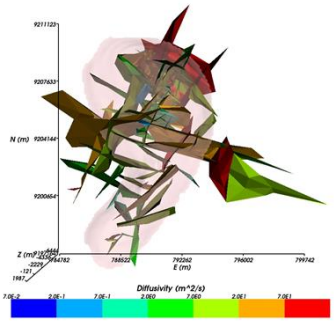

Hydro-structure characterization from MEQ and pumping data

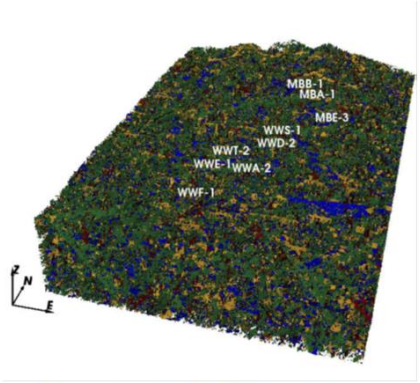

Fracture trends of a DFN model

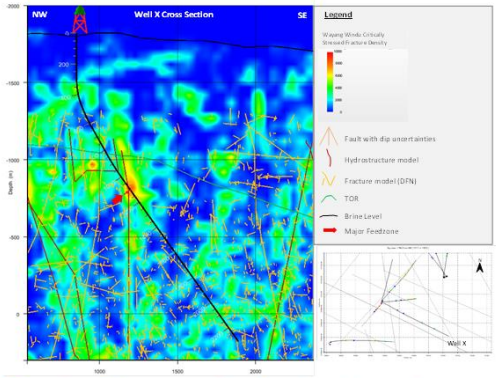

Density of stress sensitive fracture intersections

Figure 27. DFN modeling workflow applied to the Wayang Windu Geothermal Field in Indonesia (data courtesy of STAR energy).

Another important application of the DFN is its use for more sophisticated dynamic modeling of hydraulic fracture design. A priority objective for EGS development is creating the reservoir via hydraulic fracturing to extract heat. Fully 3D fracture modeling software is required to accurately model fracture growth in complex, unconventional fractured formations. Under stimulation, the hydrofrac provides the initial connection to the wellbore. Natural fractures connect when slip occurs, initiating microseismic activity. For these studies, we will deploy the new Baker Hughes ARGOS™ software to fully monitor the introduction of fracture fluids into the formation through preexisting fractures during stimulation.

5.6 Implications of the In Situ Stress State and Fracture Network for Stimulation of the SRP Geothermal Reservoir

Effective production from EGS reservoirs requires stimulation of preexisting natural fractures, but it is also accompanied by hydraulic fracturing that creates high-conductivity pathways back to the producing well. These are often held open after stimulation using proppants injected with the stimulation fluid. Because injection pressures exceed the least stress, the stimulated volume creation is likely here to be through a combination of shear stimulation and growth of new hydraulic fractures, enabling more efficient connections within the preexisting natural fracture system.

For the 1-D geomechanical data for the INEL-1 borehole we evaluated the mud pressure at which a tensile fracture starts to form on the wellbore wall for a given tensile strength. Figure 28 shows that wells highly deviated in the direction of S_{hmin} require higher stimulation pressures than those drilled in the direction of S_{Hmax}. The results indicate that well stability will not be an issue on the ESRP, and high mud weights will not be required.

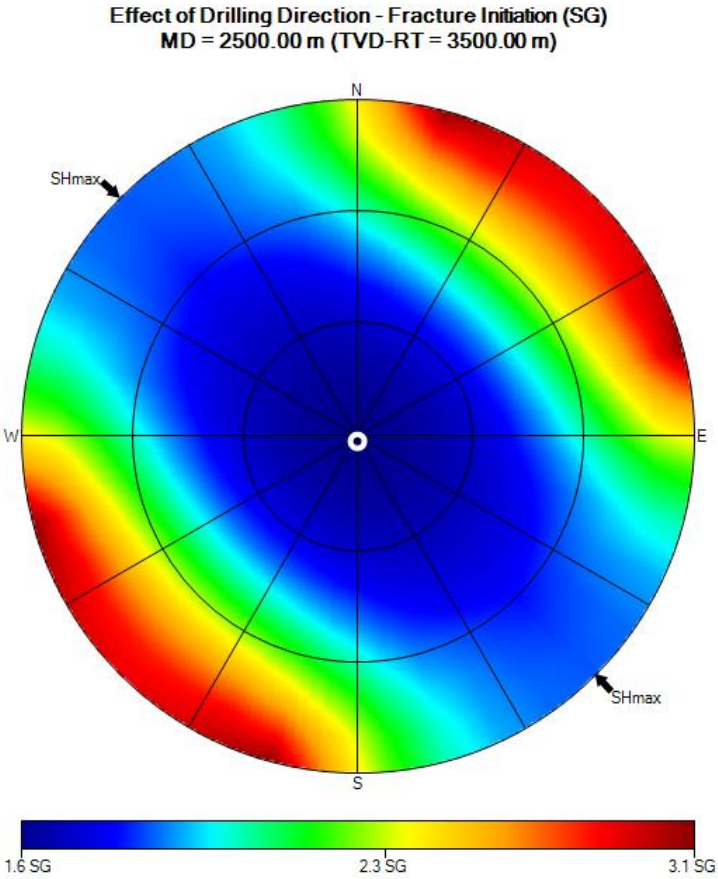

Figure 28. Pressure as a function of wellbore trajectory; vertical wells are plotted in the center, and horizontal wells plot along the outside edge. The grid in the plot is aligned with the stress symmetry. Geographical north is at the top of the plot, and the two arrows pointing into the plot indicate the azimuth of the maximum horizontal stress.

Similarly we can use the INEL-1 1-D geomechanical model to estimate the optimal trajectory to stimulate the preexisting natural fracture system (Figure 29). The approach we use for modeling the connected stimulated network is the observation, validated by numerous studies (e.g., Barton, 2007), that fracture conductivity is enhanced when fractures have slipped under a critical state in which the shear stress is sufficient to cause the fracture to fail in shear. Explicitly, we define this condition using a Coulomb failure criterion in which slip occurs when $\tau > \mu\sigma_n - S_0$ (τ is the shear stress acting on the fracture, μ is the coefficient of sliding friction, σ_n is the effective normal stress, and S_0 is the cohesion).

Under natural conditions (Figure 29, left), most fractures are nearly completely closed, as σ_n is always greater than zero in situ. Raising the fluid pressure in preexisting natural fractures decreases effective stress normal to the plane of the fractures thereby causing an increase in the number of fractures that are critically stressed and thus can slip (Figure 29, right). Because fracture walls are rough, slip is coupled with an increase in the fracture aperture, which enhances conductivity. As stimulation pressure continues to increase to values above the fracture gradient, Mode I (extensile) fractures will open and, with continued pressure increases, the pre-stimulated shear fractures will also open. When the pressure drops after stimulation is complete, shear fractures remain open (they self-prop), but Mode I fractures will re-close unless proppant or other means are used to maintain their newly created aperture.

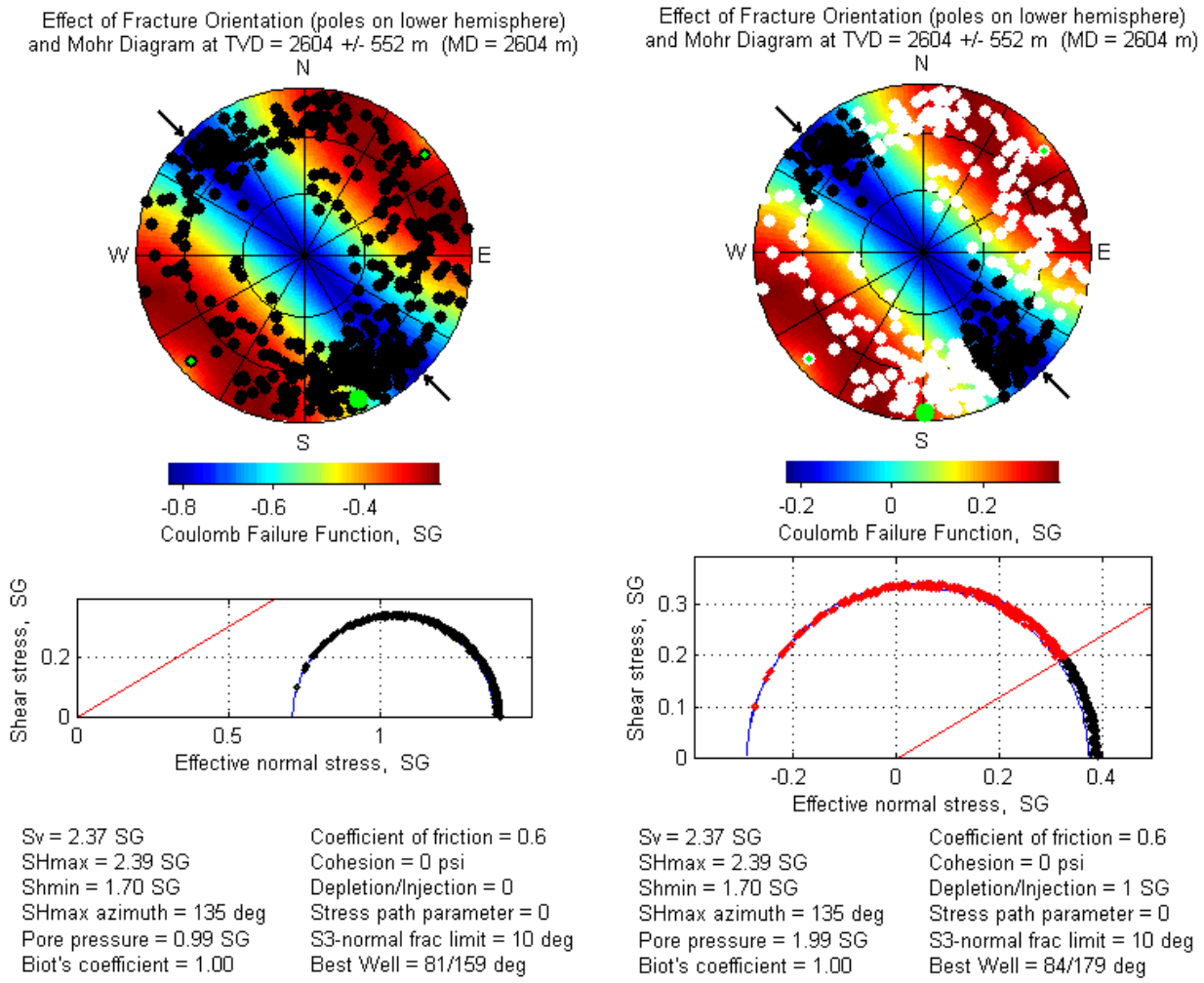

Figure 29. Measured fractures in Borehole INEL-1 before and after the fluid pressure has been increased by 1 SG (~ hydrostatic pressure) to almost 2 SG, where white indicates natural fractures that could be opened by shear displacement if the fluid pressure in them reached this level during hydraulic fracturing. In practice, hydraulic fracturing with a pressure of 2 SG where the fluid is injected into the rock would not open all of the fractures indicated in white. The lower Mohr circles show the pre- and post-stimulation effective stresses (total stress minus pore pressure).

We will use Baker Hughes's new ARGOS™ fully 3D fracture modeling software to establish our planned development of a fully calibrated 3D reservoir geomechanical model and coupled DFN model; well design criteria, including optimal trajectories; landing points; frac staging; spacing; sequencing; and proppant schedules (Figure 30). ARGOS is a multiphysics platform for hydraulic fracture modeling in complex, unconventional formations such as EGS. Importantly, the interoperability between JewelSuite and ARGOS enables a powerful workflow for fracture modeling in complex unconventional formations. ARGOS can read directly from JewelSuite FORGE geomechanical models, various meshes, and wellbore designs required for simulation. ARGOS simulation results can then read by JewelSuite for visualization and analysis.

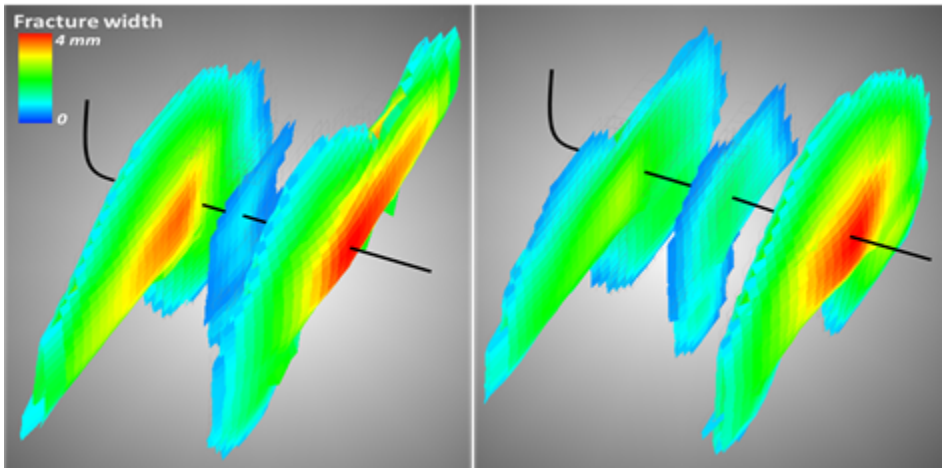

Figure 30. 3D modeling reveals that the effects of varying cluster spacing on fracture growth can be highly asymmetric in laterally variable media.

6. PHASE 2 CHARACTERIZATION PLAN

Characterization efforts will focus on addressing the greatest risks posed by the uncertainties in the subsurface geology; these uncertainties are considered to be (1) the depth required to reach 175°C (347°F), (2) the possibility of encountering localized sedimentary rocks, and (3) the possibility of encountering a localized region of high permeability (e.g., faults and fractures). The characterization activities described in this section will result in the collection of data that will eliminate or greatly reduce the risks to the project prior to advancing to Phase 3.

Our characterization approach is to analyze direct and indirect indicators of the geologic regime and the drilling environment to ascertain the suitability of the GRRA for EGS. We will use state-of-the-art methods for geophysical imaging during Phase 2B coupled with innovative data integration and modeling. The Phase 2B results will be used to optimize well design for Phase 2C, which will include the drilling of two wells: (1) a deep 3- to 4-km (9,800- to 13,100-ft) characterization, or "pilot," well and a shallow 250-m (820-ft) water-supply well. The pilot well will be used in Phase 2C to refine the conceptual model of the site's geologic structure, thermal profile, and rock physics characteristics for EGS. During Phase 2B, we will also reenter the existing 3.15-km (10,365 ft)-deep INEL-1 borehole to obtain information on the geological stress regime and to collect water samples necessary for understanding the geochemistry of native fluids and the interactions of circulated fluids in the proposed EGS within the stimulated fracture network.

6.1 Phase 2B Characterization Activities

We will conduct the following Phase 2B characterization activities.

6.1.1 High-Resolution Gravity

One of our first Phase 2B activities will be to collect of a series of six high-resolution gravity (100-m [328-ft] station spacing) profiles. These will help to identify the maximum gravity gradient created by the density contrast between rhyolite deposits and ancient marine sediments. The high-resolution gravity lines will reduce the uncertainties in depth and location of the volcanic/Paleozoic contact. Several gravity lines will originate at the base of the Lost River Range and extend southeastward out into the SRP, with one extending to INEL-1. One or more gravity lines will extend northeast to southwest to tie the lines together.

6.1.2 Light Detection and Ranging

We will use light-detection and ranging (LIDAR) instruments from INL and the Center for Advanced Energy Studies to generate a precise, 3D image of the earth's surface for the operations pad and surrounding area. This information will be used as a baseline for the topography prior to field disturbances.

6.1.3 Interferometric Synthetic Aperture Radar

We will perform a basic interferometric synthetic aperture radar survey using available commercial data (e.g., freely available Sentinel C band or ALOS-2 L band) to examine possible ground deformation in the area from field activities and to establish a baseline for future work. The open-source package GMTSAR (Sandwell et al., 2011) will be combined with a time-series analysis and an available high-resolution digital elevation model (and perhaps the LIDAR map described above).

6.1.4 Passive Seismic

We will analyze data from our planned eight-station temporary seismic array, as described in the FORGE *Preliminary Induced Seismic Mitigation Plan* (Templeton et al., 2016), in several ways to search for microseismicity and characterize the subsurface structure. Basic detection/association routines (short- and long-term averaging) will be applied to detect microseismic events. Locations and associated error estimates will be generated for any observed events, as well as moment tensors as possible. We will analyze signals from regional or teleseismic events using receiver functions to refine basement depth and crustal velocity structure. An advanced detection routine (matched field) will be applied to search for exceptionally small events. In parallel, a seismic interferometry study using correlation of ambient seismic noise will be conducted using continuous noise recorded by the planned eight-station deployment combined with data from the existing INL permanent seismic network. The result will be a basic 1D seismic-velocity (including shear wave structure) model to a depth of a few kilometers; this model will be useful for improved event location and for comparison with the active seismic survey results. Previous applications of this method at other geothermal sites (i.e., Brady's geothermal field and Newberry Geothermal Energy) have proved successful (e.g., Matzel et al., 2014).

6.1.5 Magnetotellurics

An MT survey will characterize the electrical resistivity structure of the project area. It will be a remote-referenced tensor survey that includes the vertical magnetic field. One goal of the survey is to delineate properties of major aquifer units to be confirmed by independent information, such as drilling or seismic surveys. A second goal is to test for a local heat source indicated by a low-resistivity upwelling from the deeper crust, as is associated with extensional geothermal systems elsewhere (Wannamaker et al., 2011). A third goal is to derive background resistivity structure as a constraint for subsequent possible MT monitoring measurements that could be used to test for temporal changes in resistivity structure following well stimulation.

Inversion of the monitoring data will yield volumes and locations of rock subject to permeability changes, including anisotropic property changes, due to the state of fluid interconnection. One hundred tensor stations will be acquired with station spacing on the order 2 km (6,600 ft) toward the domain peripheries and 1 km (0.6 mi) toward the FORGE Operations Area. This is appropriate sampling for a well with experimental activity in the 1.5- to 2-km (4,900- to 6,600-ft) depth range and to achieve a depth of investigation of at least 10 km (32,800 ft). The MT responses will be inverted with new, uniquely powerful 3D inversion software described by Kordy et al. (2016a; 2016b). This software is based on the deformable finite element method and uses all direct solvers. This algorithm can incorporate an arbitrary a-priori inversion structure, making the algorithm suitable not only for establishing existing background structure but also for conservative estimation of subsurface structural changes during hydraulic stimulation by constraining minimal departures from that background.

6.1.6 Active Seismic Survey

An active seismic survey will be used to define the depth and attitude of the geothermal reservoir targets beneath the FORGE site. Our seismic characterization plan is based on previous INL seismic surveys and the Stanford Surprise Valley seismic survey (Egger et al., 2010). The seismic survey will use the University of Texas T-Rex vibroseis seismic source, which can image to more than 3-km (1.9-mi) depth. We will also conduct two refraction profiles using explosive sources by contracting with the National Seismic Source Facility at the University of Texas, El Paso. The explosive source data will provide constraint geologic structure below 3-km (9,800-ft) depth (similar to Pankratz and Ackermann, 1982).

Lines will consist of two 20-km (12.4-mi) oblique seismic profiles that extend from the range front and across the site of the proposed FORGE pilot well—one northwest-southeast profile along, or parallel to, U.S. Highway 20 and another north-south-oriented profile that crosses U.S. Highway 20 near the drill site. These vibroseis seismic lines will image south-dipping Paleozoic strata to determine whether they are faulted or folded beneath the SRP. These lines should also allow us to image the rhyolite system as it thickens to the south and any other continuous-velocity boundaries at greater depths. Tests in the field will be needed to assess the reflection imaging capabilities at the INL Site. Our plan will provide a detailed deep-velocity model for the construction of synthetic seismograms and data interpretation.

In summary, our seismic plan will:

1. Produce a detailed refraction tomogram for the upper 1 km (0.6 mi) using a vibroseis seismic source
2. Produce a reflection image for the upper 3+ km (1.9+ mi) using a vibroseis seismic source
3. Image the seismic velocity structure greater than 5-km (3.1-mi) depth using large explosives to tie with existing crustal-scale refraction data.

6.1.7 Slim Hole Coring

We will drill a new intermediate-depth slim hole (~700 m [2,300 ft]) in the GRRA near our selected site to test the geologic conceptual model, evaluate the local geothermal gradient, and examine the geochemical and isotopic characteristics of basalts and rhyolites. We will also perform hydraulic tests and collect core for detailed laboratory characterization and thin-section analysis. The laboratory tests of core will include those for:

- Density
- Mineral characterization
- Natural fracture properties and failure envelop
- Stress-dependent permeability and injection experiments
- Porosity
- Permeability
- Deformation and failure properties
- Brittleness
- Static and dynamic measurements
- Fluid inclusion analysis
- Bulk rock strength
- Thermal expansion coefficient
- Thermal conductivity
- Stoneley-wave reflections and attenuation
- Crossed dipole acoustics
- Nuclear magnetic resonance spectra
- Spectral natural gamma.

Also, a number of other tests will be conducted on the core to help solidify the interpretation of the geologic model. These tests include magnetic declination; magnetic susceptibility; density; radiometric dating; Ar/Ar dating; major element, trace element, and phase chemistry; electron microprobe and laser ablation inductively coupled plasma mass spectrometry for phase chemistry; x-ray fluorescence for major elements; and inductively coupled plasma mass spectrometry for trace elements.

Using the core data, we will update our existing poroelastic model and ground truth for both the seismic and gravity data sets. Groundwater hydraulic testing will be used to update the local model of aquifer flow and transport. Upon completion of the corehole, it will be instrumented as a deep monitoring well/piezometer and potentially a seismic monitoring station.

6.1.8 Reenter INEL-1

The 3.15-km (10,365)-deep INEL-1 geothermal test borehole remains open other than a bridge plug at a depth of approximately 460 m (1,509 ft). Collecting representative water samples and a suite of modern borehole geophysical logs from the deep geothermal reservoir is critical for successfully designing new wells for EGS. Pressure-integrity tests will be performed in selected intervals in INEL-1 to estimate the formation fracture gradient and to measure the stress-state of the system. It is important to know the pressure integrity of down-hole formations when planning and drilling the pilot well. Water chemistry analyses, gas analysis, fracture density, and other rock properties will be collected from this effort. After INEL-1 is reentered and the bridge plug is removed, a full suite of geophysical well logs will be collected. During water sample collection, the hydraulic properties of the formation will also be measured.

6.2 Phase 2C Characterization Activities

Phase 2C characterization activities are designed to collect the last data required to finalize the FORGE design. The focus of Phase 2C will be drilling a deep geothermal pilot well and a water-supply well. Also, passive seismic monitoring will continue throughout Phase 2C. During Phase 2C, it may be necessary to collect additional gravity data. For instance, some additional high-resolution gravity data may be collected on an as-needed basis. Also, the rock core collected from the geothermal well will be analyzed using the laboratory core techniques described in the previous section.

6.2.1 Water-Supply Well

A water-supply well is needed onsite for drilling of the deep geothermal test well, for onsite water needs, and for long-term EGS operations. Additionally, the water supply will be sufficient for fire-suppression requirements. We anticipate that this well will be approximately 200 m (650 ft) deep and drilled using an air-rotary drilling method. The well will be sited such that the slim hole drilled in Phase 2B can be used as an observation well for a pumping test of the water-supply well. Aquifer parameters, including transmissivity and storativity, will be collected during the test and used in the local groundwater flow model.

6.2.2 Pilot Well

In Phase 2C, we plan to initially drill a vertical pilot well to a depth between 2,500 and 4,000 m (8,200 and 13,100 ft) depending on the final measured geothermal gradient from the slim hole drilled in Phase 2B. This pilot well will serve two purposes. The first is to allow for detailed characterization of the entire vertical section at the FORGE site. Drilling a pilot well will allow for deep characterization of in situ fracture sets and determination of the in situ stress conditions, as well as collection of rock core. In Phase 2C, we plan to initially drill a vertical pilot well to a depth between 2,500 and 4,000 m (8,200 and 13,100 ft) depending on the final measured geothermal gradient from the slim hole drilled in Phase 2B. The second purpose is a cost-saving measure; we plan to sidetrack out of the pilot well at the initiation of Phase 3 using the Baker Hughes AutoTrak eXpress system. The AutoTrak eXpress system has continuous-string rotation while eliminating sliding and orienting for extended lateral legs.

The well is designed to allow repeated reentry and testing at high pressures. The design also includes as many as two lateral legs that can potentially be sidetracked out of the well. The preliminary design is as follows:

- Drill a 66-cm (26-in.) vertical hole to more than 244 m (800 ft), and run 51-cm (20-in.) casing that is cemented to the surface and equipped with a single gate and annular preventer. Set the casing through fluid loss zones.
- Drill a 44.45-cm (17½-in.) vertical hole to 1,500 m (5,000 ft) +/-; log the open hole; and run 34.6-cm (13 5/8-in.), 12.2-kg/m (88.2 pounds per foot), N-80, premium-connection casing that is cemented to the surface. Install a 34.6-cm (13 5/8-in.) 5M casing head and a 34.6-cm (13 5/8-in.) full blowout-prevention-equipment stack with a rotating head. Perform multiple mini-frac tests below this shoe in the 31.1-cm (12¼-in.) hole or with packers.
- Drill a 31.1-cm (12¼-in.) vertical hole to total depth; core intervals as necessary depending on logging-while-drilling (LWD)/ measurement-while-drilling data; run a complete suite of logs, including an imaging log; and run 24.4-cm (9 5/8-in.), premium-connection liner hung 61 m (200 ft) inside of a 34.6-cm (13-3/8-in.) shoe with liner top packer set as a backup seal after cementing the liner.

6.2.3 Well Logging Suite

A suite of wireline petrophysical and wellbore image logs is planned. Appendix H lists the well logs to be collected in the pilot well during Phase 2C. The purpose of acquiring and analyzing an extensive well log suite for the FORGE site is three-fold. First, the data will be used to improve structural models based on interpretation of surface geophysical surveys by obtaining an accurate profile of physical properties, such as density, velocity, and electrical conductivity as a function of depth. Second, the log data will be used to refine the geomechanical model, which includes the stress field, natural fracturing, and mechanical properties as a function of depth. Using this model, the orientations and conductivities of the most conductive fractures can be determined for selection of the optimal landing point and well plan for EGS development. Third, the value of each log will be assessed for delivery of the results to enable selection of the optimal log suite for future wells.

6.2.4 Rock Physics Analysis

We will perform rock physics analyses on well logs from the pilot well for the purpose of lithology identification and correlation with seismic and electromagnetic data. The rock physics analysis will use the rock and fluid properties measured at the well (such as porosity, mineral volumes, and saturations) and elastic properties (density, elastic wave velocities or impedances) and extrapolate this information to a larger volume based on seismic data (Grana et al., 2016; Appendix B). Our goal is to build a 3D model of rock and fluid properties adjacent to the well bore of the pilot well. However, farther away from the well, we can only measure elastic properties (and potentially resistivity and gravity). In order to build this model, given the seismic data, we will (1) perform a seismic inversion to estimate elastic properties; (2) estimate a rock physics relation at the well to link elastic to rock properties; and (3) apply the calibrated rock physics model and estimate the 3D model or rock properties.

Key logs will include wellbore images that will be needed to detect structurally important natural fractures and stress-induced wellbore breakouts and tensile wall fractures, as well as stratigraphic features. We plan to use an advanced wireline and LWD imaging program. The newly developed GeoThermal Imager, an ultrasonic phased-array imaging tool rated to 300°C (527°F), can be deployed under equilibrium temperatures (Figure 31). While drilling, the LWD StarTrak tool (Figure 32) will provide real-time, high-resolution electrical images to extract critical information regarding in situ stress orientation and stress magnitude and to characterize natural fractures.

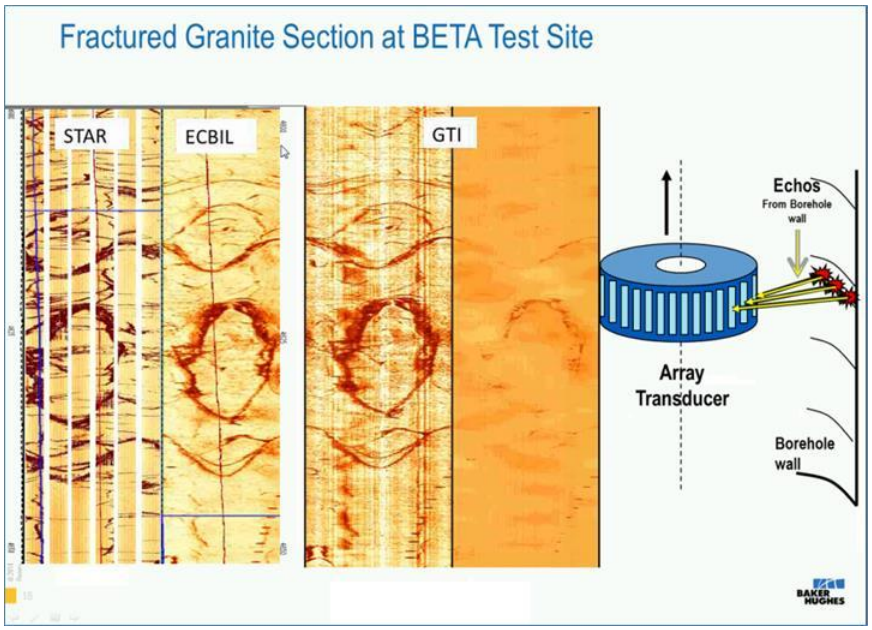

Figure 31. Comparison of electrical image (Panel 1), ultrasonic amplitude image (Panel 2) with ultrasonic, and travel time images recorded with the newly developed GeoThermal Imager in granite (Panels 3 and 4).

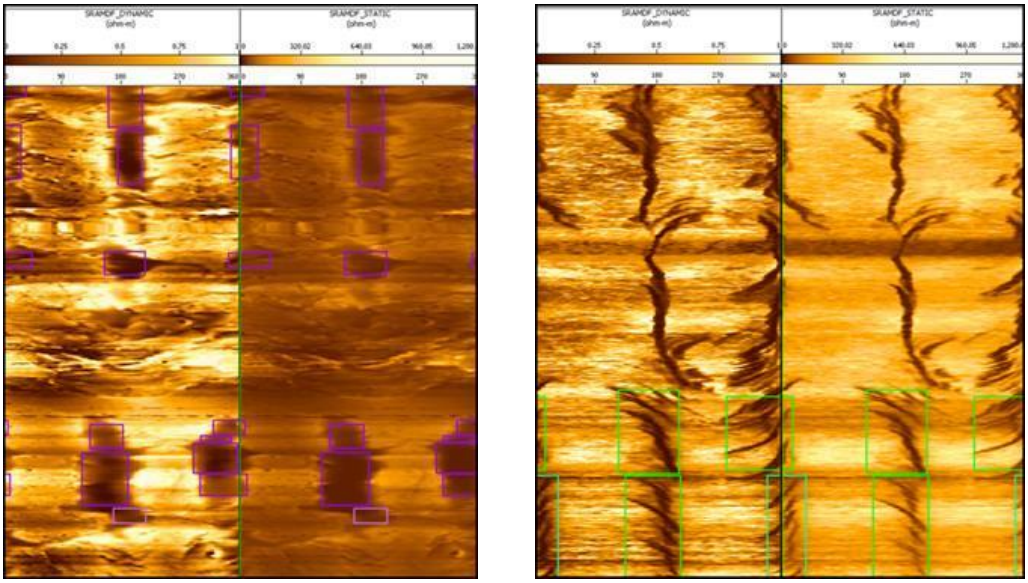

Figure 32. Example of the image data recorded with the LWD StarTrak tool capable of real-time recording of very high-resolution images with full azimuthal coverage during drilling. Wellbore breakouts and natural fractures are seen in the left set of images, and induced tensile fractures and wellbore damage (petal-centerline fractures) are discriminated in the set of images on the right.

7. SUMMARY AND CONCLUSION

The data we have presented show that the GRRA is a prime candidate for EGS in the ESRP. Using a combination of geophysical results, geologic investigations, and observations from deep boreholes, we defined two bounding end-member geologic models. The primary difference between the models is the geometry of the contact separating the ESRP rhyolites from the possible underlying Paleozoics. One model is constructed from the inferred boundaries of four nested calderas within the 8- to 10-Ma Picabo volcanic field and assumes that these calderas are similar to the currently active Yellowstone volcanic system. In this model, the rhyolite/Paleozoic contact is formed by ring faults associated with caldera subsidence and the potential FORGE reservoir is composed of intra-caldera rhyolite flows and/or rhyodacites similar to those observed in deep Borehole INEL-1. The second model is derived from the crustal flexure model of McQuarrie and Rodgers (1998) and depicts the rhyolite/Paleozoic basement contact beneath the GRRA as a surface that dips ~30 degrees toward the ESRP. The nested calderas are shifted several kilometers to the south, while the rocks beneath the GRRA primarily consist of extra-caldera rhyolite flows and ignimbrite sheets. Permeability measurements of all the potential reservoir lithologies range from 6.7×10^{-20} to 1.8×10^{-17} m^2 (0.068 to 2 μD), which is less than the maximum permeability allowed for FORGE.

One uncertainty in our geologic model is the dip of the rhyolite/Paleozoic basement boundary beneath the GRRA. To minimize the risks of penetrating this boundary prior to encountering temperatures in excess of 175°C (347°F), we chose a FORGE site that is far enough away from the range front to maximize the likelihood that rhyolite lithologies are present to more than 4 km (13,100 ft) below the surface.

We bracketed the likely depth to the 175°C (347°F) isotherm within the range of conductive temperature gradients observed in five deep boreholes near the GRRA. The data indicate that the 175°C isotherm lies between 2.4 and 3.8 km (7,800 and 12,500 ft) beneath the surface, yielding potential reservoir volumes of 0.6 to 2.1 km^3 (0.14 to 0.49 mi^3).

Our preliminary geomechanical model, based primarily on rock strength measurements and well logs from deep Borehole INEL-1, suggests in situ stress conditions are amenable to hydraulic fracturing of the reservoir. Additionally, we presented a workflow for extending this model to three dimensions when more data become available during Phase 2.

Finally, we presented a Phase 2 characterization plan. This plan calls for geophysical, hydrological, and geochemical site characterization. Additionally, a deep pilot well will be drilled and characterized using state-of-the-art down-hole logging tools.

We have shown that our site meets the requirements for FORGE. We bounded the uncertainties in reservoir depth, volume, and temperature by developing two end-member geologic structural scenarios utilizing 3D geologic modeling software. Overlaying two thermal gradients on the geologic models generated four reservoir/thermal scenarios. All scenarios exceed FORGE site selection requirements.

REFERENCES

Anders, M.H., Geissman, J.W., Piety, L.A., and Sullivan, J.T., 1989, Parabolic distribution of circumeastern Snake River Plain seismicity and latest Quaternary faulting: Migratory pattern and association with the Yellowstone hotspot: Journal of Geophysical Research, v. 94, no. B2, p. 1589–1621, doi: 10.1029/JB094iB02p01589.

Anders, M.H., Rodgers, D.W., Hemming, S.R., Saltzman, J., DiVenere, V.J., Hagstrum, J.T., Embree, G.F., and Walter, R.C., 2014, A fixed sublithospheric source for the late Neogene track of the Yellowstone hotspot: Implications of the Heise and Picabo volcanic fields: Journal of Geophysical Research: Solid Earth, v. 119, no. 4, p. 2871–2906, doi: 10.1002/2013JB010483.

Bakshi, R., Halvaei, M. E., and Ghassemi, A., 2016, Geomechanical characterization of core from the proposed FORGE laboratory on the Eastern Snake River Plain, Idaho: *in* Proceedings, 41st Workshop on Geothermal Reservoir Engineering Stanford University, Stanford, California, SGP-TR-209.

Barton, C. A., Moos, D., Hartley, D., Baxter, S., Foulquier, L., Holl, H., and Hogarth, R., 2013, Geomechanically coupled simulation of flow in fractured reservoirs: *in* Proceedings, 38th Workshop on Geothermal Reservoir Engineering Stanford University, Stanford, California, SGP-TR-198.

Blackwell, D. D., 1990, Temperatures and heat flow in INEL-GT1 and WO-2 boreholes, Snake River Plain, Idaho, Department of Energy, doi: 10.2172/1017885.

Blackwell, D., Richards, M., Frone, Z., Batir, J., Ruzo, A., Dingwall, R., and Williams, M., 2011, Temperature at depth maps for the conterminous US and geothermal resource estimates: Geothermal Resources Council Transactions, v. 35, p. 1545–1550, GRC Record 1029452.

Bowers, G.L., 1995, Pore Pressure Estimation from Velocity Data: Accounting for Overpressure Mechanisms Besides Undercompaction: SPE Drilling & Completion.

Branney, M., and Acocella, V., 2015, Calderas, *in* Sigurdsson, J., Houghton, B., McNutt, S.R., and Stix, J. eds., Encyclopedia of volcanoes, Elsevier/Academic Press, New York.

Branney, M.J., Bonnichsen, B., Andrews, G.D.M., Ellis, B., Barry, T.L., and McCurry, M., 2008, "Snake River (SR)-type" volcanism at the Yellowstone hotspot track: distinctive products from unusual, high-temperature silicic super-eruptions: Bulletin of Volcanology, v. 70, p. 293–314, doi: 10.1007/s00445-007-0140-7.

Byerlee, J.D., 1978, Friction of Rocks: Pure and Applied Geophysics, v. 116, p. 615-626, doi: 10.1007/BF00876528.

Christiansen, R.L., 2001, The Quaternary and Pliocene Yellowstone Plateau Volcanic Field of Wyoming, Idaho, and Montana: U.S. Geological Survey Professional Paper 729-G.

Cole, J., Milner, D., and Spinks, K., 2005, Calderas and caldera structures: a review: Earth-Science Reviews, v. 69, no. 1-2, p. 1–26, doi: 10.1016/j.earscirev.2004.06.004.

DeNosaquo, K.R., Smith, R.B., and Lowry, A.R., 2009, Density and lithospheric strength models of the Yellowstone-Snake River Plain volcanic system from gravity and heat flow data: Journal of Volcanology and Geothermal Research, v. 188, no. 1-3, p. 108–127, doi: 10.1016/j.jvolgeores.2009.08.006.

de Silva, S.L., and Gregg, P.M., 2014, Thermomechanical feedbacks in magmatic systems: Implications for growth, longevity, and evolution of large caldera-forming magma reservoirs and their supereruptions: Journal of Volcanology and Geothermal Research, v. 282, p. 77–91, doi: 10.1016/j.jvolgeores.2014.06.001.

Dobson, P.F., Kennedy, M., Conrad, M.E., McLing, T., Mattson, E., Wood, T., Cannon, C., Spackman, R., van Soest, M., and Robertson, M, 2015, He Isotopic evidence for undiscovered geothermal systems in the Snake River Plain: *in* Proceedings, 40th Workshop on Geothermal Reservoir Engineering Stanford University, Standford California, SGP-TR-204.

Doherty, D., McBroome, L., and Kuntz, M., 1979, Preliminary geological interpretation and lithologic log of the exploratory geothermal test well (INEL-1): U. S. Geological Survey Open-File Report, v. 79-1248, p. 10.

Drew, D.L., Bindeman, I.N., Watts, K.E., Schmitt, A.K., Fu, B., and McCurry, M., 2013, Crustal-scale recycling in caldera complexes and rift zones along the Yellowstone hotspot track: O and Hf isotopic evidence in diverse zircons from voluminous rhyolites of the Picabo volcanic field, Idaho: Earth and Planetary Science Letters, v. 381, p. 63–77, doi: 10.1016/j.epsl.2013.08.007.

Egger, A.E., Glen, J.M.G., and Ponce, D.A., 2010, The northwestern margin of the Basin and Range province Part 2: Structural setting of a developing basin from seismic and potential field data: Tectonophysics, v. 488, p. 150-161, doi:10.1016/j.tecto.2009.05.029.

Furlong, K., 1979, An analytic stress model applied to the Snake River Plain (northern Basin and Range Province, U. S. A.): Tectonophysics, v. 58, p. 11–15.

Grana, D., Verma, S., and Podgorney, R., 2016, Rock Physics Modeling for the Potential FORGE Site on the Eastern Snake River Plain, Idaho; *in* Proceedings, Workshop on Geothermal Reservoir Engineering Stanford University, Stanford, California, SGP-TR-209.

Holland, M., Brudy, M., Van Der Zee, W., Perumalla, W., and Finkbeiner, T., 2010, Value of 3D Geomechanical Modeling in Field Development – A New Approach Using Geostatistics: SPE/DGS Saudi Arabia Section Technical Symposium and Exhibition, April 4–7, Al-Khobar, Saudi Arabia.

Jaeger, J.C. and Cook, N.G.W., 1979, Fundamentals of Rock Mechanics, 3rd Edition, London, Chapman and Hall.

Kelbert, A., Egbert, G.D., and deGroot-Hedlin, C., 2012, Crust and upper mantle electrical conductivity beneath the Yellowstone Hotspot Track: Geology, v. 40, no. 5, p. 447–450, doi: 10.1130/G32655.1.

Kordy, M., Wannamaker, P., Maris, V., Cherkaev, E., and Hill, G., 2016a, 3-D magnetotelluric inversion including topography using deformed hexahedral edge finite elements and direct solvers parallelized on SMP computers–Part I: forward problem and parameter Jacobians: Geophysical Journal International, v. 204, no. 1, p. 74–93.

Kordy, M., Wannamaker, P., Maris, V., Cherkaev, E., and Hill, G., 2016b, 3-D magnetotelluric inversion including topography using deformed hexahedral edge finite elements and direct solvers parallelized on SMP computers– Part II: direct data-space inverse solution: Geophysical Journal International, v. 204, no. 1, p. 94–110.

Kuntz, M.A., Spiker, E.C., Rubin, M., Champion, D.E., and Lefebvre, R.H., 1986, Radiocarbon studies of latest Pleistocene and Holocene lava flows of the Snake River Plain, Idaho: Data, lessons, interpretations: Quaternary Research, v. 25, no. 2, p. 163–176, doi: 10.1016/0033-5894(86)90054-2.

Leeman, W.P., Annen, C., and Dufek, J., 2008, Snake River Plain - Yellowstone silicic volcanism: implications for magma genesis and magma fluxes: Geological Society, London, Special Publications, v. 304, no. 1, p. 235–259, doi: 10.1144/SP304.12.

Leeman, W.P., Schutt, D.L., and Hughes, S.S., 2009, Thermal structure beneath the Snake River Plain: Implications for the Yellowstone hotspot: Journal of Volcanology and Geothermal Research, v. 188, no. 1–3, p. 57–67, doi: 10.1016/j.jvolgeores.2009.01.034.

Lipman, P.W., 1997, Subsidence of ash-flow calderas: relation to caldera size and magma-chamber geometry: Bulletin of Volcanology, v. 59, no. 3, p. 198–218, doi: 10.1007/s004450050186.

Mabey, D.R., 1978, Gravity and aeromagnetic anomalies in the Rexburg area of Eastern Idaho: U.S. Geological Survey Open-File Report, v. 78-382, 19 p.

Mann, L.J., 1986, Hydraulic properties of rock units and chemical quality of water for INEL-1: a 10,365-foot deep test hole drilled at the Idaho National Engineering laboratory, Idaho: Water Resources Investigations Report 86-4020, U.S. Geological Survey, 27 p.

Matzel, E., Templeton, D., Petersson, A., and Goebel, M., 2014, Imaging the Newberry EGS site using seismic interferometry: *in* Proceedings, Thirty-Ninth Workshop on Geothermal Reservoir Engineering Stanford University, Stanford, California, SGP-TR-202.

McCurry, M., McLing, T., Smith, R.P., Hackett, W.R., Goldsby, R., Lochridge, W., Podgornery, R., Wood, T., Pearson, E., Welhan, J., Plummer, M., 2016, Geologic setting of the Idaho National Laboratory Geothermal Resource Research Area: *in* Proceedings, 41st Workshop on Geothermal Reservoir Engineering Stanford University, Stanford, California, SGP-TR-209.

McCurry, M., and Rodgers, D.W., 2009, Mass transfer along the Yellowstone hotspot track I: Petrologic constraints on the volume of mantle-derived magma: Journal of Volcanology and Geothermal Research, v. 188, no. 1-3, p. 86–98, doi: 10.1016/j.jvolgeores.2009.04.001.

McCurry, M., and Welhan, J., 2012, Do Magmatic-Related Geothermal Energy Resources Exist in Southeast Idaho?: GRC Transactions, v. 36, p. 699–707.

McLing, T.L., Smith, R.P., Smith, R.W., Blackwell, D.D., Roback, R.C., and Sondrup, A.J., 2016, Wellbore and groundwater temperature distribution Eastern Snake River Plain, Idaho; implications for groundwater flow and geothermal potential: Journal of Volcanology and Geothermal Research, in press.

McQuarrie, N., and Rodgers, D.W., 1998, Subsidence of a volcanic basin by flexure and lower crustal flow: The eastern Snake River Plain, Idaho: Tectonics, v. 17, no. 2, p. 203, doi: 10.1029/97TC03762.

Metcalfe, Elisabet, 2015, Road Tripping through the Geothermal Frontier, http://energy.gov/eere/articles/road-tripping-through-geothermal-frontier, U.S. Department of Energy, November 18, 2015.Stanford University, Stanford, California, February 24-26, 2014, SGP-TR-202.

Moos, D., and C. Barton, 1990, In-Situ Stress and Natural Fracturing at the INEL Site, Idaho, DOE Report EGG-NPR-10631.

Moos, D., and Zoback, M.D., 1990, Utilization of observations of well bore failure to constrain the orientation and magnitude of crustal stresses: Application to continental, Deep Sea Drilling Project, and Ocean Drilling Program boreholes: Journal of Geophysical Research, v. 95, 9305-9325, doi: 10.1029/JB095iB06p09305.

Morgan, L.A., and McIntosh, W.C., 2005, Timing and development of the Heise volcanic field, Snake River Plain, Idaho, western USA: Geological Society of America Bulletin, v. 117, no. 3, p. 288, doi: 10.1130/B25519.1.

Pankratz, L.W., and Ackermann, H.D., 1982, Structure along the northwest edge of the Snake River Plain interpreted from seismic refraction: Journal of Geophysical Research, v. 87, no. B4, p. 2676, doi: 10.1029/JB087iB04p02676.

Parsons, T., Thompson, G.A., and Smith, R.P., 1998, More than one way to stretch: a tectonic model for extension along the plume track of the Yellowstone hotspot and adjacent Basin and Range Province: Tectonics, v. 17, no. 2, p. 221, doi: 10.1029/98TC00463.

Peng, X., and Humphreys, E.D., 1998, Crustal velocity structure across the eastern Snake River Plain and the Yellowstone swell: Journal of Geophyscial Research, v. 103, p. 7171–7186.

Perkins, M.E., and Nash, B.P., 2002, Explosive silicic volcanism of the Yellowstone hotspot: the ash fall tuff record: Geological Society of America Bulletin, v. 114, no. 3, p. 367–381.

Pierce, K.L., and L.A. Morgan, 1992, The track of the Yellowstone hot spot: Volcanism, faulting, and uplift: Geological Society of America Memoir 179, p. 1–54.

Pierce, K.L., and Morgan, L.A., 2009, Is the track of the Yellowstone hotspot driven by a deep mantle plume? — Review of volcanism, faulting, and uplift in light of new data: Journal of Volcanology and Geothermal Research, v. 188, no. 1-3, p. 1–25, doi: 10.1016/j.jvolgeores.2009.07.009.

Podgorney, R., Snyder, N., Mink, L. R., and McLing, T., 2016, A Snake River Plain Field Laboratory for Enhanced Geothermal Systems: An Overview of the Snake River Geothermal Consortium's Proposed FORGE Site, *in* Proceedings, 41st Workshop on Geothermal Reservoir Engineering Stanford University, Stanford, California, February 22–24, SGP-TR-209.

Potter, K.E., 2014, The Kimama Core: A 6.4 Ma record of volcanism, sedimentation, and magma petrogenesis on the axial volcanic high Snake River Plain, ID [Ph.D. dissertation]: Utah State University, 174 p.

Prestwich, S., and Bowman, J.A., 1980, Completion and Testing Report: INEL Geothermal Exploratory Well One (INEL-1), Department of Energy, Idaho Operations Office, IDO-10096, 53 p.

Rodgers, D.W., Ore, H.T., and Bobo, R.T., 2002, Extension and subsidence of the eastern Snake River Plain, Idaho: Tectonic and Magmatic Evolution of the Snake River Plain Volcanic Province, p. 121–155.

Schmandt, B., Dueker, K., Humphreys, E., and Hansen, S., 2012, Hot mantle upwelling across the 660 beneath Yellowstone: Earth and Planetary Science Letters, v. 331-332, p. 224–236, doi: 10.1016/j.epsl.2012.03.025.

Shervais, J.W., Schmitt, D.R., Nielson, D., Evans, J.P., Christiansen, E.H., Morgan, L., Pat Shanks, W.C., Prokopenko, A.A., Lachmar, T., Liberty, L.M., Blackwell, D.D., Glen, J.M., Champion, D., Potter, K.E., et al., 2013, First results from HOTSPOT: The Snake River plain scientific drilling project, Idaho, U.S.A.: Scientific Drilling, no. 15, p. 36–45, doi: 10.2204/iodp.sd.15.06.2013.

Sandwell, D., Mellors, R., Tog, X., Wei, D., Wessel, P., 2011, Open radar interferometry software for mapping surface deformation: Eos Transactions, AGU 92 (28), 234 p.

Smith, R.B., Jordan, M., Steinberger, B., Puskas, C.M., Farrell, J., Waite, G.P., Husen, S., Chang, W.-L., and O'Connell, R., 2009, Geodynamics of the Yellowstone hotspot and mantle plume: Seismic and GPS imaging, kinematics, and mantle flow: Journal of Volcanology and Geothermal Research, v. 188, no. 1-3, p. 26–56, doi: 10.1016/j.jvolgeores.2009.08.020.

Smith, R.P., Jackson, S.M., and Hackett, W.R., 1996, Paleoseismology and seismic hazards evaluation in extensional volcanic terrains: Journal of Geophysical Research, v. 101, no. B3, p. 6277–6292.

Sparlin, M.A., and Braile, L.W., 1982, Crustal structure of the Eastern Snake River Plain determined from ray trace modeling of seismic refraction data: Journal of Geophyscial Research, v. 87, no. B4, p. 2619–2633.

Templeton, D., Mellors, R., Payne, S., Irving, J., Ulrich, J., and Podgorney, R., 2016, Preliminary Induced Seismicity Plan: Snake River Plain, Idaho, Snake River Geothermal Consortium, INL/LTD-16-38124.

Wagner, L.S., Fouch, M.J., James, D.E., and Hanson-Hedgecock, S., 2012, Crust and upper mantle structure beneath the Pacific Northwest from joint inversions of ambient noise and earthquake data: Geochemistry, Geophysics, Geosystems, v. 13, no. 12, p. n/a–n/a, doi: 10.1029/2012GC004353.

Wannamaker, P.E., Maris, V., Hasterok, D., and Doerner, W., 2011, Crustal Scale Resistivity Structure, Magmatic-Hydrothermal Connections, and Thermal Regionalization of the Great Basin: Geothermal Resources Council Transactions, 35, p. 1787–1790.

Ward, C.D., Coghill, K., and Broussard, M.D., 1994, The Application of Petrophysical Data to Improved Pore and Fracture Pressure Determination in North Sea Graben HPHT Wells, SPE Annual Technical Conference and Exhibition, Society of Petroleum Engineers, September 25–28, New Orleans, Louisiana, SPE-28297-MS.

Welhan, J.A., 2016, Thermal and Geochemical Anomalies in the Eastern Snake River Plain Aquifer: Contributions to a Conceptual Model of the Proposed FORGE Test Site, *in* Proceedings, Workshop on Geothermal Reservoir Engineering Stanford University, Stanford, California, SGP-TR-209.

Zoback, M. D. (2007), Reservoir Geomechanics, Cambridge University Press.

Zoback, M. D. and Healy, J. H., 1992, In Situ Stress Measurements to 3.5 km Depth in the Cajon Pass Scientific Research Borehole: Implications for the Mechanics of Crustal Faulting: Journal of Geophysical Research, v. 97 doi: 10.1029/91JB02175.

Zohdy, A.A.R., and Stanley, W.D., 1973, Preliminary interpretation of electrical sounding curves obtained across the Snake River Plain from Blackfoot to Arco, Idaho: U. S. Geological Survey Open-File Report, v. 73-370.

Appendix A

Geologic Setting of the Idaho National Laboratory Geothermal Resource Research Area

PROCEEDINGS, 41st Workshop on Geothermal Reservoir Engineering
Stanford University, Stanford, California, February 22-24, 2016
SGP-TR-209

Geologic Setting of the Idaho National Laboratory Geothermal Resource Research Area

Michael McCurry[1], Travis McLing[2], Richard P. Smith[3], William R. Hackett[4], Ryan Goldsby[1], William Lochridge[1], Robert Podgorney[2], Thomas Wood[5], David Pearson[1], John Welhan[6], Mitch Plummer[2]

[1]Department of Geosciences, Idaho State University, Pocatello, ID 83209

[2]Idaho National Engineering Laboratory, Idaho Falls, ID 83415

[3]Smith Geologic and Photographic Services, LLC, 13786 Schoger Road, Nathrop, CO 81236

[4]WRH Associates, Inc., 2007 Cherokee Circle, Ogden, UT 84403

[5]University of Idaho, Center for Advanced Energy Studies, Idaho Falls, ID 83402

[6]Idaho Geological Survey, University of Idaho, Moscow, ID 83844

e-mail: Michael McCurry <mccumich@isu.edu>

Keywords: Snake River Plain, geologic conceptual model, subsurface geology, rhyolite, caldera, EGS

ABSTRACT

The Idaho National Laboratory (INL) has designated ~100 km^2 of the Eastern Snake River Plain (ESRP), along the track of the Yellowstone Hot Spot, as a Geothermal Resource Research Area (GRRA). The GRRA is a designated area of the INL Site to support research and development for all aspects of geothermal energy. The GRRA is the focus of studies under the Phase I award to the Snake River Geothermal Consortium (SRGC) from the DOE Frontier Observatory Research in Geothermal Energy (FORGE) program. The GRRA provides a robust field site for development of innovative and advanced geothermal technologies, approaches and methods.

The GRRA is located in a geological region that is dominated by the Yellowstone volcanic track, the Earth's largest and most active continental hot spot system. It is well known for high regional heat flow (110 mW/m^2) and voluminous late Miocene to Holocene magmatism and tectonism. The GRRA is generally underlain by several hundred meters of interbedded Pleistocene basalt lavas erupted from widely scattered vents on the ESRP and sediment derived from mountain ranges northwest of the plain. The basalts and sediments host part of the prolific ESRP aquifer. In the adjacent 3.2 km deep INEL-1 well, these rocks overlie thousands of meters of rhyolites erupted during the climax of hot spot related volcanic activity between ~10 and 4.5 Ma. The rhyolites are dominantly voluminous densely welded ignimbrites, lava flows and shallow intrusions that ponded within and intruded beneath and into coeval caldera systems. Permeability of the thick intracaldera deposits is extremely low due to a combination of very dense welding and rock alteration and mineralization driven by now-extinct intracaldera hydrothermal systems. The extremely low permeability and large mass of the hot deep rocks is ideally suited for EGS studies as heat recovery from this region will require advanced drilling, reservoir stimulation, and fluid injection to achieve necessary heat extraction.

1. INTRODUCTION

The Eastern Snake River Plain (ESRP) is one of the largest regions in North America of high heat flow (up to 110 mW/m^2) and robust volcanic and tectonic activity (e.g., Blackwell, 1989; Anders et al., 2014). Recent activity is dominated by Yellowstone-Snake River Plain hot spot system (e.g., Smith et al., 2009). Enormous overlapping and nested calderas were produced by voluminous rhyolitic volcanic eruptions between 10 and 4.6 Ma, producing potentially ideal host-rock materials for development of EGS technologies. However, post-caldera basaltic volcanism, and the development of a robust active aquifer system have muted obvious surficial evidence of the underlying caldera systems and high heat flow (e.g., Smith, 2004). Locations and characteristics of buried (cryptic) calderas are therefore inferred from robust regional geologic and geophysical surveys, and from deep borehole data.

This paper is a preliminary summary of the geologic setting and evolution of the Geothermal Resources Research Area (GRRA), emphasizing materials, structures and cryptic caldera context of the proposed EGS reservoir system. It summarizes and integrates previous work with the focus being to develop a geologically and geophysically constrained range of conceptual models of GRRA subsurface geologic architecture at geothermal-reservoir-relevant depths of 1.5 to 4 km.

2. REGIONAL GEOLOGIC SETTING

The GRRA site is located on the northern margin of the Yellowstone-Snake River Plain (YSRP) volcanic track, the worlds largest active continental hot spot system (e.g., Smith et al. 2009) (Fig. 1).

The crust in this region consists mainly of early Precambrian crystalline rocks (Foster et al., 2006) that are overlain by late Precambrian to Mesozoic age sedimentary rocks of the Cordilleran fold and thrust belt (Dickinson, 2004; DeCelles and Coogan, 2006; Yonkee et al., 2014). Regional magmatic activity produced the late Cretaceous Idaho Batholith and Eocene Challis volcanic province (e.g., Gaschnig et al., 2011) and Oligocene intrusions of the Albion Mountains region (Konstantinou et al., 2012, 2013a). But with the exception of distal sedimentary facies of the Challis system, none of these appear to have extended to the GRRA area (Fig. 2A). Strong extension

occurred in Eocene to early Oligocene exposing mid-crustal rocks in isolated metamorphic core complexes of the Pioneer and Albion-Raft River Mountains areas, northwest and southwest of GRRA (Strickland et al., 2011a,b). Coeval, less intense extension produced half graben basins over a wider region, including formation of the Arco Pass Basin located just north of the GRRA in the Arco Hills (e.g., Link and Janecke, 1999). Another, later phase of late Miocene extension and uplift occurred during proximal volcanism along the YSRP (Vogel et al., 2014; Konstantinou et al.. 2011, 2013b).

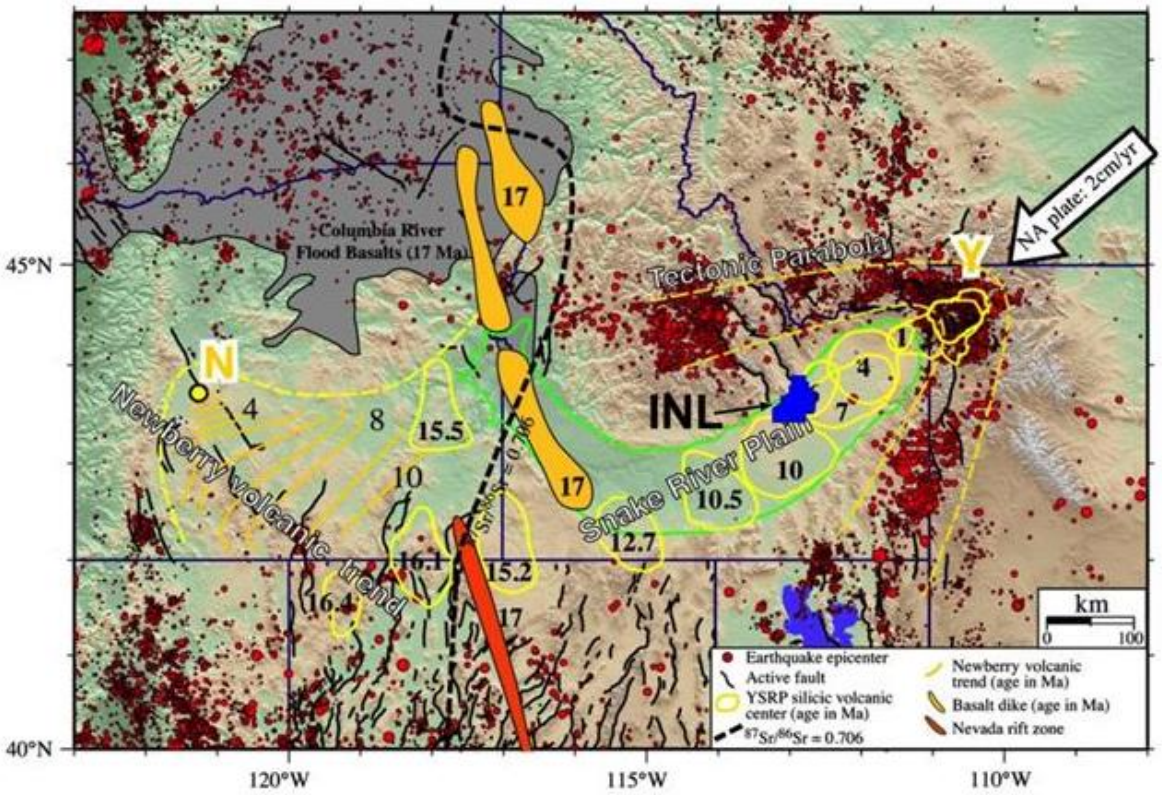

Figure 1: The location and regional geologic and tectonic setting of the proposed GRRA and FORGE Phase 1 study area (after Smith et al., 2009, their figure 2). The GRRA is located on the northwest margin of the INL (shown in dark blue). The map emphasizes major Neogene to Recent volcanic and tectonic features related to development and evolution of the Nevada-Columbia magmatic belt (Camp et al., 2015) and the Yellowstone-Snake River Plain hotspot system. Most lines and symbols are explained on the inset explanation. Ages of initiation of major silicic volcanism are indicated for rhyolite volcanic fields (yellow lines). The green line encompasses Quaternary to Pliocene basalt lavas that postdate local rhyolite volcanism.

Regional Basin-and-Range extension began ~17-15 Ma and is continuing to present, most actively in eastern and western regions of Basin and Range (e.g., Parsons, 1995), and around the margins of the ESRP - the YSRP "tectonic parabola" (e.g., Anders et al., 1989) (Fig. 1). Inception of Basin and Range extension coincided with massive 17-15 Ma outpouring of basalt lavas of the Columbia River Basalt (CRB) Large Igneous Province (LIP) (e.g., Camp et al., 2015) (Fig. 1). Numerous studies suggest that initiation of extension, coeval CRB volcanism, volcanism in southeastern Oregon, and southward across central Nevada are genetically linked to upward impingement of a mantle plume on the base of the North American lithosphere (e.g., Pierce et al., 2009).

Basaltic CRB volcanism is followed by two time-transgressive tracks of rhyolite-dominated volcanism. A weaker northwest trending track, the Oregon High Lava Plains track (Fig. 1, Newberry volcanic trend), and a much more robust track that extends to the northeast across southern Idaho and currently located beneath the Yellowstone, Wyoming region (referred to here as the YSRP track, for Yellowstone-Snake River Plain) (Fig. 1, 2A).

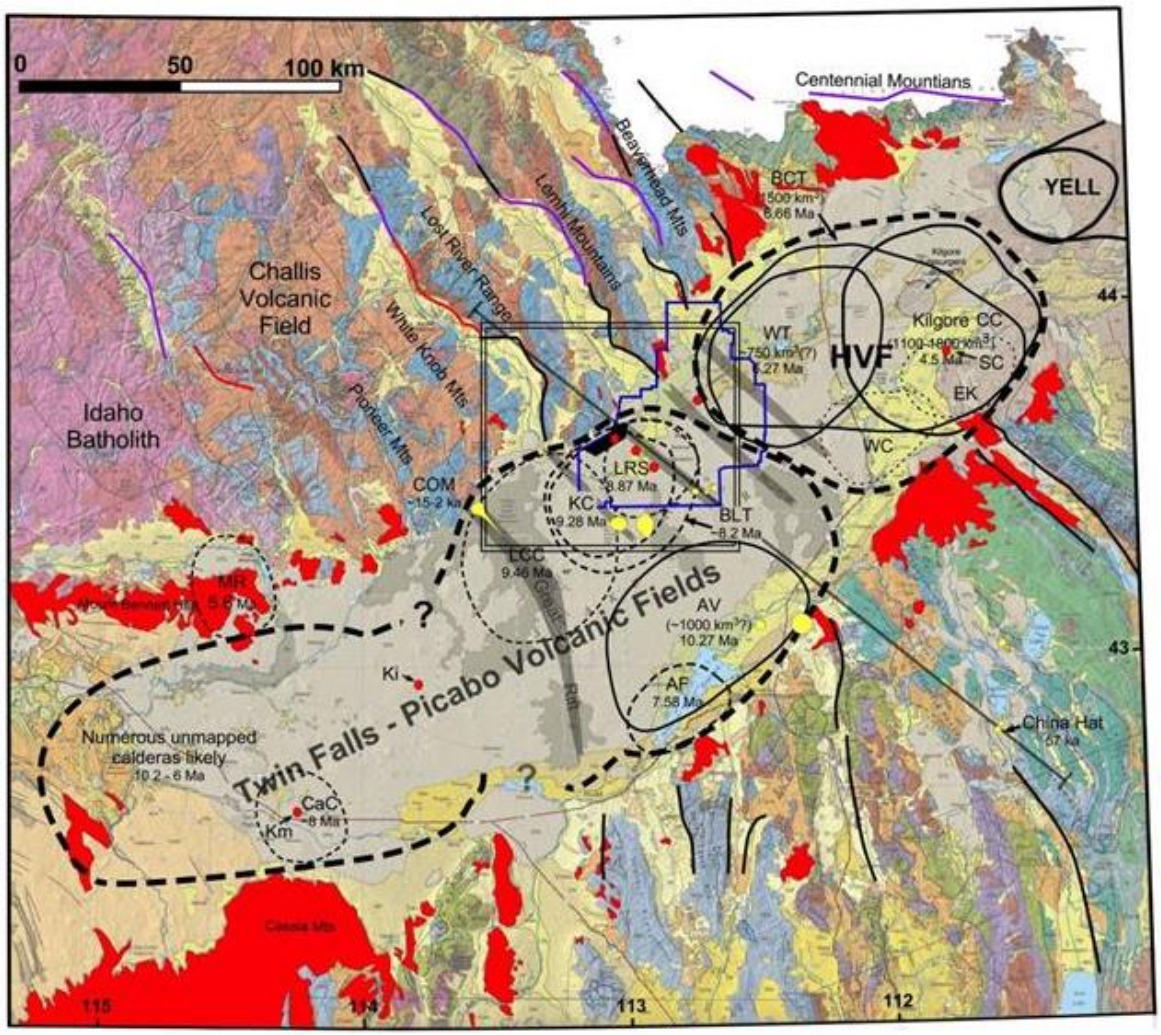

Figure 2. Geologic map of the Eastern Snake River Plain (ESRP) and its surroundings emphasizing salient volcanic and tectonic features. The INL is outlined in blue with a black inset showing the location of the GRRA. Double lines indicate the location of a blow-up geologic map (Figure 11). The geologic base map is from Lewis et al. (2012). Shades of green, blue and purple illustrate late Precambrian to Paleozoic sedimentary rocks exposed in Basin and Range horst blocks north and south of the plain. Faults having late Neogene to Recent activity are shown in bold lines (after Anders et al., 2014). Pale shades of grey on the Snake River Plain indicate Quaternary basalt lavas (Holocene in darker shade); pale yellow indicates Quaternary sediment. Yellow = Quaternary cryptodomes, lava domes and volcanic fields consisting of geochemically evolved mafic to rhyolitic composition (e.g., McCurry and Welhan, 2012). Bold red colors indicate exposures of rhyolites (mostly ignimbrites) exposed along the margins of the plain. Major rhyolite volcanic fields are illustrated with bold dashed lines; HVF = Heise volcanic field. Twin Falls and Picabo fields overlap in age and are therefore combined. Deep boreholes are shown as red dots (Km=Kimberly; Ki+Kimama; SC=Sugar City; after Shervais et al., 2013). Boreholes located within the boundaries of INL are distinguished in Figures 5 and 11A. Inferred caldera locations and ages are illustrated with solid (better defined location) and dashed (less well defined location) black lines. TF=Twin Falls, after Shervais et al., 2013; MR=Magic Reservoir, after Leeman, 1982b; AF=American Falls, LCC=Little Chokecherry Canyon, KC=Kyle Canyon, LRS=Lost River Sinks, are after Anders et al., 2014; AV=Arbon Valley (or Taber), after Kellogg et al., 1994; Kuntz et al., 1992; McCurry, 2009; WT=Walcott, BCT=Blacktail Creek, Kilgore, and CC=Conant Creek, are after Morgan and McIntosh, 2005, modified by Anders et al., 2014; WC=Wolverine Creek, Ek=Elkhorn Spring, are after Anders et al., 2014). 2B. A cross-section of the crust and upper mantle (from McCurry and Welhan, 2012; modified from Peng and Humphreys, 1998). The cross-section extends southeast from the southern end of the Lost River Range to China Hat. ESRP = Eastern Snake River Plain; BVF = Blackfoot Volcanic Field; PMs = late Precambrian to Paleozoic miogeoclinal sedimentary rocks.

The YSRP is defined on the basis of a northeast trending, time-transgressive pattern in the inception of voluminous rhyolite volcanism (e.g., Armstrong et al., 1975; Pierce and Morgan, 1992). It 'migrates' at an average rate and in a direction closely mirroring 'absolute'

motion of the North American lithosphere (e.g. Smith et al. 2009) (Fig. 1). Volcanic fields evolved in waxing-waning cycles lasting several m.y., and overlapped in time and space with strong subsidence (sagging) along the volcanic track, and robust extension via Basin and Range extension in regions peripheral to the track. Detailed study of structures along the northern margin of the plain (Fig. 3) indicate 5 to 6 km of ESRP directed subsidence, almost all of which is accommodated by flexure (e.g., McQuarrie and Rodgers, 1998; Rodgers et al., 2002). Geophysical studies indicate that the subsidence occurred in response to intrusions on mafic magmas from the mantle into the lower- and middle-crust (e.g., Brott et al., 1981; Braile et al., 1982).

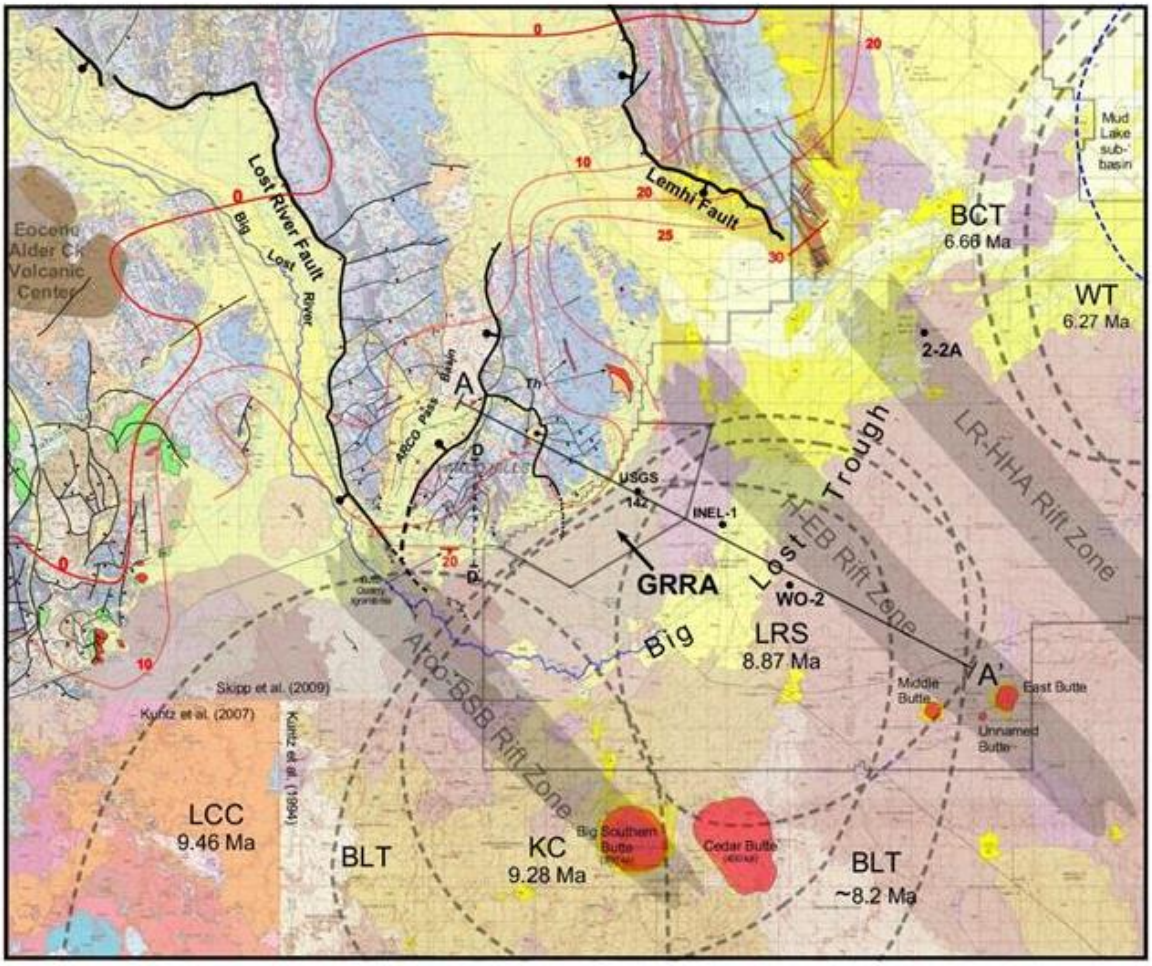

Figure 3. An intermediate scale geologic map of the GRRA and surroundings. Three base geologic maps are tiled together in the figure (Skipp et al., 2009; Kuntz et al., 2007; Kuntz et al., 1994). Neogene and Quaternary faults are highlighted in black; Quaternary rhyolite lava domes and cryptodomes in red shade. Picabo age and Heise age ignimbrites are also highlighted (in green and red colors, respectively). The geology base map is overlailn by inferred calderas (bold dashed lines); outlines of the Big Lost Trough basin and Mud Lake sub-basin are shown in thin dashed lines; red lines (red dots are measurement locations) that contour the tilt of Laramide fold axes into the plain (after Rodgers et al., 2002; McQuarrie and Rodgers, 1998); shaded regions illustrate volcanic rift zones; locations of deep boreholw (USGS142, INEL-1, WO-2 and 2-2A). The map also shows the locations of three project cross-section AA'.

Rhyolite fields may have cumulative volumes of 10,000-20,000 km^3 (e.g., Bonnichsen et al., 2008; Ellis et al., 2013). Volcanism is dominated by eruption of distinctively hot, relatively dry 'high grade' ignimbrites summarized by Branney et al. (2008) as SR-type, and voluminous lava flows. Similarities among the ignimbrites has made correlation, and therefore estimates of sources and volumes difficult, however recent work suggests that eruptions of >100 km^3 were not unusual. Many, but possibly not all (cf. Ekren et al., 1984), are sourced from caldera complexes. Assuming the cryptic volcanic fields (now largely buried by younger basalts) have evolved in a manner similar to Yellowstone caldera system, and to other large volcanic field world-wide, it seems likely that the fields host numerous overlapping and nested calderas. A prominent role for nesting of calderas is also strongly suggested by remarkably light patterns of oxygen stable isotope chemistry of the rhyolites (Bindeman et al., 2007; Watts et al., 2011; Drew et al., 2013).

Cessation of rhyolite volcanism was followed soon after by eruption of basalt lavas, beginning at ~6 Ma in the CSRP and ~4.2 Ma in ESRP (Shervais et al., 2013; Potter, 2014; Champion et al., 2002). The basalt eruptions produced a widely distributed basalt-dominated field consisting of hundreds of coalescing shield volcanoes (e.g., Greeley and King 1977; Kuntz et al., 1992; Hughes et al., 2002), having a cumulative volume of over 10,000 km^3 (e.g., McCurry et al., 2008). Accumulation of the basalts and concomitant subsidence of ESRP produced a basalt-dominated basin up to ~2 km deep (Shervais et al., 2013; Potter, 2014).

A number of spatially systematic patterns occur within ESRP basalt field (e.g., Kuntz et al., 2002, 1992; Hackett and Smith, 1992; Hughes et al., 2002; Wetmore et al., 2009) (Fig. 3). Many linear vents, alignments of vents and fracture systems trend to the northwest across parts of the ESRP, and west-northwest in the Spencer-Kilgore region south of the Centennial Range (e.g., Kuntz et al., 1992). Some of these features cluster into diffuse linear, northwest trending zones, and are identified as volcanic rifts zones (e.g., Kuntz et al., 1992, 2002; Rodgers et al., 2002). Some of these appear to merge into range bounding normal faults (e.g., Arco-Big Southern Butte Rift Zone, Figure 3), and may be dominantly tectonic in origin. Others may root into robust dike swarms (e.g., Parsons et al., 1998; Kuntz et al., 2002; Rodgers et al., 2002, 1990). The 'Great Rift' is the youngest and most prominent of these (e.g., Holmes et al., 2008). Interestingly, the Great Rift exhibits a systematic change in trend from northwest to northerly (Fig. 2), likely reflecting a northward change in the direction of regional strain (e.g., Payne et al., 2012). Other patterns in the distribution of volcanic vents have produced diffuse linear and curvilinear constructional topographic highs (e.g., 'Axial Volcanic Zone'; Fig. 3).

Basalt lavas are commonly interlayered with clastic sediment derived from drainage off ranges bounding the plain (e.g., Bestlin et al., 2002; Geslin et al., 2002). Importantly, accumulations of basalt and sediment in the central and eastern Snake River Plain have largely buried the underlying rhyolitic rocks and caldera systems. Virtually no unambiguous rhyolite sources are exposed, aside from those in the Yellowstone area (including Island Park). Volumes and sources of rhyolites in those regions are therefore inferred almost entirely from spatial distributions and depositional features of ignimbrite and fall deposits marginal to the plain, a small number of deep boreholes, and geophysical surveys.

In the ESRP eruptions of primitive basalts overlap in time and space with eruptions of comagmatic, highly geochemically evolved rocks, varying from Fe-enhanced and alkaline basalt to rhyolite (McCurry et al., 2008; Shervais et al., 2006; Leeman, 1982). These have produced a number of domes and cryptodomes across the ESRP such as Big Southern Butte and Middle Butte (Fig. 3), and evolved lava fields (e.g., Craters of the Moon, Cedar Butte, Unnamed Butte; Fig. 2, 3). Unlike the primitive basalt, parental magmas to these rocks underwent strong intracrustal fractional crystallization (e.g., Putirka et al., 2009, Whitaker et al., 2008) and remelting (e.g., Shervais et al., 2006; Bindeman et al., 2014). Hot cumulates associated with the long-lived active COM system (e.g., Kuntz et al., 1986), and voluminous young BSB system (e.g., McCurry et al., 2008), or possibly other cryptic (blind) systems across the ESRP, may be associated with localized thermal anomalies that are masked by the shallow active ESRP aquifer (e.g., McCurry and Welhan, 2012).

3. GEOPHYSICAL FRAMEWORK

Geophysical surveys have defined major features of the heat flow, crustal architecture, dynamics, seismicity, relative temperatures and distribution of fluids in the crust, lithosphere and deep mantle the YSRP region (e.g., Brott et al., 1981; Braile et al., 1982; Smith et al., 2009). Some aspects of these features are rapidly evolving as new EarthScope and GPS data continue to be gathered and interpreted (e.g., Payne et al., 2013). Some salient features are summarized here.

Numerous geophysical studies document prominent geophysical anomalies occur within the upper mantle and lower crust along the YSRP (e.g., Smith et al., 2009). Schmandt et al. (2012) identify low V_p and V_s seismic velocities extending from beneath Yellowstone to a depth of at least 1000 km. A prominent corridor of low velocity mantle also extends from the base of the crust to a depth of ~200 km along the entire ESRPA, lessening in magnitude from northeast to southwest beneath CSRP.

Kelbert et al. (2012) document a prominent region of low resistivity in the upper mantle beneath the ESRP, between 40 and 80 km depth. They interpret this as being produced by mantle containing 1-3% partial melt, comparable to melt fractions inferred from shear wave velocity (e.g., Wagner,2010; Schmandt et al. 2012). They also infer that mantle derived fluid may be preferentially rising into the lower crust preferentially along the margins of the ESRP. Interestingly, they also infer decoupling in the resistivity and seismic tomography data beneath Yellowstone indicating that the mantle under Yellowstone is depleted in fluid (magma), relative to regions of mantle under ESRP. Zhdanov et al. (2012; 2011) also infer low resistivity of upper mantle and lower crust beneath the SRP. However, in contrast to Kelbert et al., they also infer a plume-like region of low resistivity beneath Yellowstone. These and other regional geophysical surveys are compelling evidence for existence of melt, likely basaltic in composition, in the upper mantle and lower crustal regions of ESRP. It is plausible that the mantle underlying ESRP has been at or near its solidus (~1300°C) for the last 10 m.y.

Figure 4 illustrates a large-scale conceptual cross-section of the ESRP and surrounding regions that is based mainly upon the seismic and gravity model of Peng and Humphreys (1998). These authors build upon seismic and gravity work done in the 1970's and 1980's (e.g., Braile et al., 1982; Sparlin et al., 1982; Greensfelder et al., 1982; Smith and Braile, 1994). The model illustrates a crustal structure that is dominated by mafic lower crust, felsic crystalline upper crust and several kilometers of supracrustal rocks (the Cordilleran Miogeocline). Rocks directly beneath the ESRP are distinguished by presence of a mid-crustal region of unusually high density and a thin layer at or near the Moho that contains a significant fraction of melt.

McCurry et al.

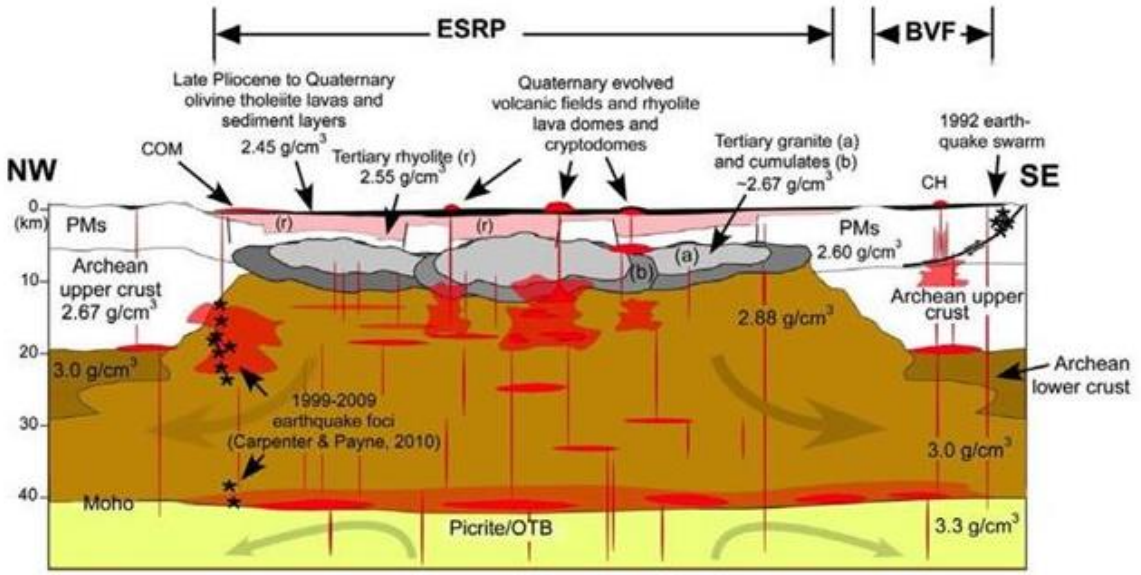

Figure 4. A cross-section of the crust and upper mantle (from McCurry and Welhan, 2012; modified from Peng and Humphreys, 1998). The cross-section extends southeast from the southern end of the Lost River Range to China Hat. ESRP = Eastern Snake River Plain; BVF = Blackfoot Volcanic Field; PMs = late Precambrian to Paleozoic miogeoclinal sedimentary rocks.

Importantly, the prominent mid-crustal density anomaly underlying the ESRP is inferred to be a product of intrusion of dense, hot (~1300°C) mantle derived melts (basalt) into pre-existing mid-crustal rocks (e.g., Brott et al., 1981; Smith and Braile, 1994). These initiated petrologic processes that culminated with eruption of rhyolite and intrusion of granitic rocks (e.g., Christiansen and McCurry, 2008; Szymanowski et al., 2015). McCurry and Rodgers (2009) applied a Nd- isotopic tracer method to extruded rhyolites as a method of inferring the original amount of mantle derived mass added to the crust, equating to a layer of gabbro ~14 km thick. Leeman et al. (2008) independently arrived at a similar estimate based on an energy balance analysis. Absence of a significant deviation of crustal thickness beneath ESRP, led Rodgers and McCurry (2009) to infer that the excess mass was transferred via lower crustal flow into regions marginal to the plain. This idea is supported in more recent geophysical work by Yuan et al. (2010); it is also consistent with geophysical work by DeNosquio et al. (2009) indicating that the mid-crustal 'sill' extends up to ~40 km southeast of the ESRP.

Geophysical constraints for the ESRP upper crust architecture include long baseline active seismic refraction (e.g., Sparlin et al., 1982; Braile et al., 1982) and resistivity (Zohdy and Stanley, 1973) surveys, and a seismic refraction survey focused on the northern margin of the ESRP (Pankratz and Ackermann, 1982). The seismic refraction and resistivity surveys indicate a steeply dipping northern, fault-like boundary to the ESRP, south of the Arco Hills and beneath GRRA, and consistent with a caldera margin in that region.

Interpretations of upper crustal structures from seismic, gravity and magnetic surveys data are complicated in the ESRP and CSRP regions by occurrence of interlayered basalts and sediment (e.g., Liberty et al., 2015). Josten and Smith (1997) analyzed Bouguer gravity data in the ESRP and inferred regions of likely buried calderas in the ESRP where low density, rhyolitic caldera fill plausibly abuts against higher density Paleozoic carbonate rocks.

4. GEOLOGY OF THE GRRA AREA

The surficial geology of the GRRA and vicinity are illustrated in Figures 3. Rocks exposed in the Pioneer, Lost River and Lemhi Ranges north of the plain are dominantly Paleozoic carbonate and siliciclastic rocks (purple and blue colors) that are deformed and cut by Sevier and Laramide folds and faults. The Paleozoic rocks are unconformably overlain by Eocene volcanic and volcaniclastic rocks of the Challis Formation (brown and tan colors). The closest of these, the Alder Creek complex, is located about 30 km northeast of GRRA. Distal sedimentary facies of that system are exposed in the Arco Pass basin, 5 km north of GRRA (Fig. 5). Eocene and older rocks underwent diachronous periods of late Eocene to early Oligocene and Miocene to Recent extension and related normal faulting. Oligocene extension is evident in a half graben in the Arco Hills (Arco Pass basin). The graben contains tilted Eocene Challis formation and an older gravel formation. These are overlain by less strongly tilted to nontilted gravels and thin discontinuous valley fill erosional remnants of ignimbrites of the Heise volcanic field in the Arco Hills and Picabo and Heise groups in the Pioneer and Lemhi Mountains. The graben bounding Arco Pass fault trends to the south-southwest, and apparently intersects with the active Lost River Fault near the town of Arco. A branch of the Arco Pass fault extends to the south, bisecting the Arco Hills, projecting to the south beneath the GRRA. However, there is no evidence for Miocene or younger offset on that fault.

Miocene to Recent normal faulting has produced the current fault block physiography of the region. Prominent range bounding active normal faults include the Lost River and Lemhi Fault systems (e.g., Janecke et al., 1993; Bruhn et al, 1992; Wu and Bruhn, 1994). The

Lost River fault projects to the south into a diffuse system of small-offset normal faults referred to as the Arco Rift Zone (e.g., Kuntz et al., 1992; Kuntz and Cork, 1978; Jackson et al., 2006).

McQuarrie and Rodgers (1997) and Rodgers et al. (2002) document progressive southward tilting of originally horizontal late Mesozoic fold axes and in volcanic and volcaniclastic deposits of the Heise volcanic group. Tilt contours are illustrated in Figure 3. These structures document ~20 km wide zone marginal to the ESRP in which tilts increase from zero to 20-30 degrees to the south, accommodating 4.5 to 8.5 of subsidence of the plain, most which occurred ~10 and 8.5 Ma in the GRRA area. Minor east-northeast trending normal faults are inferred to have been produced by flexure of the brittle crust. Contour reentrants coincide with major Quaternary grabens indicating that the reentrants are artifacts of Quaternary faulting and basin formation.

The southernmost ends of the Pioneer, Lost River and Lemhi Ranges are cut by an unusually high density of small-offset, crosscutting normal faults (Fig. 3). Bruhn et al. (1992) indicate that those in the southern Lemhi Mountains are a product of complex fault tip evolution of the Lemhi fault (e.g., their Figure 10). Morgan (1984) suggested that some of the small faults could be related to normal fault ring fracture zones bordering calderas that may reside a short distance to the south of the ranges.

Quaternary structures in the GRRA area are dominantly northwest trending. However, proposed cryptic calderas clustered near the southern margin of the Lost River Range imply existence of related cryptic curvilinear ring fault systems beneath basalts, perhaps 10's km long and several kilometers deep. Some of these are likely to have orientations that intersect at high angles with Quaternary structures.

Basalt lavas produced mainly from overlapping shield volcanoes dominate areas south of the mountain ranges. Surficial basalts near GRRA vary in age from ~300 to ~200 ka (Skipp et al., 2009) and do not appear to have significant tectonic tilt. Near the ranges the basalts feather out and are interbedded and discontinuously overlain by range derived clastic sediment. Sediment interbeds also commonly occur in borehole cores and logs (e.g., Bestland et al., 2002; Geslin et al., 2002). Most appear to record transient fluvial, lacustrine and eolian processes. However sedimentation associated with the Big Lost Trough (Fig. 3) appear to have been unusually robust and long-lived. Current drainage into that system includes the Big Lost River, Little lost River and Birch Creek. The largest, the Big Lost River, has an unusual drainage pattern defined by southward flow from the Big Lost Graben, followed by deflection to the east and then north by constructional volcanic features of the 'axial volcanic zone'. Based upon borehole studies, sedimentation associated with that system occurs to at least 2.5 Ma (e.g., Geslin et al., 2002).

Hundreds of boreholes have been drilled across INL, focused on defining stratigraphic and structural features relevant to understanding the hydrogeology and hydrochemistry of the ESRP aquifer, and for monitoring fate and transport of site related contaminants (e.g., Bartholomay and Twining, 2015; Champion et al., 2011). Many of the boreholes have core samples, almost all have downhole geophysical logs (most importantly gamma logs). These have been used to produce detailed subsurface correlation maps of basalt and sediment interbed layers, typically to depths of ~200 meters (e.g., Figure 4B, C). Significant results of these studies include, 1. documentation of spatial distribution of lava accumulation rates, 2. long term existence of the Big Lost Trough, 3. little or no tilting of basalt layers up to at least ~1 Ma, 4. little or no faulting, 5. Little or no systematic time sequential change in basalt lava chemistry that are characteristic of waning phases of hot spot activity.

4.1 Deep borehole geology

Several boreholes penetrate through the entire basalt section in the GRRA and INL area, INEL-1 (to 3.16 km), WO-2 (to 1.52 km), 2-2A (to 910 m), and most recently USGS 142 (to 573 m). Other regional deep boreholes include those of Project Hotspot (Kimberly, to 1958 m, and Kimama, to 1912 m; e.g., Shervais et al., 2013; Potter, 2014), and the Sugar City borehole (Embree et al., 1978). The Kimberly borehole penetrates 1350 m of homogeneous, intracaldera-like rhyolite (Knott et al., 2013) and referred to by Shervais et al. (2013) as the 'Twin Falls caldera'.

Summaries of salient aspect of borehole stratigraphy near GRRA are illustrated in Figure 5. Rhyolites exposed in boreholes WO-2 (e.g., Anders et al., 2014; McCurry and Rodgers, 2009) and 2-2A (Dougherty, 1979) are dominated by two rhyolite lava flows, and thin outflow ignimbrites (i.e. deposited outside of their source calderas) of the Heise volcanic field. The WO-2 borehole bottoms-out in one of the most voluminous Heise ignimbrite units (the Blacktail Creek tuff), but it is not clear whether it is within or outside of a source caldera.

McCurry et al.

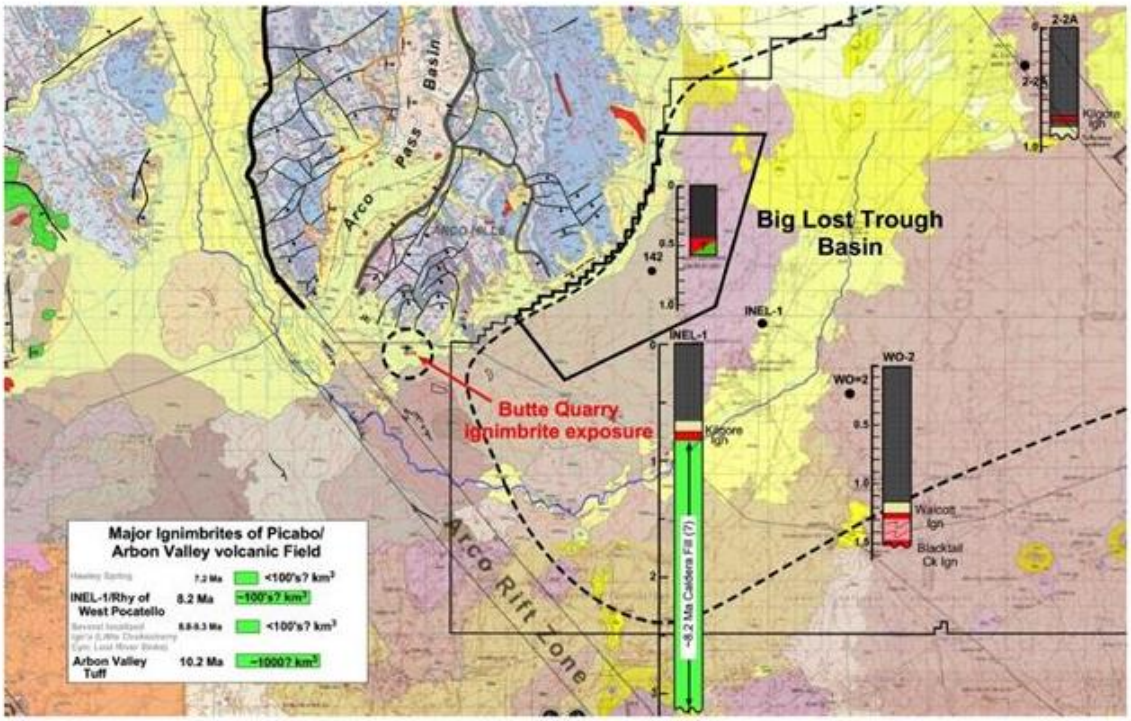

Figure 5. Summary map illustrating volcanic rock stratigraphy observed in boreholes INEL-1, 2-2A, WO-2 and USGS 142. Green: rhyolite correlated with the Picabo volcanic field; red: rhyolite correlated with the Heise volcanic field.

The INEL-1 borehole penetrates ~2.5 km of rhyolite below of basalt cover of ~750 m (total depth of ~3.2 km). Rhyolite sampled at ~770 m may correlate to outflow facies of the Tuff of Kilgore (McBroome et al., 1981; cf. Anders, et al., 2014).

Importantly, three cored intervals from INEL-1, extending over a range of depth of 1.1 to 3.2 km, yielded rhyolites containing zircon phenocrysts having overlapping U-Pb SHRIMP dates of ~8.2 Ma (McCurry and Rodgers, 2009; Drew et al., 2012). Phenocryst textures of these rocks are typical of SR-type rhyolite (after Branney et al., 2008). Drew et al. (2012) point out that rhyolite at ~1.5 km depth bears striking geochemical similarities to a possible lavalike ignimbrite near Pocatello (Rhyolite of West Pocatello). They suggest that they may be correlative parts of a particularly large ignimbrite. If the 8.2 Ma rhyolites of INEL-1 are extrusive, as seems likely, then they are clear evidence for existence of a Picabo-age caldera in the GRRA area (referred to here as the 'Big Lost Trough caldera').

Figure 5 illustrates a simplified lithologic log for recently drilled borehole USGS 142. This borehole is located near the center of GRRA, and therefore provides key stratigraphic control in that area to a borehole bottom depth of 573 m. The borehole penetrates 425 meters of basalt lavas, and lesser amounts of sediment interbeds. However the lower portion of the borehole penetrates through a single ignimbrite ~150 m thick. Petrographic examinations of core from upper and lower parts of the ignimbrite exhibit clear eutaxitic textures indicative of its pyroclastic origin. Interior parts of the ignimbrite exhibit banding and rheomorphic features that are typical of SR-type rhyolitic ignimbrites. Examination of variation in intensity of welding of the bottom-hole core suggests that the base of the ignimbrite occurs with a few meters of that depth. Preliminary examination of the bulk major and trace-element composition and petrography of the rhyolite indicates that it is not correlated to any of the large Heise ignimbrites. Dating and additional geochemical work on the rhyolite are in progress. The 150 m thick ignimbrite is thicker than most regional outflow ignimbrites. We speculate that the ignimbrite could be an upper cooling unit of the Big Lost Trough (BLT) caldera, perhaps from the same sequence that occurs in borehole INEL-1. However it could also be an outflow of the BLT caldera resting on country rocks, or an outflow unit of some as yet unidentified caldera that erupted soon after the BLT caldera, and that ponded within the moat region of the BLT caldera.

5. CALDERAS AND THEIR SIGNIFICANCE FOR EGS EXPLORATION IN ESRP

Calderas are perhaps the single most important structural and lithologic (rock materials) features of the ESRP with regard to its EGS potential (e.g., Podgorney et al., 2013; Moody and Plummer, 2014; Wohletz and Heiken, 1992). Key geologic requirements for successful FORGE development in GRRA include a rock reservoir that is shallow enough to drill to obtain necessary temperature (assumed to be in the 1.5 to 4 km depth range at GRRA), homogeneous (i.e. free of strong stratification, joint systems, foliations or other characteristics of rock anisotropies), voluminous, dense (i.e. low fracture density and low porosity) and dry. In a rhyolite dominated volcanic terrain such as YSRP the best fit for these criteria would be the intracaldera facies of a major ignimbrite eruption (e.g., Wilcock et al., 2013; Wohletz and Heiken, 1992).

We summarize the major features of caldera systems, including relevant aspects of their nomenclature, classification, and formation, mainly following review papers by Branney and Acocella (2015), Acocella (2006; 2007), Cole et al. (2005), and Lipman (1997). We then summarize a rationale for inferring existence, sizes, depths and locations of numerous cryptic calderas that underlie basalts across ESRP (e.g., Anders et al. 2014; Morgan and McIntosh 2005).

5.1 Caldera systems

Calderas are subsided regions that form in response to rapid, voluminous magma transfer from shallow (upper crust) magma reservoirs (Branney and Acocella, 2015). Five end-member types of calderas are widely recognized (e.g., Lipman 1997; Cole et al. 2005), including Piston, Piecemeal, Trap-door, Downsag and Funnel (Figure 6). Most large explosive eruptions $\geq$ ~10 km^3 produce calderas. However some may not (Ekren et al. 1984). Additionally, some calderas are non-eruptive, collapse being brought about by lateral transfer of magma within laterally extended magma reservoirs (Lipman 2008). Correlated patterns between caldera area, caldera depth and erupted magma volumes have been defined by studies of young calderas in diverse geologic environments (e.g., Acocella, 2007; Gregg et al., 2012). Eruptions of 100's to 1000's km^3 (common along the YSRP) typically produce calderas 20 to 50 km across and 1-3 km deep.

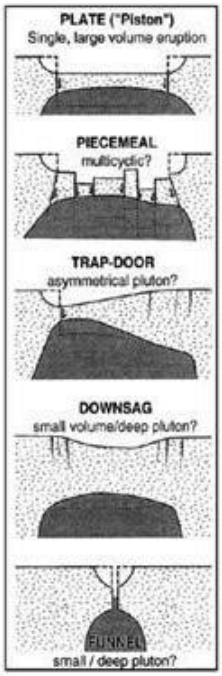

Figure 6. Types of calderas and caldera classification (from Acocella, 2006).

Development of large silicic explosive-volcanism-related calderas generally represent the climax of activity of regionally extensive volcanic fields (e.g. Lipman et al., 2015). These volcanic systems evolve through a waxing and waning sequence of events lasting ~10^4 – 10^6 years and referred to and described by Smith and Bailey (1968) as the 'resurgent-cauldron cycle' and subsequently elaborated on and modified in numerous subsequent studies (e.g., Walker, 1984; Lipman, 1997; Cole, 2006; Acocella, 2006, 2007).

Activity begins with development of a precaldera volcanic field consisting numerous small and compositionally diverse volcanoes. Incremental assembly of a magma reservoir at depths of ~5-10 km leads to eventual catastrophic eruption via reverse ring fracture systems up to 10's kilometers long. Ring fractures generally conform to the shape of the underlying magma reservoir(s), but may also be affected by pre-existing structures and regional stresses. Explosive jetting from the vents produces hot fragmental volcanic debris that collapses back to ground as pyroclastic density currents (PDC) (e.g., Wilcock et al., 2013) that incrementally produce deposits referred to as ignimbrites. Many of the PDC's infill into the subsiding caldera depression, and may rapidly accumulate to thickness of a kilometer or more, exceeding the thickness of coeval ignimbrites formed beyond the margins of the caldera by a factor of 10 or more. Owing to their rapid accumulation near source vents the resulting intracaldera deposit is generally massive and densely welded.

Calderas produce patterns of structures and deposits. Acocella (2006, 2007) describes four time sequential stages of evolution. Caldera development begins with downsagging (stage 1), followed by formation of reverse ring-fracture faults along which most magmas are erupted (stage 2), followed by additional downsagging (stage 3) and finally collapse of roof wall rocks via a system of normal ring

faults (stage 4). Over-steepened walls of normal fault scarps produces a 'collar structure' consisting of scalloped shaped landslide scars, and landslide debris into the caldera as mega- and mesobreccia. Collar zones and regions of sagging and incipient collapse-related normal and reverse faults may occur in a zone up to kilometers outside of the ring-fracture and vent systems for the caldera. Major caldera-bounding ring fracture faults and related vents are curvilinear and may be ~10's km long in the largest calderas. Intracaldera vents may be linear, curvilinear or complex.

Postcaldera activity commonly involves strong hydrothermal alteration of caldera fill owing to capture of meteoric water into the caldera depression and shallow heat sources. This may be a particularly robust process in YSRP caldera systems as suggested by occurrence of remarkably light $\delta^{18}O$ of latter erupted rhyolites relative to those erupted earlier in nested caldera fields (Bindeman et al., 2007; Watt et al., 2011; Drew et al., 2013).

Post-collapse activity also commonly includes extrusion of degassed rhyolite magma along ring-fracture faults, deposition of lacustrine and fluvial sediment within the caldera, and in the case of many large calderas uplift of central regions of the floor of the caldera ('resurgent doming'; e.g., Kennedy et al., 2012) by intrusion of sills (e.g., Fridrich et al., 1991; Kawakami et al. 2007) or by renewed deeper intrusive activity by nonerupted remnants of the underlying magma body (e.g., Lipman 1984; Smith and Bailey 1968; de Silva et al., 2015). Uplift commonly produces radial and linear normal fault systems. Multiple resurgent domes are formed with some very large calderas (e.g., San Juan and Yellowstone calderas, e.g., Christiansen, 2001; Casadevall and Ohmoto, 1977). These may be connected by systems of normal faults and fractures (Christiansen, 2001; Casadevall and Ohmoto, 1977. CCDB proposes a detailed nomenclature for calderas based upon key aspects of post-caldera activity (Geyer and Marti, 2008). Figure 7 illustrates a simplified integrated model of a caldera (Branney and Acocella 2015).

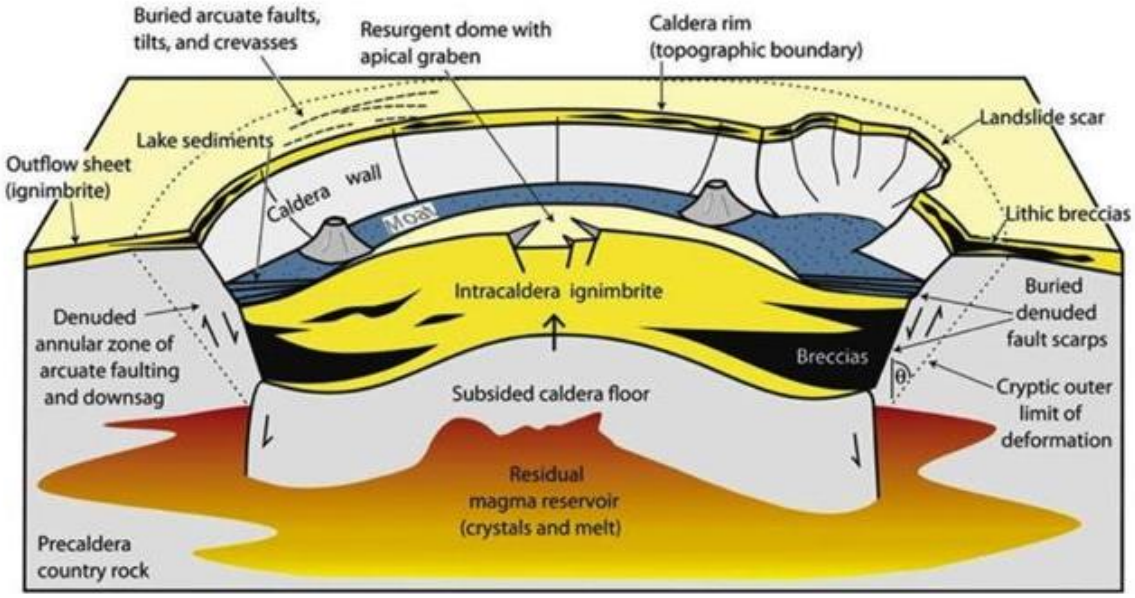

Figure 7. A conceptual model of a resurgent caldera (after Branney and Acocella (2015). The region labeled "Denuded annular zone of arcuate faulting and downsag" and with lanslide scars is equivalent to the 'collar zone' of Lipman (1997).

Major silicic volcanic fields commonly form complex overlapping, 'nested', calderas . These differ from piecemeal calderas in that they form in diachronous events that may be hundreds of thousands to millions of years apart in time (e.g., Lipman, 1997; Christiansen, 2001). Nesting may produce cumulative subsidence of many kilometers. Caldera nesting occurs in the Yellowstone volcanic field (Christiansen et al., 2001). Volcanological (e.g., Morgan and McIntosh, 2005; Anders et al., 2014) and geochemical studies (Bindeman et al., 2007; Watts et al., 2011; Drew et al., 2013) suggest that it is a also common feature of other parts of the YSRP volcanic track.

5.2 Criteria for identifying and locating cryptic (buried) calderas

Inference of cryptic calderas in the central and eastern Snake River Plain have been made on the basis of:

1. Correlation, and volcanic facies and kinematic analyses of caldera-related volcanic materials, mainly ignimbrites and ring-fracture lava flows (e.g., Anders et al. 2009, 2014; Morgan and McIntosh, 2005; Morgan et al., 1984, 2008; Morgan, 1988, 1992; Kellogg et al., 1994; Prostka and Embree, 1978; Embree et al., 1982);

2. Caldera-related structures including an inferred resurgent dome (Morgan and McIntosh, 2005) and possible caldera-related normal and collar faults (e.g., Morgan et al. 1984; Morgan,1988);

3. Studies of deep boreholes that penetrate through shallow basalts into the underlying rhyolites (e.g., Doherty et al., 1979; McCurry and Rodgers, 2009; Anders et al., 2014);

4. Spatial distributions of basalt and rhyolite lava dome vents (e.g., Doherty et al., 1979; Kuntz and Dalrymple, 1979; Kuntz, 1992);

5. Persistent regions of sediment accumulation (e.g., Kuntz et al., 1992);

6. Seismic surveys (Pankratz and Ackermann, 1979: Braile et al., 1982; Sparlin et al. 1982);

7. Resistivity surveys (Zohdy and Stanley, 1973);

8. Interpretations of gravity and magnetic anomalies (Josten and Smith, 1997; Mabey, 1978, 1982).

5.3 Distribution of calderas in ESRP (Picabo and Heise volcanic fields)

Figures 2 and 3 illustrates the inferred locations of calderas in the ESRP. Dashed lines are intended to encompass source vents for the respective calderas; they do not distinguish between caldera wall, and normal and reverse ring fault systems (Fig. 6). Existence and locations of calderas follow mainly from previous syntheses by Anders et al. (2014), Shervais et al. (2013), Morgan (1984, 1988), and Morgan and McIntosh (2005). Examinations of deep boreholes indicate that calderas associated with the Heise volcanic field (≤6.66 Ma) are located to the east of borehole INEL-1 and likely east of borehole WO-2. Three of the cluster of four nested calderas shown in the GRRA area (Fig. 3) are inferred from relatively small erosional remnants of outflow ignimbrites in the southern Pioneer and White Knob Mountains (Anders et al., 2014). The locations and sizes of those calderas are therefore weakly constrained and may differ by many kilometers from the boundaries shown in the figure. A fourth caldera, referred to here as the Big Lost Trough caldera, is added to the Anders et al. (2014) map. This caldera is a modification of the INEL-1 caldera proposed by Dougherty et al. (1979), and is inferred from previously described seismic refraction (Pankritz and Ackerman, 1982) and resistivity surveys (Zohdy and Stanley, 1973), and deep boreholes (INEL-1 and USGS 142). We suggest that it is also broadly coincident with, and likely has contributed to the existence of the Big Lost Trough sedimentary basin. The northern boundary of the outer wall of this buried caldera may be accurate to within a kilometer, based largely upon seismic refraction work by Pankratz and Ackermann (1982).

6. GRRA STUDY AREA: A PRELIMINARY CROSS-SECTION INTERPRETATION

Figure 8 illustrates a northwest-southeast cross-section of the GRRA and surroundings.

McCurry et al.

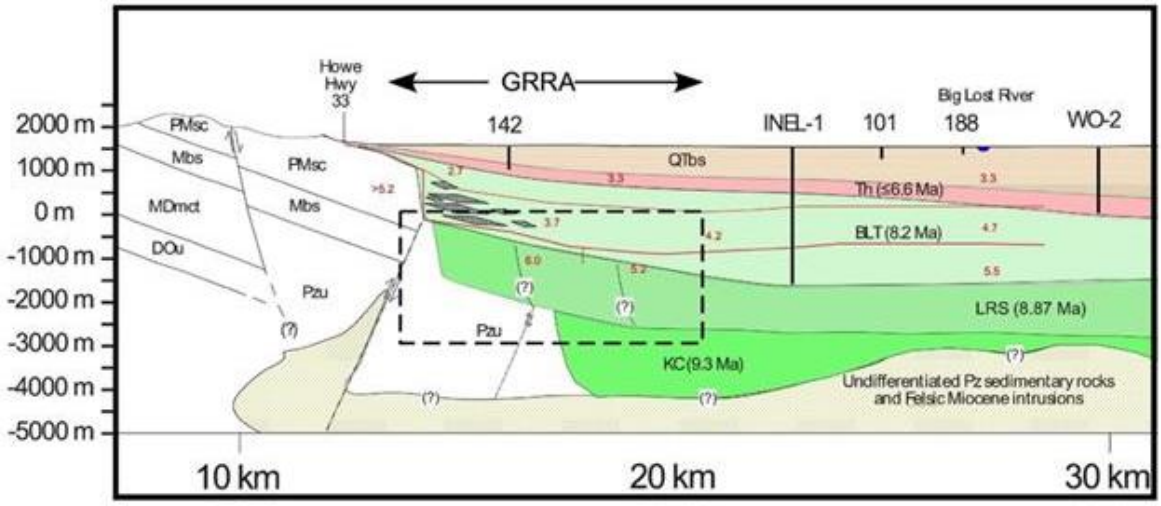

Quaternary-Late Neogene

Qalf - alluvial and fluvial deposits (includes Qc - colluvial deposits)
Qr - rhyolite lava dome (Pleistocene)
QTg - gravels, glacial and other sources (Holocene to Pliocene)
QTbs - basalt of the ESRP (Holocene to Pliocene)
Th - Heise group rhyolite ignimbrites (6.66 to 4.5 Ma)
BC - Blacktail Creek ignimbrite of Heise group (6.66 Ma)
Tp - Picabo group rhyolite ignimbrites (10.2 - 7.7 Ma)
BLT - 'Big Lost Trough' ignimbrite (~8.2 Ma)
LRS - Lost River Sinks ignimbrite (8.87 Ma)
KC - Kyle Canyon ignimbrite (9.28 Ma)
LCC - Little Choke Cherry ignimbrite (9.46 Ma)
TAV - Arbon Valley ignimbrite (10.2 Ma)
Tgu - upper gravel sediments (Miocene to Oligocene)
Tgl - lower gravel sediments (Eocene)
Tcv - Challis group volcanics (Eocene)

Paleozoic and Proterozoic sedimentary units

PMsc - Calcareous sandstones and limestones
Mbs - Quartzite, limestone and dolostones
MDmct - Siliceous sandstones, quartzite and limestones
DOu - Undifferentiated dolostone
OYu - Quartzites and calcareous sandstones

Figure 8. Blow-up view of the part of cross-section AA' (Fig. 3) near the GRRA. Numbers across the top of the figure indicate boreholes located close to the cross-section (mostly with USGS prefix). Faint red lines and numbers are model boundaries and seismic velocities from Pankhurst and Ackermann (1982). The dashed box illustrates the potential GRRA reservoir target zone (assumed to be 1.5 – 4 km depth). Stippled regions near caldera boundaries represent likely mega- and mesobreccia rich regions. Question marks indicate uncertainty in location of the deeper nested Picabo-age caldera boundaries. The diagram illustrates that USGS 142 penetrates into Th (Heise volcanics, undifferentiated). New geochemical data suggest that it is either an unknown Heise unit, or a Picabo unit.

Approach and uncertainties: Cross-sections are constrained by surface geology, borehole data and caldera locations as defined in the previous section. At present there are no unambiguous constraints for common features of calderas, such as structural collars, megabreccia zones, resurgent dome structures, moat deposits or hypabyssal intrusions (illustrated diagrammatically in Fig. 8). We therefore omit these from the cross-sections with the understanding that some or all of these are likely present.

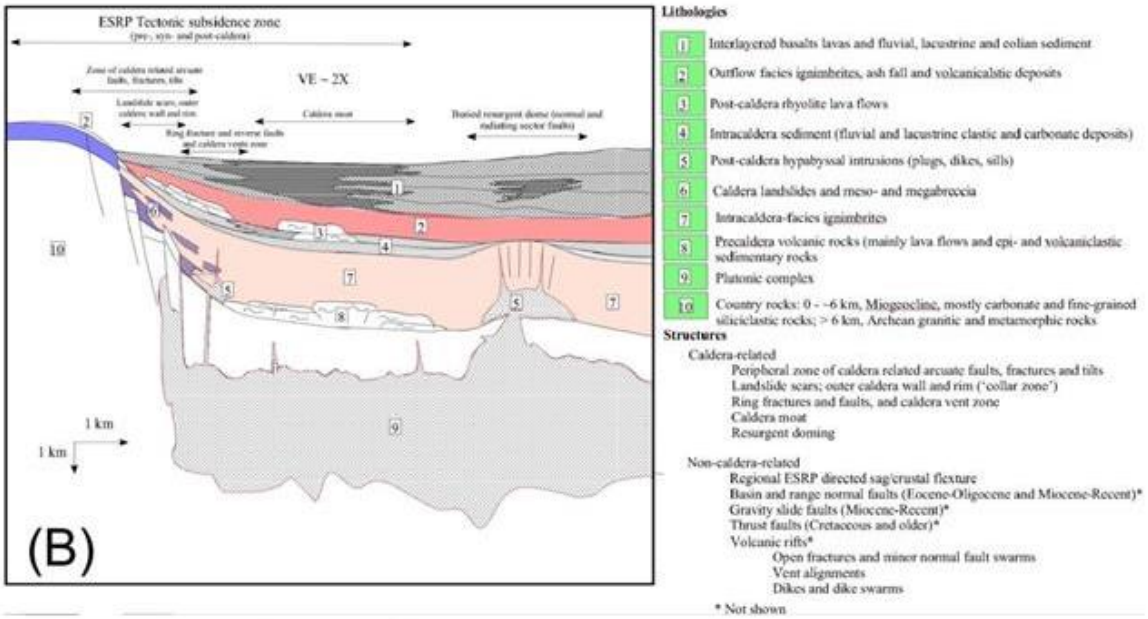

Figure 9. A conceptual model illustrating possible lithologies and structures in the GRRA area.

The cross-section extends from the Arco Hills to the southeast across the center of GRRA, It roughly parallels the seismic survey line of Pankratz and Ackermann (1982) and the resistivity survey of Zohdy and Stanley (1973). It also crosses close to three deep boreholes (USGS 142; INEL-1; and WO-2). It is therefore the best constrained cross-section currently possible for reservoir-depth interpretation. Long vertical red lines illustrate basalt vents that reach to modern surface. Faint red lines and red numbers illustrate the velocity model boundaries and modeled seismic velocities of Pankratz and Ackerman (1982). The diagram illustrates three nested calderas (KC - Kyle Canyon, LRS - Lost River Sinks and BLT). Each is assumed to contain ~1 km of caldera fill, and that the fill extends to the top of ring fracture normal faults. Deeper, older calderas (KC and LRS) are inferred to tilt more strongly into the plain than the young BLT caldera (following from subsidence timing constraints of Rodgers et al., 2002). We assume a total flexure-related subsidence of ~4 km (the minimum estimate of Rodgers et al., 2002). As illustrated in the Figure, host rocks are likely to be Picabo age intracaldera rhyolites. Thicker, more homogeneous reservoir rocks are more likely to occur beneath the southeastern parts of the GRRA.

6.1 GRRA Reservoir Hypotheses

Figure 10 illustrates plausible worst-case and best-case geologic conceptual model hypotheses for the proposed GRRA reservoir. The models are simplified to emphasize characteristics of the likely rhyolite-dominated reservoir rocks. Other details of rock lithologies and structures are neglected (cf. Figure 9). The 2-d conceptual models corresponds to cross-section AA', Figure 3.

McCurry et al.

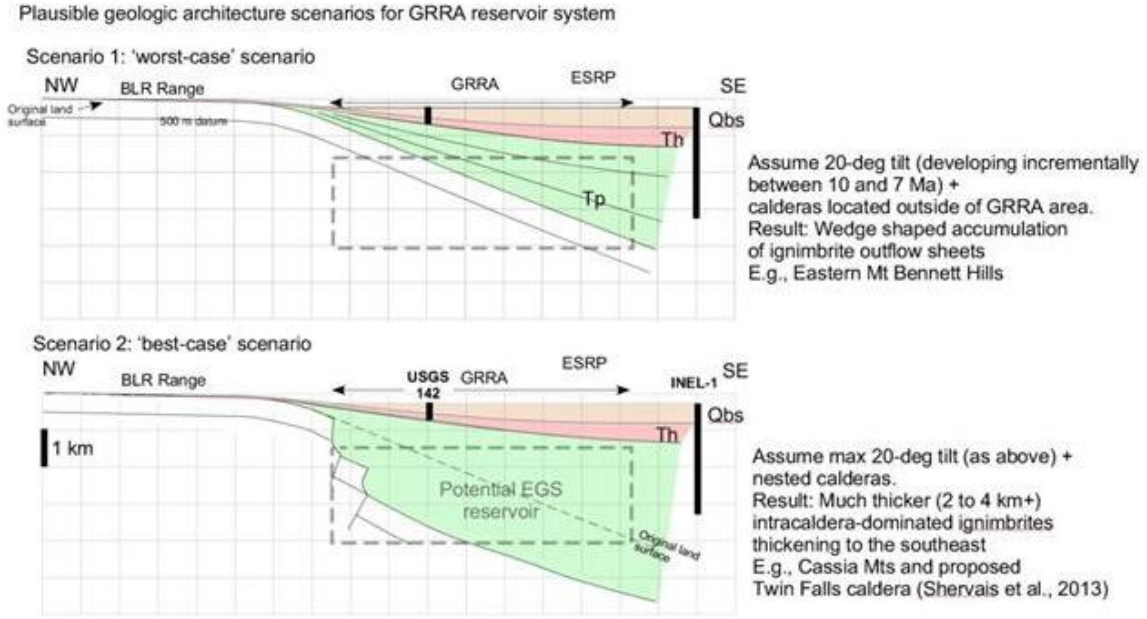

1. Worst-case: wedge of thin outflow ignimbrite sheets; thinning to NW, cumulative thickness decreasing roughly linearly from ~3 km under SE parts of GRRA to less than a few hundred meters under NW parts of GRRA.

2. Best-case: Deep nested calderas; overlapping or nearly overlapping narrow steep caldera walls and narrow collar; 2-4 km (or more if multiple nested calderas) of densely welded intracaldron ignimbrites. Other 'best case' features:
   - minimal landslide mega- and meso-breccia
   - 'moat region' of caldera; no resurgent doming, or resurgent dome located far enough away to neglect it
   - narrow cooling break; minimal lacustrine or other intercaldera deposits
   - little post caldera tectonic or volcanic and intrusive activity aside from incremental deposition of basalt lavas and sediment

Figure 10. This figure is intended to bracket a plausible range of subsurface architecture for the GRRA..

Worst case scenario: In the worst case scenario, caldera boundaries occur outside of the GRRA area. Basin development is solely a product of flexure subsidence of the plain. In this case rhyolites are dominantly outflow facies of ignimbrites (i.e. relatively thin and discontinuous). This model predicts that the southern half of GRRA would host potentially suitable reservoir host rocks.

Best-case scenario. In this scenario one or more nested caldera margins overlap close to the southern margin of the Arco Hills. Caldera collapse, enhanced by flexure tilting could produce thick, dense, homogeneous intracaldera reservoir rocks that encompass nearly the entire potential reservoir region. Seismic refraction data of Pankurst and Ackmann (1982), indicating a sharp drop in basement depth, suggests that this scenario may be closer to the actual case.

6. CONCLUSIONS

Preliminary 2-d modeling of the geologic and geophysical characteristics of the GRRA are consistent with a high probability of favorable types of EGS host rocks at potential reservoir depths of 1.5 to 4 km, particularly towards the southern and southeast parts of the GRRA. Reservoir depth rocks are likely to be dominated by marginal or moat, intracaldera ignimbrite-facies of caldera systems. Calderas are likely to be nested. Boreholes may therefore encounter diverse sedimentary deposits, lava flows or caldera collapse breccias between intracaldera ignimbrites.

The large potential magnitude of the EGS resource and unique combinations of favorable reservoir-depth host rocks and a shallow robust aquifer system indicate that GRRA is an ideal site for EGS research and development.

REFERENCES

Acocella, V., 2006, Caldera types: How end-member relate to evolutionary stages of collapse: Geophysical Research Letters, v. 33, no. 18, p. 2–6, doi: 10.1029/2006GL027434.

Acocella, V., 2007, Understanding caldera structure and development: An overview of analogue models compared to natural calderas: Earth-Science Reviews, v. 85, no. 3-4, p. 125–160, doi: 10.1016/j.earscirev.2007.08.004.

Acocella, V., Funiciello, R., Marotta, E., Orsi, G., and De Vita, S., 2004, The role of extensional structures on experimental calderas and resurgence: Journal of Volcanology and Geothermal Research, v. 129, no. 1-3, p. 199–217, doi: 10.1016/S0377-0273(03)00240-3.

Anders, M.H., Geissman, J.W., Piety, L.A., and Sullivan, J.T., 1989, Parabolic distribution of circumeastern Snake River Plain seismicity and latest Quaternary faulting: Migratory pattern and association with the Yellowstone hotspot: Journal of Geophyscial Research, v. 94, no. B2, p. 1589–1621, doi: 10.1029/JB094iB02p01589.

Anders, M.H., Rodgers, D.W., Hemming, S.R., Saltzman, J., Divenere, V.J., Hagstrum, J.T., Embree, G.F., and Walter, R.C., 2014, A fixed sublithospheric source for the late Neogene track of the Yellowstone hotspot: Implications of the Heise and Picabo volcanic fields: Journal of Geophysical Research: Solid Earth, v. 119, no. 4, p. 2871–2906, doi: 10.1002/2013JB010483.

Anders, M.H., Saltzman, J., and Hemming, S.R., 2009, Neogene tephra correlations in eastern Idaho and Wyoming: Implications for Yellowstone hotspot-related volcanism and tectonic activity: Bulletin of the Geological Society of America, v. 121, no. 5-6, p. 837–856, doi: 10.1130/B26300.1.

Armstrong, R.L., Leeman, W.P., and Malde, H.E., 1975, K-Ar dating, Quaternary and Neogene volcanic rocks of the Snake River Plain, Idaho: American Journal of Science, v. 275, p. 225–251, doi: 10.2475/ajs.275.3.225.

Bartholomay, R.C., and Twining, B. V., 2015, Hydrologic Influences on Water-Level Changes in the Eastern Snake River Plain Aquifer at and near the Idaho National Laboratory , Idaho , 1949 – 2014 Scientific Investigations Report 2015 – 5085: U. S. Geological Survey Scientific Investigations Report, v. 2015-5085, p. 37.

Bestland, E.A., Link, P.K., Lanphere, M.A., and Champion, D.E., 2002, Paleoenvironments of sedimentary interbeds in the Pliocene and Quaternary Big Lost Trough (eastern Snake River Plain, Idaho): Geological Society of America Special Paper, v. 353, p. 27–44.

Bindeman, I.N., and Simakin, A.G., 2014, Rhyolites — Hard to produce , but easy to recycle and sequester : Integrating microgeochemical observations and numerical models: Geosphere, v. 10, no. 5, p. 930–957, doi: 10.1130/GES00969.1.

Bindeman, I.N., Watts, K.E., Schmitt, A.K., Morgan, L. a., and Shanks, P.W.C., 2007, Voluminous low δ18O magmas in the late Miocene Heise volcanic field, Idaho: Implications for the fate of Yellowstone hotspot calderas: Geology, v. 35, no. 11, p. 1019, doi: 10.1130/G24141A.1.

Bonnichsen, B., Leeman, W.P., Honjo, N., McIntosh, W.C., and Godchaux, M.M., 2007, Miocene silicic volcanism in southwestern Idaho: geochronology, geochemistry, and evolution of the central Snake River Plain: Bulletin of Volcanology, v. 70, p. 315–342, doi: 10.1007/s00445-007-0141-6.

Braile, L.W., Smith, R.B., Ansorge, J., Baker, M.R., Sparlin, M.A., Prodehl, C., Schilly, M.M., Healy, J.H., Mueller, S., and Olsen, K.H., 1982, The Yellowstone-Snake River Plain seismic profiling experiment: Crustal structure of the Eastern Snake River Plain: Journal of Geophyscial Research, v. 87, no. B4, p. 2597–2609.

Branney, M., and Acocella, V., 2015, Calderas, *in* Sigurdsson, J., Houghton, B., McNutt, S.R., and Stix, J. eds., Encyclopedia of volcanoes, Elsevier/Academic Press, New York.

Branney, M.J., Bonnichsen, B., Andrews, G.D.M., Ellis, B., Barry, T.L., and McCurry, M., 2008, "Snake River (SR)-type" volcanism at the Yellowstone hotspot track: Distinctive products from unusual, high-temperature silicic super-eruptions: Bulletin of Volcanology, v. 70, p. 293–314, doi: 10.1007/s00445-007-0140-7.

Brott, A., Blackwell, D.D., and Ziagos, J.P., 1981, Thermal and tectonic implications of heat flow in the Eastern Snake River Plain , Idaho: Journal of Geophyscial Research, v. 86, no. B12, p. 11709–11734.

Bruhn, R.L., Wu, D., and Lee, J.-J., 1992, Final report on structure of the southern Lemhi and Arco Fault Zone, Idaho. EGG-NPR-10680 Informal Report prepared for U.S. Department of Energy.

Camp, V.E., Pierce, K.L., and Morgan, L.A., 2015, Yellowstone plume trigger for Basin and Range extension, and coeval emplacement of the Nevada–Columbia Basin magmatic belt: Geosphere , v. 11 , no. 2 , p. 203–225, doi: 10.1130/GES01051.1.

Carpenter, N.S., and Payne, S.J., 2009, Deep, long-period earthquakes in and around Craters of the Moon National Monument, Idaho: Seismological Research Letters, v. 80, p. 350.

Champion, D.E., Hodges, M.K. V., Davis, L.C., and Lanphere, M.A., 2011, Paleomagnetic Correlation of Surface and Subsurface Basaltic Lava Flows and Flow Groups in the Southern Part of the Idaho National Laboratory , Idaho , with Pleomagnetic Data Tables for Drill Cores Scientific Investigations Report 2011 – 5a049: U. S. Geological Survey Scientific Investigations Report, v. 2011-5049, p. 33.

Champion, D.E., Lanphere, M.A., and Kuntz, M.A., 2002, Accumulation and subsidence of late Pleistocene basaltic lava flows of the eastern Snake River Plain, Idaho, *in* Link, P.K. and Mink, L.L. eds., Geological Society of America Special Paper, Geological Society of America, p. 175–192.

Christiansen, E.H., and McCurry, M., 2008, Contrasting origins of Cenozoic silicic volcanic rocks from the western Cordillera of the United States: Bulletin of Volcanology, v. 70, no. 3, p. 251–267, doi: 10.1007/s00445-007-0138-1.

Cole, J., Milner, D., and Spinks, K., 2005, Calderas and caldera structures: a review: Earth-Science Reviews, v. 69, no. 1-2, p. 1–26, doi: 10.1016/j.earscirev.2004.06.004.

DeCelles, P.G., and Coogan, J.C., 2006a, Regional structure and kinematic history of the Sevier fold-and-thrust belt, central Utah: Geological Society of America Bulletin, v. 118, no. 7-8, p. 841–864, doi: 10.1130/B25759.1.

DeNosaquo, K.R., Smith, R.B., and Lowry, A.R., 2009, Density and lithospheric strength models of the Yellowstone-Snake River Plain volcanic system from gravity and heat flow data: Journal of Volcanology and Geothermal Research, v. 188, no. 1-3, p. 108–127, doi: 10.1016/j.jvolgeores.2009.08.006.

de Silva, S.L., Mucek, A.E., Gregg, P.M., and Pratomo, I., 2015, Resurgent Toba - field, chronologic, and model constraints on time scales and mechanisms of resurgence at large calderas: Frontiers in Earth Science, v. 3, p. 1–17, doi: 10.3389/feart.2015.00025.

Dickinson, W.R., 2004, Evolution of the North American Cordillera: Annual Review of Earth and Planetary Sciences, v. 32, no. 1, p. 13–45, doi: 10.1146/annurev.earth.32.101802.120257.

Doherty, D.J., 1979b, Drilling data from exploration well 2-2A, NW1/4, Sec. 15, T. 5 N., R. 31 E., Idaho National Engineering Laboratory, Butte County, Idaho: U. S. Geological Survey Open-File Report, v. 79-851, p. 1.

Doherty, D., McBroome, L., and Kuntz, M., 1979, Preliminary geological interpretation and lithologic log of the exploratory geothermal test well (INEL-1): U. S. Geological Survey Open-File Report, v. 79-1248, p. 10.

Drew, D.L., Bindeman, I.N., Watts, K.E., Schmitt, A.K., Fu, B., and McCurry, M., 2013, Crustal-scale recycling in caldera complexes and rift zones along the Yellowstone hotspot track: O and Hf isotopic evidence in diverse zircons from voluminous rhyolites of the Picabo volcanic field, Idaho: Earth and Planetary Science Letters, v. 381, p. 63–77, doi: 10.1016/j.epsl.2013.08.007.

Ekren, E.B., McIntyre, D.H., and Bennett, E.H., 1984, High-temperature, large-volume, lavalike ash-flow tuffs without caldera in southwestern Idaho: U.S. Geological Survey Proffesional Paper, v. 1272, p. 82.

Ellis, B.S., Wolff, J. a., Boroughs, S., Mark, D.F., Starkel, W. a., and Bonnichsen, B., 2013, Rhyolitic volcanism of the central Snake River Plain: a review: Bulletin of Volcanology, v. 75, no. 8, p. 745, doi: 10.1007/s00445-013-0745-y.

Embree, G.F., Lowell, M.D., and Doherty, D.J., 1978, Drilling data from Sugar City exploration well, Madison County, Idaho: U. S. Geological Survey Open-File Report, v. 78-1095, p. 1.

Fishel, M.L., 1993, The geology of uplifted rocks on Big Southern Butte: implications for the stratigraphy and geochemistry of the eastern Snake River plain, Idaho: Idaho State University, 178 p.

Foster, D.A., Mueller, P.A., Mogk, D.W., Wooden, J.L., and Vogl, J.J., 2006, Proterozoic evolution of the western margin of the Wyoming craton: implications for the tectonic and magmatic evolution of the northern Rocky Mountains: Canadian Journal of Earth Sciences, v. 43, no. 10, p. 1601–1619, doi: 10.1139/e06-052.

Fouch, M.J., 2012, The Yellowstone Hotspot : Plume or Not ? Geology, , no. 5, p. 479–480, doi: 10.1016/j.

Foulger, G.R., Christiansen, R.L., and Anderson, D.L., 2015, The Yellowstone "hot spot" track results from migrating basin-range extension: Geological Society of America Special Paper, v. 514, p. SPE514–14, doi: 10.1130/2015.2514(14).

Gaschnig, R.M., Vervoort, J.D., Lewis, R.S., and Tikoff, B., 2011, Isotopic Evolution of the Idaho Batholith and Challis Intrusive Province, Northern US Cordillera: Journal of Petrology, v. 52, no. 12, p. 2397–2429, doi: 10.1093/petrology/egr050.

Geslin, J.K., Link, P.K., Riesterer, J.W., Kuntz, M.A., and Fanning, C.M., 2002, Pliocene and Quaternary stratigraphic architecture and drainage systems of the Big Lost Trough, northeastern Snake River Plain, Idaho: Geological Society of America Special Paper, v. 353, p. 11–26.

Geyer, A., and Martí, J., 2008, The new worldwide collapse caldera database (CCDB): A tool for studying and understanding caldera processes: Journal of Volcanology and Geothermal Research, v. 175, no. 3, p. 334–354, doi: 10.1016/j.jvolgeores.2008.03.017.

Greely, R., and King, J.S., 1977, Volcanism of the Eastern Snake River Plain, Idaho: A comparative planetary geology guidebook (R. Greely & J. S. King, Eds.): NASA, Washington, D.C.

Greensfelder, R.W., and Kovach, R.L., 1982, Shear wave velocities and crustal structure of the Eastern Snake River Plain, Idaho: Journal of Geophyscial Research, v. 87, no. B4, p. 2643–2653.

Gregg, P.M., De Silva, S.L., Grosfils, E.B., and Parmigiani, J.P., 2012, Catastrophic caldera-forming eruptions: Thermomechanics and implications for eruption triggering and maximum caldera dimensions on Earth: Journal of Volcanology and Geothermal Research, v. 241-242, p. 1–12, doi: 10.1016/j.jvolgeores.2012.06.009.

Hackett, W.R., and Smith, R.P., 1992, Quaternary volcanism, tectonics, and sedimentation in the Idaho National Engineering Laboratory area, *in* Wilson, J.R. ed., Field Guide to Geological Excursions in Utah and Adjacent Areas of Nevada, Idaho, and Wyoming, Utah Geological Survey Miscellaneous Publication 92-3, p. 1–18.

Holmes, A. a. J., Rodgers, D.W., and Hughes, S.S., 2008, Kinematic analysis of fractures in the Great Rift, Idaho: Implications for subsurface dike geometry, crustal extension, and magma dynamics: Journal of Geophysical Research, v. 113, no. B4, p. 1–15, doi: 10.1029/2006JB004782.

Hughes, S.S., Wetmore, P.H., and Casper, J.L., 2002, Evolution of Quaternary Tholeiitic Basalt Eruptive Centers on the Eastern Snake River Plain , Idaho, *in* Tectonic and Magmatic Evolution of the Snake River Plain Volcanic Province,.

Jackson, S.M., Carpenter, G.S., Smith, R.P., and Casper, J.L., 2006, Seismic reflection project near the southern terminations of the Lost River and Lemhi Faults , Eastern Snake River Plain , Idaho: Idaho National Laboratory Report, v. INL/EXT-06, no. October, p. 16.

Janecke, S.U., 1993a, Structures in segment boundary zones of the Lost River and Lemhi Faults, east central Idaho: Journal of Geophysical Research, v. 98, no. B9, p. 16,223–16,238.

Josten, N.E., and Smith, R.P., 1997, Gravity evidence for buried calderas beneath the eastern Snake River Plain: Geological Society of America Abstacts, v. 29, p. 365.

Kawakami, Y., Hoshi, H., and Yamaguchi, Y., 2007, Mechanism of caldera collapse and resurgence: Observations from the northern part of the Kumano Acidic Rocks, Kii peninsula, southwest Japan: Journal of Volcanology and Geothermal Research, v. 167, no. 1-4, p. 263–281, doi: 10.1016/j.jvolgeores.2007.02.003.

Kelbert, a., Egbert, G.D., and deGroot-Hedlin, C., 2012, Crust and upper mantle electrical conductivity beneath the Yellowstone Hotspot Track: Geology, v. 40, no. 5, p. 447–450, doi: 10.1130/G32655.1.

Kellogg, K.S., Harlan, S.S., Mehnert, H.H., Snee, L.W., Pierce, K.L., Hackett, W.R., and Rodgers, D.W., 1994, Major 10 . 2-Ma Rhyolitic Volcanism in the Eastern Snake River Plain , Idaho- Isotopic Age and Stratigraphic Setting of the Arbon Valley Tuff Member of the Starlight Formation. U. S. Geological Survey Bulletin, v. 2091, p. 18.

Kennedy, B., Wilcock, J., and Stix, J., 2012, Caldera resurgence during magma replenishment and rejuvenation at Valles and Lake City calderas: Bulletin of Volcanology, v. 74, no. 8, p. 1833–1847, doi: 10.1007/s00445-012-0641-x.

Knott, T., Branney, M.J., Christiansen, E.H., Reichow, M.K., McCurry, M.O., and Shervais, J.W., 2013, Drilling a "‌;super-volcano": volcanology of the proximal rhyolitic volcanic succession in the HOTSPOT deep drill hole, Idaho, Yellowstone hot-spot track: American Geophysical Union Abstract V13D-2649.

Konstantinou, A., and Strickland, A., 2012, Multistage Cenozoic extension of the Albion–Raft River–Grouse Creek metamorphic core complex: Geochronologic and stratigraphic constraints: Geosphere, v. 8, no. 6, p. 1429–1466.

Konstantinou, A., Valley, J.W., Strickland, A., Miller, E.L., Fisher, C., Vervoort, J., and Wooden, J.L., 2013, Geochemistry and geochronology of the Jim Sage volcanic suite, southern Idaho: Implications for Snake River Plain magmatism and its role in the history of Basin and Range extension: Geosphere, v. 9, no. 6, p. 1681–1703, doi: 10.1130/GES00948.1.

Konstantinou, A., Strickland, A., Miller, E., Vervoort, J., Fisher, C.M., Wooden, J., and Valley, J., 2013, Synextensional magmatism leading to crustal fl ow in the Albion – Raft River – Grouse Creek metamorphic core complex , northeastern Basin and Range: Tectonics, v. 32, p. 1–20, doi: 10.1002/tect.20085.

Kuntz, M.A., 1992, A model-based perspective of basaltic volcanism, eastern Snake River Plain, Idaho, *in* Link, P.K., Kuntz, M.A., and Platt, L.B. eds., Regional Geology of Eastern Idaho and Western Wyoming, Geological Society of America Memoir 179, p. 289–304.

Kuntz, M.A., Anderson, S.R., Champion, D.E., Lanphere, M.A., and Grunwald, D.J., 2002, Tension cracks, eruptive fissures, dikes, and faults related to late Pleistocene-Holocene basaltic volcanism and implications for the distribution of hydraulic conductivity in the eastern Snake River Plain, Idaho: Geological Society of America Special Paper, v. 353, p. 111–133.

Kuntz, M. a., Champion, D.E., Spiker, E.C., and Lefebvre, R.H., 1986b, Contrasting magma types and steady-state, volume-predictable, basaltic volcanism along the Great Rift, Idaho (USA).: Geological Society of America Bulletin, v. 97, no. 5, p. 579–594.

Kuntz, M.A., Covington, H.R., and Schorr, L.J., 1992, An overview of basaltic volcanism of the eastern Snake River Plain, Idaho, *in* Link, P.K., Kuntz, M.A., and Platt, L.B. eds., Geological Society of America Memoir, Geological Society of America, p. 227–267.

Kuntz, M.A., and Dalrymple, G.B., 1979, Geology, geochronology, and potential volcanic hazards in the Lava Ridge-Hells Half Acre area, eastern Snake River Plain, Idaho: U. S. Geological Survey Open-File Report, v. 79-1657, p. 66.

Kuntz, M.A., and Kork, J.O., 1978, Geology of the Arco-Big Southern Butte area, eastern Snake RiverPlain, and potential volcanic hazards to the radioactive waste management complex, and other waste storage and reactor facilities at the Idaho National Engineering Laboratory, Idaho: U. S. Geological Survey Open-File Report, v. 78-691, p. 77.

Kuntz, M.A., Skipp, B.A., Lanphere, M.A., Scott, W.E., Pierce, K.L., Dalrymple, G. B. Champion, D.E., Embree, G.F., Page, W.R., Morgan, L.A., Smith, R.P., Hackett, W.R., and Rodgers, D.W., 1994, Geologic map of the Idaho National Engineering Laboratory and adjoining areas, eastern Idaho: U. S. Geological Survey IMAP, v. 2330.

Leeman, W.P., Annen, C., and Dufek, J., 2008, Snake River Plain - Yellowstone silicic volcanism: implications for magma genesis and magma fluxes: Geological Society, London, Special Publications, v. 304, no. 1, p. 235–259, doi: 10.1144/SP304.12.

Leeman, W.P., Schutt, D.L., and Hughes, S.S., 2009, Thermal structure beneath the Snake River Plain: Implications for the Yellowstone hotspot: Journal of Volcanology and Geothermal Research, v. 188, no. 1-3, p. 57–67, doi: 10.1016/j.jvolgeores.2009.01.034.

Leeman, W.P., 1982, Evolved and Hybrid Lavas from the Snake River Plain, Idaho, *in* Bonnichsen, B. and Breckenridge, R.M. eds., Cenozoic Geology of Idaho, Idaho Bureau of Mines and Geology Bulletin 26, p. 193–202.

Liberty, L.M., Schmitt, D.R., and Shervais, J.W., 2015, Seismic imaging through the volcanic rocks of the Snake River Plain: insights from Project Hotspot: Geophysical Prospecting, v. 63, p. 919–936, doi: 10.1111/1365-2478.12277.

Link, P.K., and Janecke, S.U., 1999, Geology of East-Central Idaho: Geologic Roadlogs for the Big and Little Lost River, Lemhi, and Salmon River Valleys, *in* Hughes, S.S. and Thackray, G.D. eds., Guidebook to the Geology of Eastern Idaho, Idaho Museum of Natural History, p. 295–334.

Lipman, P.W., Zimmerer, M.J., and McIntosh, W.C., 2015, An ignimbrite caldera from the bottom up: Exhumed floor and fill of the resurgent Bonanza caldera, Southern Rocky Mountain volcanic field, Colorado: Geosphere, v. 11, p. GES01184.1, doi: 10.1130/GES01184.1.

Lipman, P.W., and McIntosh, W.C., 2008, Eruptive and noneruptive calderas, northeastern San Juan Mountains, Colorado: Where did the ignimbrites come from? Bulletin of the Geological Society of America, v. 120, p. 771–795, doi: 10.1130/B26330.1.

Lipman, P.W., 1997, Subsidence of ash-flow calderas: relation to caldera size and magma-chamber geometry: Bulletin of Volcanology, v. 59, no. 3, p. 198–218, doi: 10.1007/s004450050186.

Mabey, D.R., 1982, Geophysics and tectonics of the Snake River plain, Idaho: Bulletin - Idaho Bureau of Mines and Geology, v. 26, p. 139.

Mabey, D.R., 1978, Gravity and aeromagnetic anomalies in the Rexburg area of Eastern Idaho: U. S. Geological Survey Open-File Report, v. 78-382, p. 19.

McCurry, M., 2009, The Arbon Valley Tuff: A new look at a highly anomalous ignimbrite from the Yellowstone–Snake River Plain track: Geological Society of America Abstracts with Programs, v. 41, no. 6, p. 43.

McCurry, M., Hayden, K.P., Morse, L.H., and Mertzman, S., 2008, Genesis of post-hotspot, A-type rhyolite of the Eastern Snake River Plain volcanic field by extreme fractional crystallization of olivine tholeiite: Bulletin of Volcanology, v. 70, no. 3, p. 361–383, doi: 10.1007/s00445-007-0143-4.

McCurry, M., and Rodgers, D.W., 2009, Mass transfer along the Yellowstone hotspot track I: Petrologic constraints on the volume of mantle-derived magma: Journal of Volcanology and Geothermal Research, v. 188, no. 1-3, p. 86–98, doi: 10.1016/j.jvolgeores.2009.04.001.

McCurry, M., and Welhan, J., 2012, Do Magmatic-Related Geothermal Energy Resources Exist in Southeast Idaho ? GRC Transactions, v. 36, p. 699–707.

McBroome, L.A., Doherty, D.J., and Embree, G.F., 1981, Correlation of major Pliocene and Miocene ash-flow sheets, eastern Snake River plain, Idaho, *in* Montana Geological Society 1981 Field Conference and Symposium Guidebook to Southwest Montana, p. 323–330.

McQuarrie, N., and Rodgers, D.W., 1998, Subsidence of a volcanic basin by flexure and lower crustal flow: The eastern Snake River Plain, Idaho: Tectonics, v. 17, no. 2, p. 203, doi: 10.1029/97TC03762.

Moody, A., and Plummer, M. a, 2014, Implications of geology, structure and tectonic setting for heat extraction on the Eastern Snake River Plain: Proceedings, Thirty-Ninth Workshop on Geothermal Reservoir Engineering Stanford University, Stanford, California, February 24-26, 2014 SGP-TR-202, v. 2, no. SGP-TR-202, p. 1–9.

Morgan, L.A., 1988, Explosive rhyolitic volcanism on the Eastern Snake River Plain: University of Hawaii, 200 p.

Morgan, L.A., 1992, Stratigraphic relations and paleomagnetic and geochemical correlations of ignimbrites of the Heise volcanic field, eastern Snake River Plain, eastern Idaho and western Wyoming, *in* Link, P.K., Kuntz, M.A., and Platt, L.B. eds., Geological Society of America Memoir, Geological Society of America, p. 215–226.

Morgan, L. a., Doherty, D.J., and Leeman, W.P., 1984, Ignimbrites of the Eastern Snake River Plain: Evidence for major caldera-forming eruptions: Journal of Geophysical Research, v. 89, no. B10, p. 8665, doi: 10.1029/JB089iB10p08665.

Morgan, L. a., and McIntosh, W.C., 2005, Timing and development of the Heise volcanic field, Snake River Plain, Idaho, western USA: Geological Society of America Bulletin, v. 117, no. 3, p. 288, doi: 10.1130/B25519.1.

Morgan, L.A., Pierce, K.L., and Shanks, W.C.P., 2008, Track of the Yellowstone hotspot: Young and ongoing geologic processes from the Snake River Plain to the Yellowstone Plateau and Tetons, *in* Roaming the Rocky Mountains and Environs: Geological Field Trips: Geological Society of America Field Guide, p. 1–35.

Pankratz, L.W., and Ackermann, H.D., 1982, Structure along the northwest edge of the Snake River Plain interpreted from seismic refraction: Journal of Geophysical Research, v. 87, no. B4, p. 2676, doi: 10.1029/JB087iB04p02676.

Parsons, T., 1995, The Basin and Range Province, *in* K. Olsen ed., Continental Rifts: Evolution, Structure and Tectonics, Elsevier, New York, p. 277– 324,.

Parsons, T., Thompson, G.A., and Smith, R.P., 1998a, More than one way to stretch: a tectonic model for extension along the plume track of the Yellowstone hotspot and adjacent Basin and Range Province: Tectonics, v. 17, no. 2, p. 221, doi: 10.1029/98TC00463.

Payne, S.J., McCaffrey, R., King, R.W., and Kattenhorn, S. a., 2012, A new interpretation of deformation rates in the Snake River Plain and adjacent basin and range regions based on GPS measurements: Geophysical Journal International, v. 189, no. 1, p. 101–122, doi: 10.1111/j.1365-246X.2012.05370.x.

Peng, X., and Humphreys, E.D., 1998, Crustal velocity structure across the eastern Snake River Plain and the Yellowstone swell: Journal of Geophyscial Research, v. 103, p. 7171–7186.

Phillips, W.M., Szymanowski, D., and Ellis, B., 2014, Effect of poorly constrained caldera locations on ignimbrite volume estimates, Heise Volcanic Field, Eastern Snake River Plain, Idaho: Geological Society of America Abstracts with Programs, v. 46, no. 5, p. 94.

Pierce, K.L., and Morgan, L. a., 2009, Is the track of the Yellowstone hotspot driven by a deep mantle plume? — Review of volcanism, faulting, and uplift in light of new data: Journal of Volcanology and Geothermal Research, v. 188, no. 1-3, p. 1–25, doi: 10.1016/j.jvolgeores.2009.07.009.

Pierce, K.L., and Morgan, L.A. The track of the Yellowstone hot s1oot: Volcanism, faulting, and uplift: Geological Society of America Memoir, v. 179, p. 1–52.

Podgorney, R., Mccurry, M., Wood, T., Mcling, T., Ghassemi, A., Welhan, J., Mines, G., Plummer, M., Moore, J., Fairley, J., and Wood, R., 2013, Enhanced Geothermal System Potential for Sites on the Eastern Snake River Plain , Idaho: GRC Transactions, v. 37, p. 191–197.

Potter, K.E., 2014, The Kimama Core: A 6.4 Ma record of volcanism , sedimentation , and magma petrogenesis on the axial volcanic high , Snake River Plain , ID: Utah State University PhD Dissertation, 174 p.

Putirka, K.D., Kuntz, M. a., Unruh, D.M., and Vaid, N., 2009, Magma Evolution and Ascent at the Craters of the Moon and Neighboring Volcanic Fields, Southern Idaho, USA: Implications for the Evolution of Polygenetic and Monogenetic Volcanic Fields: Journal of Petrology, v. 50, no. 9, p. 1639–1665, doi: 10.1093/petrology/egp045.

Rodgers, D.W., Hackett, W.R., and Ore, H.T., 1990, Extension of the Yellowstone plateau, eastern Snake River Plain, and Owyhee plateau: v. Geology, no. 18, p. 1138–1141.

Rodgers, D.W., Ore, H.T., and Bobo, R.T., 2002, Extension and subsidence of the eastern Snake River Plain, Idaho: Tectonic and Magmatic Evoluiton of the Snake River Plain Volcanic Province, p. 121–155.

Schmandt, B., Dueker, K., Humphreys, E., and Hansen, S., 2012, Hot mantle upwelling across the 660 beneath Yellowstone: Earth and Planetary Science Letters, v. 331-332, p. 224–236, doi: 10.1016/j.epsl.2012.03.025.

Shervais, J.W., Schmitt, D.R., Nielson, D., Evans, J.P., Christiansen, E.H., Morgan, L., Pat Shanks, W.C., Prokopenko, A. a., Lachmar, T., Liberty, L.M., Blackwell, D.D., Glen, J.M., Champion, D., Potter, K.E., et al., 2013, First results from HOTSPOT: The Snake River plain scientific drilling project, Idaho, U.S.A.: Scientific Drilling, , no. 15, p. 36–45, doi: 10.2204/iodp.sd.15.06.2013.

Shervais, J.W., Vetter, S.K., and Hanan, B.B., 2006, Layered mafic sill complex beneath the eastern Snake River Plain: Evidence from cyclic geochemical variations in basalt: Geology, v. 34, no. 5, p. 365–368, doi: 10.1130/G22226.1.

Skipp, B., Snider, L.G., Janecke, S.U., and Kuntz, M. A, 2009, Geologic map of the Arco 30 x 60 minute quadrangle, Idaho: Idaho Geologic Survey Publication GM-47. doi: 10.1029/2003GC000661.

Smith, R.B., Jordan, M., Steinberger, B., Puskas, C.M., Farrell, J., Waite, G.P., Husen, S., Chang, W.-L., and O'Connell, R., 2009, Geodynamics of the Yellowstone hotspot and mantle plume: Seismic and GPS imaging, kinematics, and mantle flow: Journal of Volcanology and Geothermal Research, v. 188, no. 1-3, p. 26–56, doi: 10.1016/j.jvolgeores.2009.08.020.

Smith, R.B., and Braile, L.W., 1994, The Yellowstone hotspot: Journal of Volcanology and Geothermal Research, v. 61, p. 121–187.

Smith, R.L., and Bailey, R.A., 1968, Resurgent cauldrons: Geological Society of America Memoir, p. 613–662, doi: 10.1130/MEM116-p613.

Sparlin, M.A., and Braile, L.W., 1982, Crustal structure of the Eastern Snake River Plain determined from ray trace modeling of seismic refraction data: Journal of Geophyscial Research, v. 87, no. B4, p. 2619–2633.

Spear, D.B., and King, J.S., 1982, The geology of Big Southern Butte, Idaho, *in* Cenozoic Geology of Idaho, Idaho Bureau of Mines and Geology Bulletin 26, p. 395–403.

Spera, F.J., and Crisp, J.A., 1981, Eruption volume, periodicity, and caldera area: Relationships and inferences on development of compositional zonation in silicic magma chambers: Journal of Volcanology and Geothermal Research, v. 11, p. 169–187.

Strickland, a., Miller, E.L., Wooden, J.L., Kozdon, R., and Valley, J.W., 2011, Syn-extensional plutonism and peak metamorphism in the Albion-Raft River-Grouse Creek metamorphic core complex: American Journal of Science, v. 311, no. 4, p. 261–314, doi: 10.2475/04.2011.01.

Strickland, A., Miller, E.L., and Wooden, J.L., 2011, The Timing of Tertiary Metamorphism and Deformation in the Albion–Raft River–Grouse Creek Metamorphic Core Complex, Utah and Idaho: The Journal of Geology, v. 119, no. 2, p. 185–206, doi: 10.1086/658294.

Szymanowski, D., Ellis, B.S., Bachmann, O., Guillong, M., and Phillips, W.M., 2015, Bridging basalts and rhyolites in the Yellowstone–Snake River Plain volcanic province: The elusive intermediate step: Earth and Planetary Science Letters, v. 415, p. 80–89, doi: 10.1016/j.epsl.2015.01.041.

Vogl, J.J., Min, K., Carmenate, a., Foster, D. a., and Marsellos, a., 2014, Miocene regional hotspot-related uplift, exhumation, and extension north of the Snake River Plain: Evidence from apatite (U-Th)/He thermochronology: Lithosphere, v. 6, no. 2, p. 108–123, doi: 10.1130/L308.1.

Wagner, L.S., Fouch, M.J., James, D.E., and Hanson-Hedgecock, S., 2012, Crust and upper mantle structure beneath the Pacific Northwest from joint inversions of ambient noise and earthquake data: Geochemistry, Geophysics, Geosystems, v. 13, no. 12, p. n/a–n/a, doi: 10.1029/2012GC004353.

Walker, G.P.L., 1984, Downsag calderas, ring faults, caldera sizes, and incremental caldera growth: Journal of Geophysical Research, v. 89, no. B10, p. 8407–8416, doi: 10.1029/JB089iB10p08407.

Watts, K.E., Bindeman, I.N., and Schmitt, A.K., 2011, Large-volume rhyolite genesis in caldera complexes of the Snake River Plain: Insights from the Kilgore Tuff of the Heise volcanic field, Idaho, with comparison to Yellowstone and Bruneau-Jarbidge rhyolites: Journal of Petrology, v. 52, no. 5, p. 857–890, doi: 10.1093/petrology/egr005.

Wetmore, P.H., Hughes, S.S., Connor, L., and Caplinger, M., 2009, Spatial distribution of eruptive centers about the Idaho National Laboratory, *in* Connor, C.B., Chapman, N.A., and Connor, L.J. eds., Volcanic and Tectonic Assessment for Nuclear Facilities, Cambridge, UK, Cambridge University Press, p. 23.

Whitaker, M.L., Nekvasil, H., Lindsley, D.H., and McCurry, M., 2008, Can crystallization of olivine tholeiite give rise to potassic rhyolites? - An experimental investigation: Bulletin of Volcanology, v. 70, p. 417–434, doi: 10.1007/s00445-007-0146-1.

Willcock, M. a W., Cas, R. a F., Giordano, G., and Morelli, C., 2013, The eruption, pyroclastic flow behaviour, and caldera in-filling processes of the extremely large volume (>1290km3), intra- to extra-caldera, Permian Ora (Ignimbrite) Formation, Southern Alps, Italy: Journal of Volcanology and Geothermal Research, v. 265, p. 102–126, doi: 10.1016/j.jvolgeores.2013.08.012.

Wohletz, K., and Heiken, G., 1992, Volcanology and geothermal energy: University of California Press, Berkeley, California.

Wu, D., and Bruhn, R.L., 1994, Structural and rupture characteristics of the southern Lost River Fault Zone, Idaho:.

Yonkee, W. a., Dehler, C.D., Link, P.K., Balgord, E. a., Keeley, J. a., Hayes, D.S., Wells, M.L., Fanning, C.M., and Johnston, S.M., 2014, Tectono-stratigraphic framework of Neoproterozoic to Cambrian strata, west-central U.S.: Protracted rifting, glaciation, and evolution of the North American Cordilleran margin: Earth-Science Reviews, v. 136, p. 59–95, doi: 10.1016/j.earscirev.2014.05.004.

Yuan, H., Dueker, K., and Stachnik, J., 2010, Crustal structure and thickness along the Yellowstone hot spot track: Evidence for lower crustal outflow from beneath the eastern Snake River Plain: Geochemistry, Geophysics, Geosystems, v. 11, no. 3, doi: 10.1029/2009GC002787.

Zhdanov, M.S., Gribenko, A., Čuma, M., and Green, M., 2012, Geoelectrical Structure of the Lithosphere and Asthenosphere beneath the Northwestern United States: Geology & Geosciences, v. 1, no. 2, p. 1–6, doi: 10.4172/jgg.1000106.

Zhdanov, M.S., Smith, R.B., Gribenko, A., Cuma, M., and Green, M., 2011, Three-dimensional inversion of large-scale EarthScope magnetotelluric data based on the integral equation method: Geoelectrical imaging of the Yellowstone conductive mantle plume: Geophysical Research Letters, v. 38, no. 8, p. n/a–n/a, doi: 10.1029/2011GL046953.

Zohdy, A.A.R., and Stanley, W.D., 1973, Preliminary interpretation of electrical sounding curves obtained across the Snake River Plain from Blackfoot to Arco, Idaho: U. S. Geological Survey Open-File Report, v. 73-370.

Appendix B

Rock Physics Modeling for the Potential FORGE Site on the Eastern Snake River Plain, Idaho

PROCEEDINGS, 41st Workshop on Geothermal Reservoir Engineering
Stanford University, Stanford, California, February 22-24, 2016
SGP-TR-209

Rock Physics Modeling for the Potential FORGE Site on the Eastern Snake River Plain, Idaho

Dario Grana[1*], Sumit Verma[1], Robert Podgorney[2]

[1] Department of Geology and Geophysics, University of Wyoming, Laramie, WY 82070

[2] Idaho National Laboratory, Idaho Falls, ID 83415

[*] Corresponding author: dgrana@uwyo.edu

Keywords: Rock physics, Seismic modeling, Snake River Plane

ABSTRACT

Rock physics models allow establishing a physical-mathematical relation between rock and fluid properties and geophysical attributes. In this study, we propose to apply rock physics models to a geophysical dataset measured at two well locations near the proposed Snake River Plain FORGE site in eastern Idaho. The potential target is a rhyolite layer, which occurs between 2,000 and 3,000 m. The available data include two sets of sonic and petrophysical well logs at two well locations, which are approximately 6 km apart. The goal of this study is to calibrate a physical model to link reservoir properties (porosity, lithology, saturation) and reservoir conditions (pressure and temperature) with geophysical attributes (velocities, density, and resistivity). This multi-physics model is calibrated at the well locations, but can be extended to the entire site if geophysical data are available. As a feasibility study to determine the value of information of 3D geophysical surveys we plan to build synthetic 2D sections through the two existing wells by interpolating well log data using geostatistical techniques such as kriging and sequential Gaussian simulations and compute the predicted seismic, electromagnetic and gravimetric responses of the model. By combining rock physics models with mathematical inverse theory, we plan to perform a sensitivity analysis on the resolution and noise level of the geophysical survey in order to determine the minimum requirements of the geophysical data acquisition to improve the reservoir description. We will also compare the new results with a previous study based on 2D refraction seismic, resistivity and gravity fields.

1. INTRODUCTION

Rock physics modeling is the discipline that studies physical-mathematical relations between geophysical measurements, such as elastic properties of seismic waves, and rock and fluid properties, such as porosity, lithology and fluid saturations. Geophysical measurements do not contain direct measurements of the reservoir properties. Indeed seismic data contain information about the compressional and shear wave velocity; electromagnetic surveys include resistivity measurements; and gravity surveys provide density data. Therefore, in hydrocarbon reservoir modeling, these sets of relations are essential to estimate rock and fluid properties from geophysical attributes and build 3-dimentional models for fluid flow simulations and predictions. Similarly, in geothermal reservoirs, we can apply rock physics models to build an initial static model for geothermal dynamic simulations.

Rock physics literature includes several models to estimate elastic and electrical properties from rock and fluid measurements (Mavko et al., 2009; Dvorkin et al., 2014). For example, given a set of rock physics relations, we can estimate the velocity of compressional and shear waves given the porosity, lithological content and fluid saturation of the porous rock at reservoir conditions. Similarly, we can also estimate the resistivity and density of the porous rock. Rock physics provides several empirical and physically-derived relations to estimate the link between porosity and velocity, porosity and permeability, saturation and resistivity for a number of lithologies and fluid mixtures. Datasets acquired in hydrocarbon reservoirs show common trends between these properties. Once a relation between geophysical attributes and rock and fluid properties is established, we can then quantitatively interpret geophysical measurements and build 3-dimentional models. Rock physics models can be also used for feasibility studies for acquisition of geophysical datasets. The rock physics model can reveal which geophysical survey is the most sensitive to rock and fluid properties, and determine which geophysical dataset should be acquired in the field.

In general, a rock physics model includes multiple relations. When we create a poroelastic model for porous rocks, we first model the solid and fluid phase independently and then we model the poroelastic properties of the saturated rock as a mixture of the solid and fluid phases. Each phase is modeled as an effective medium. Mixing laws are available in literature, such as Voigt and Reuss averages and Hashin Shtrikmann bounds (Mavko et al., 2009; Dvorkin et al., 2014). To combine the two phases, the model for the porosity effect depends on the rock type under study. Empirical relations such as Han's multilinear regression and Wyllie and Raymer's regressions can be applied (Mavko et al., 2009; Dvorkin et al., 2014). However, these relations must be fitted to real data in order to be extended to the entire dataset. Among the physical relations used to describe the porosity effect, two main categories of models can be distinguished: granular media models and inclusion models (Mavko et al., 2009; Dvorkin et al., 2014). In granular media models, we assume that the porous rock is a random pack of spherical grains and we try to mathematically approximate the compressibility of the rock. In inclusion models, we approximate the geometrical shape of the pores using spheres or ellipsoids and we estimate the rock compressibility. The fluid effect is generally included in the model through Gassmann's equations (Mavko et al., 2009; Dvorkin et al., 2014).

In this study, we aim to build a rock physics model for a geothermal reservoir and compute the potential seismic response for different reservoir scenarios. In this work, we focus on elastic properties and seismic data because of the higher resolution of seismic compared to electromagnetic and gravity data and the potential ability of seismic modeling and inversion to monitor the dynamic changes in the

reservoir through time. However, the workflow can be extended to other geophysical measurements such as electromagnetic and gravity surveys if a suitable rock physics model can be calibrated at the well location. Seismic attributes can be measured at the well location and can be derived from 3-dimentional seismic data through seismic inverse modeling methods (Aki and Richards, 1980 and Yilmaz, 2001).

The dataset under study is the Potential FORGE Site on the Eastern Snake River Plain, Idaho. The Snake River is located along the track of the Yellowstone Hot Spot. The site is characterized by high heat flow and subsurface temperatures, a prolific regional aquifer system, and favorable regional stress and seismic conditions (Podgorney et al., 2016; Plummer et al., 2016; and Neupane et al., 2016). The study was identified by a recent MIT study as one of the top locations for Enhanced Geothermal Systems in the United States (Podgorney et al., 2016). In this work, we show the preliminary geophysical study including the rock physics model calibration and seismic feasibility study. For the model calibration, w used the data measured at the INEL 1 well, 6 km away from the site.

2. METHOD AND APPLICATION

In this section, we present the rock physics analysis at the INEL 1 location and use the so-obtained results as a feasibility study for seismic acquisition and modeling. The goal of this work is to establish a set of physical-mathematical relations between geophysical measurements and rock and fluid properties. These relations can be then used to build 3-dimentional reservoir models once geophysical data are acquired. Indeed, these models allow the identification of lithologies and the estimation of porosity and potentially fluid saturations from seismic, electromagnetic and gravity data.

2.1 Dataset

The available set of well logs at the INEL 1 location includes gamma ray, density, sonic, neutron porosity and resistivity (Figure 1). A facies classification has been derived according to the stratigraphic profile presented in Doherty et al. 1979 (for further details also refer to McCurry and Rodgers, 2009, and Drew et al., 2013). A preliminary data processing and well log analysis has been performed on the data to eliminate biased measurements and reconstruct sections of the logs in which data were missing. In particular, a local multilinear regression has been used to reconstruct part of the density log. In the interval of interest, between 2000 and 3000 m, all the logs were measured correctly, and the caliper log does not show relevant anomalies in the borehole. Doherty et al. (1979) determined seven sedimentological facies, based on well cuttings and cores. According to regional geological models and stratigraphy, we simplified the model to five main lithological facies (Figure 1): a shallow section basalt interlayered with sand and silt layers; a deeper basalt layer consisting of welded tuff interlayered with thin layers of tuffaceous sand and air fall ash; and a dense, recrystallized, hydrothermally altered rhyodacite.

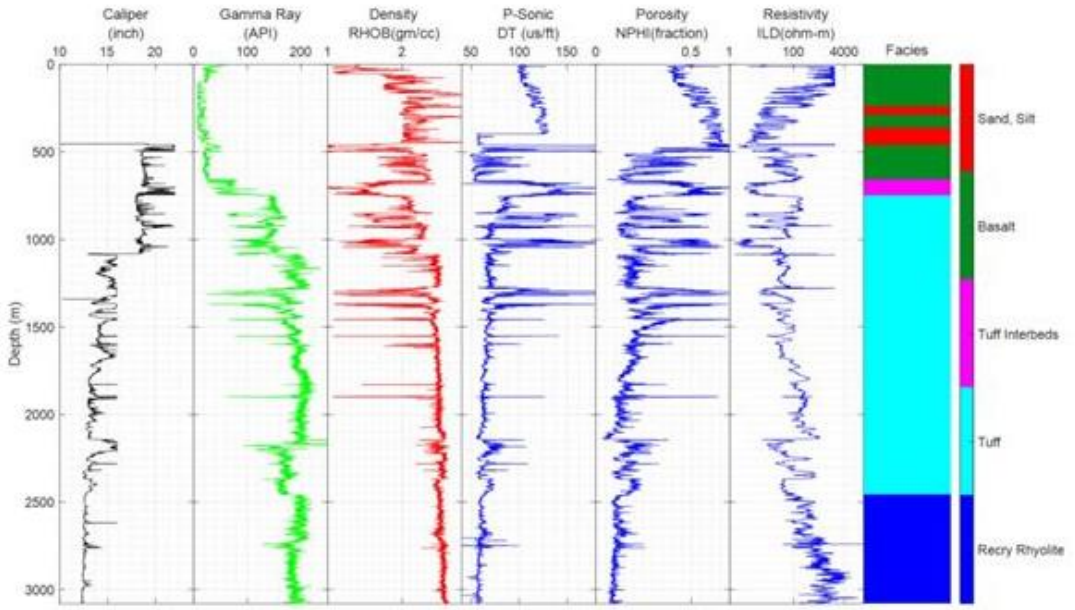

Figure 1: Well logs dataset at well INEL 1; from left to right: caliper, gamma ray, bulk density, sonic log, neutron porosity, deep induction log resistivity. A facies profile is shown in the last plot (the classification was derived and modified after Doherty et al., 1979).

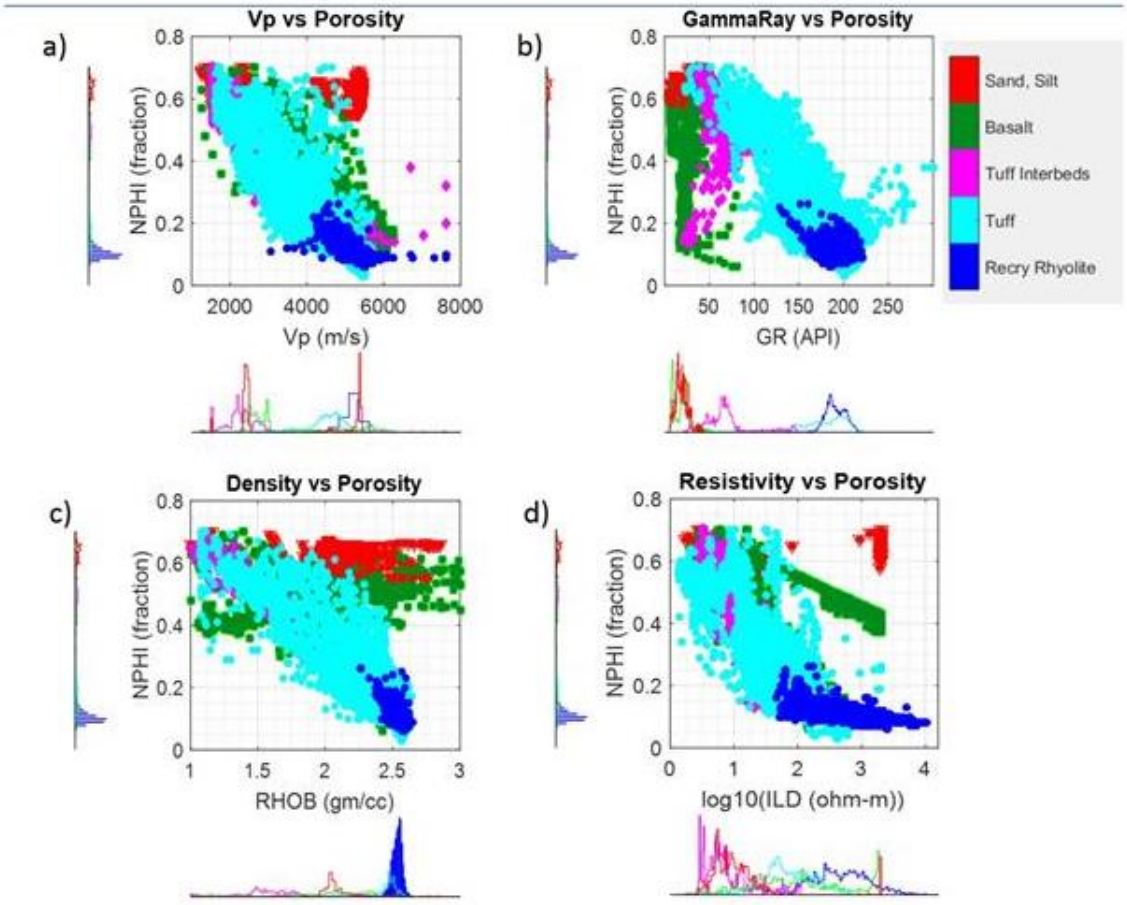

Figure 2: Crossplots between elastic and petrophysical properties versus porosity: (a) P-wave velocity, (b) Gamma ray, (c) Density and (d) Resistivity versus neutron porosity.

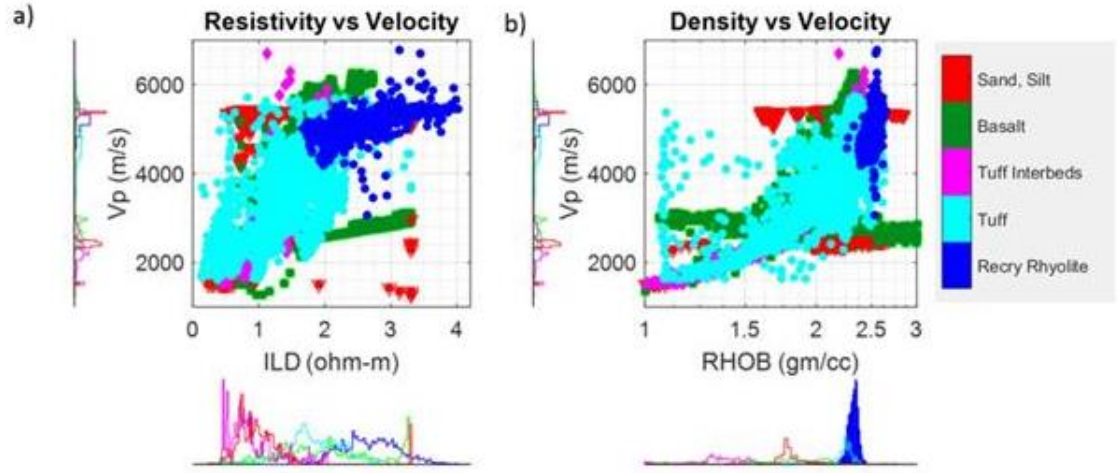

Figure 3: Crossplots in the joint elastic and electrical domains: (a) P-wave velocity versus resistivity and (b) P-wave velocity versus density.

3

According to the sonic log (Figure 1), the elastic responses of tuff and rhyolite show similar features. However, in a multivariate analysis the rhyolite layer can be discriminated from the tuff layer. In Figures 2 and 3, we show rock physics crossplots of well logs. In Figure 2 (top left), we show the relation between porosity and P-wave velocity. Although the well log data are noisy, the absolute value of the linear correlation between porosity and velocity is generally high. Porosity and velocity are anti-correlated in each facies. The relation is approximately linear in tuff and rhyolite; however, due to the lower porosity, rhyolite is distinguishable in this petro-elastic domain. The resolution of seismic data is lower than the resolution of well logs; however, if the linear relation between porosity and velocity is still valid at the seismic scale, we can estimate the porosity in the rhyolite layer from seismic attributes. A linear relation is observable also in the petrophysical domain porosity versus gamma ray (Figure 2, top right). The linear correlation is negative. Overall, the higher is the gamma ray, the lower is the neutron porosity. Rhyolite is characterized by high gamma ray and low porosity. Tuffaceous sand interbeds have a lower range of gamma ray compared to tuff. Because gamma ray and density are highly correlated, we expect the neutron porosity and density to be negatively correlated as well. Indeed the higher is the neutron porosity, the lower is the density (Figure 2, bottom left). In Figure 2 (bottom right), we show the relation between porosity and resistivity. Although there are several values in the plot that do not follow any trend and could be considered outliers due inaccurate measurements or mud effect, we see an exponential relation between porosity and resistivity. In particular, even if the porosity is low in the rhyolite, the resistivity is relatively high. This crossplot suggests that we could obtain a good lithological discrimination in the joint elastic-electric domain by combining the results of seismic inversion (i.e. elastic attributes such as velocity and density) and results of the electromagnetic inversion (i.e. resistivity). An additional constrain can be added if gravity data are available, to better determine the density model. In Figure 3, we analyze the joint elastic and electrical domain. The crossplot between P-wave velocity and resistivity shows a good discrimination between tuff and rhyolite; however, we point out that the resolution of the resistivity model that can be achieved from electromagnetic data is lower than the seismic resolution. The lower resolution could then affect the discriminability of the different facies. If the seismic acquisition includes large acquisition angles (or if gravity data are available), density could be estimated from seismic data. In Figure 3, we show that rhyolite can be discriminated in the acoustic-elastic domain as well.

In order to calibrate and apply a rock physics model to well log data, we preliminary filtered the well log data to eliminate noise and outliers. The filtered data are shown in Figure 4. A facies classification has been performed on filtered data based on a statistical algorithm, namely the expectation and maximization algorithm (Hastie et al., 2009). The statistical classification is consistent with the stratigraphic profile shown in Figure 1. However, rhyolite is over-predicted within the tuff layer; whereas the interbedded sand and silt layers are not identified. This classification can be potentially extended to the entire reservoir model if geophysical measurements are available. The resolution of the filtered logs is still higher than the seismic resolution; therefore, some of the thin layers might not be resolved by geophysical data.

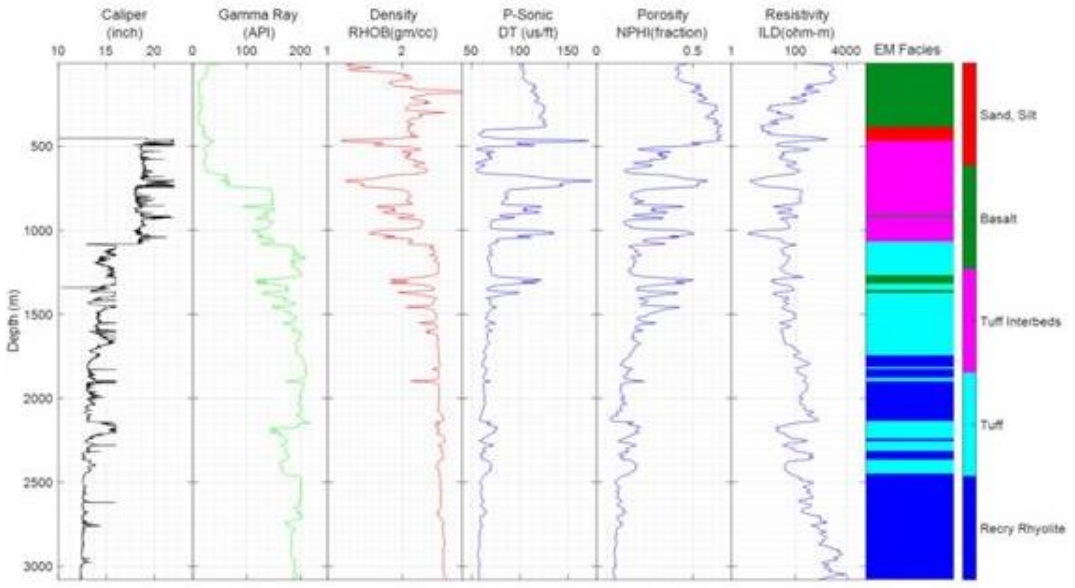

Figure 4: Filtered well logs from well INEL 1; from left to right: caliper, gamma ray, bulk density, sonic log, neutron porosity, deep induction log resistivity. A facies profile obtained using the expectation-maximization algorithm is shown in the last plot.

2.2 Rock physics model

In this section, we estimate a set of relations to link elastic and petrophysical parameters. Because rhyolite samples are not very common in hydrocarbon reservoir models, a limited number of measurements and physical-mathematical models are available in literature. In this study, we tested three different models: Nur's critical porosity, Raymers's equation, and the stiff sand model heuristically extended to rhyolite. For a complete description of these models, we refer the reader to Mavko et al. (2009). We applied these models to estimate the elastic moduli (bulk and shear moduli) of the dry rock in the tuff and rhyolite intervals. These models require the knowledge of the elastic properties of the solid rock. Due to the lack of elastic measurements on core samples, we tested several values and chose the optimal parameters based on the best fit between rock physics model predictions and measured data.

For this study, we selected the Nur's critical porosity model, although the other models provided consistent results. The fluid is assumed to be water in the entire interval of interest. The effect of the fluid on elastic properties can be described at the seismic scale by Gassmann's equation (Mavko et al., 2009). This model allows us to compute the bulk modulus of the saturated rock given its porosity, the bulk modulus of the solid phase, the bulk modulus of the dry rock, and the bulk modulus of the fluid. The shear modulus of the saturated rock is assumed to be the same as the shear modulus of the dry rock.

Nur's critical porosity model approximates the behavior of the dry rock with linear relations respect to porosity ϕ to compute the dry-rock elastic moduli K_{dry} and G_{dry}:

$$K_{dry} = K_{mat}\left(1 - \frac{\phi}{\phi_c}\right)$$
$$G_{dry} = G_{mat}\left(1 - \frac{\phi}{\phi_c}\right), \quad (1)$$

where ϕ_c is the critical porosity of the rock (assumed to be equal to 0.6 in our study) and K_{mat} and G_{mat} are the elastic moduli of the solid phase.

The fluid effect is introduced by combining dry rock properties in Equation 1 with the fluid properties, to obtain the saturated rock elastic moduli K_{sat} and G_{sat} through Gassmann's equations:

$$K_{sat} = K_{dry} + \frac{\left(1 - \frac{K_{dry}}{K_{mat}}\right)^2}{\frac{\phi}{K_{fl}} + \frac{(1-\phi)}{K_{mat}} - \frac{K_{dry}}{K_{mat}^2}}$$
$$G_{sat} = G_{dry}, \quad (2)$$

where K_{fl} is the bulk modulus of the fluid, which in our application is assumed to be water with bulk modulus of 2.25 GPa.

We applied the model in Equations 1 and 2 to the set of filtered well logs (Figure 4) to predict the elastic response of the reservoir. The predicted model is shown in Figure 5. One of the limitations of empirical rock physics models is the limited capability to predict S-wave velocity if well log data are not available for the calibration of the shear wave model. If S-wave velocity is required for the quantitative seismic interpretation study, a more reliable prediction could be obtained using the stiff sand model (Dvorkin et al., 2014).

Grana et al.

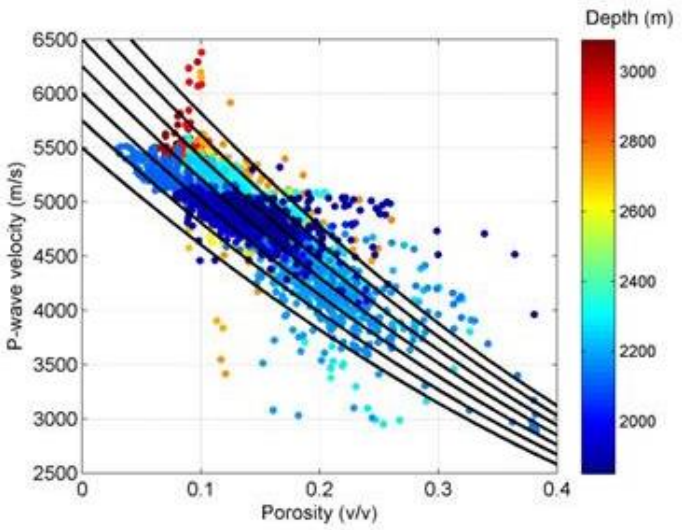

Figure 5: Rock physics model for predicting P-wave velocity as a function of porosity. Colored dots represent the well log measurements (color coded by depth), whereas the black curves show the rock physics model for several values of bulk modulus of the solid phase.

The stiff sand model (Dvorkin et al., 2014) is based on the modified Hashin–Shtrikman bound. The model combines the elastic moduli of the solid phase (rhyolite in our case) and Hertz-Mindlin moduli at the critical porosity ϕ_c. The Hertz-Mindlin equations allows us to compute the elastic moduli as follows:

$$K_{HM} = \sqrt[3]{\frac{n^2(1-\phi_c)^2 G_{mat}^2}{18\pi^2(1-\nu)^2}P}$$
$$G_{HM} = \frac{5-4\nu}{5(2-\nu)}\sqrt[3]{\frac{3n^2(1-\phi_c)^2 G_{mat}^2}{2\pi^2(1-\nu)^2}P}, \quad (3)$$

where P is the effective pressure, n is the average number of contacts per grain and ν is the Poisson ratio.

For effective porosity values between zero and the critical porosity, the stiff sand model connects the elastic moduli of the solid phase to the Hertz-Mindlin moduli of the dry rock at porosity ϕ_c, by interpolating the two end members at the intermediate porosity values through the modified Hashin-Shtrikman upper bound:

$$K_{dry} = \left(\frac{\frac{\phi}{\phi_c}}{K_{HM}+\frac{4}{3}G_{mat}} + \frac{1-\frac{\phi}{\phi_c}}{K_{mat}+\frac{4}{3}G_{mat}}\right)^{-1} - \frac{4}{3}G_{mat}$$
$$G_{dry} = \left(\frac{\frac{\phi}{\phi_c}}{G_{HM}+\frac{1}{6}\xi G_{mat}} + \frac{1-\frac{\phi}{\phi_c}}{G_{mat}+\frac{1}{6}\xi G_{mat}}\right)^{-1} - \frac{1}{6}\xi G_{mat}, \quad \xi = \frac{9K_{mat}+8G_{mat}}{K_{mat}+2G_{mat}} \quad (4)$$

We point out that the above-mentioned rock physics models do not include a geometrical description of the pore shape and treat the pore space as an effective medium. Furthermore, the measured data do not provide any information about the potential fracture system. A more accurate prediction could be obtained by integrating geomechanical measurements such as crack density and orientation in the rock physics model. Geomechanical analysis of the reservoir rocks are presented in Bakshi and Ghassemi (2016).

2.3 Seismic model and feasibility study

In this section, we apply a linearized seismic forward model to compute the seismic response of the reservoir layer and the sealing layer above it. If the elastic properties of the upper and lower layers are known, then the seismic response can be computed as a convolution of a wavelet and the reflection coefficients of the layer interface. The exact expression of the reflection coefficients can be computed using Zoeppritz equations (Aki and Richards, 1980); however, in this application, we assume that the incident angle is smaller than 45 degrees and the contrast of the elastic properties between the upper and lower layer is small, in order to apply a linearized approximation of Zoeppritz equations for weak contrasts. We use a three term approximation, namely Aki-Richards equation (Aki and Richards, 1980). In this synthetic example, we assume a Ricker wavelet with dominant frequency of 30 Hz. The predicted seismic response is shown in Figure 6 (left). A sensitivity study on the parameters affecting the quality of seismic data has been performed to verify the applicability of a seismic inversion approach to estimate the elastic properties in the reservoir and potentially the petrophysical parameters. The accuracy of the inversion results depend on the signal to noise ratio of the seismic dataset, the dominant frequency of the wavelet, the number of available angle stacks and the maximum angle. In particular, the estimation of density from seismic data requires a large incident angle in order to obtain accurate results.

The synthetic study has been performed using the petroelastic properties at reservoir conditions. The aim of the second part of the study is to verify the feasibility of reservoir monitoring through time-lapse seismic surveys. For this reason, we mimic a potential production scenario where reservoir water is replaced by steam. The elastic response has been computed using Gassmann's equations (Equation 2). In this example, we assume that porosity does not change during production. This assumption is conservative and aims to study the fluid effect only. If porosity increases due to hydraulic fracturing, the fluid effect on seismic variations will be more significant. The seismic response at the well location in the new reservoir scenario is shown in Figure 6 (mid plot). It is important to notice that we do not only observe a change in seismic amplitudes but also in the travel time. However, in order to compute the difference between the two seismic datasets, we must apply a time-shift correction using a warping technique (Figure 6, right plot). The difference in the two datasets can then be used for quantitative interpretation of time-lapse seismic data and reservoir monitoring. In this dataset, the velocity in rhyolite filled by steam decreases compared to the velocity in rhyolite filled by water due to the larger compressibility of steam compared to water.

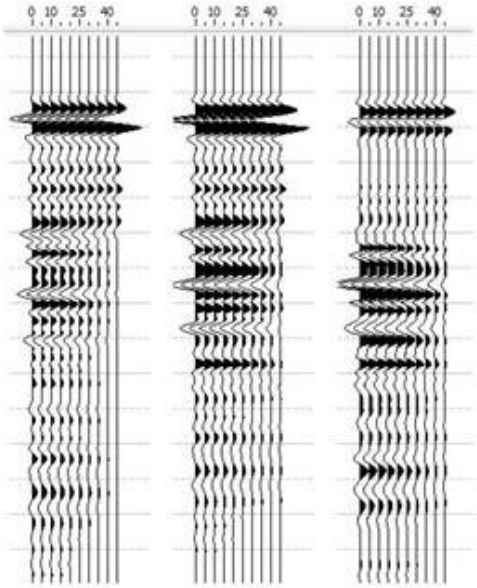

Figure 6: Synthetic seismic dataset between 2,000 and 3,000 meters. The left plot shows synthetic seismic at reservoir conditions; the mid plot shows synthetic seismic in steam conditions (same porosity as reservoir conditions). The seismic dataset in the mid plot has been corrected for time-shift to make it comparable to the left plot. Seismic differences (after time-shift correction) are shown in the right plot.

The feasibility study shows that seismic data can be used to constrain a 3D reservoir model of petrophysical properties, such as porosity, as well as to monitor saturation changes in the reservoir through time-lapse surveys. Electromagnetic and gravity surveys can be included in the reservoir characterization workflow; however, the resolution of these datasets is generally lower than the resolution of seismic data. For the characterization of the static reservoir model, seismic data should provide the most reliable information as long is the signal to noise ratio is large enough. A seismic dataset has been acquired in the 80s (see Sparlin et al., 1982 and Pankratz and Ackermann, 1982). An interpreted 2D section is shown in Figure 7 (left plot). However, this dataset only contains refraction seismic data. Therefore, the main interface between tuff and rhyolite cannot be interpreted from the data, due to the negative reflectivity at the interface. Gravity and resistivity data are also available. Sparlin et al. (1982) and Pankratz and Ackermann (1982) show an interpreted gravity section to estimate density (Figure 7, right plot). The integrated interpretation is based on a linear relation between velocity and density, which is confirmed by the well log data at INEL 1 location (Figure 3, right plot). For reservoir monitoring, both gravity and electromagnetic data could be used to estimate the spatial distribution of water and steam; however, a feasibility study prior to data acquisition is required to investigate the limitations due to data resolution.

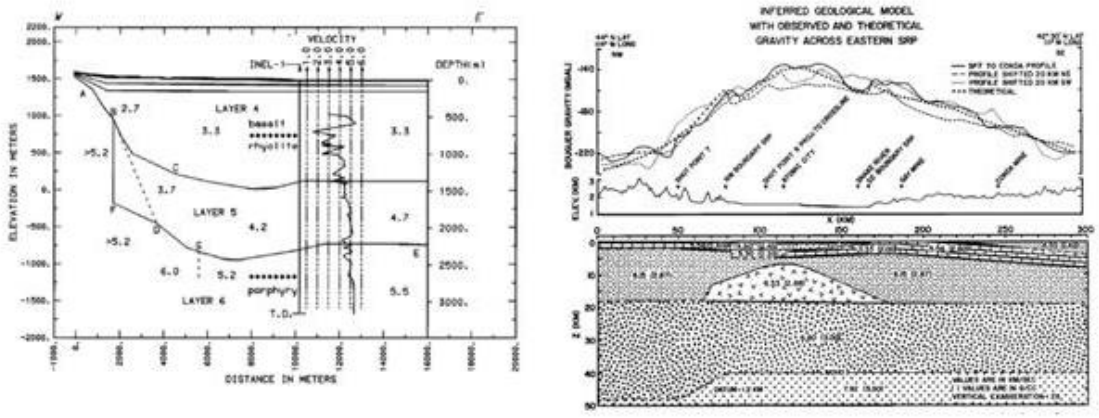

Figure 7: Interpretation of refraction seismic data (left plot) and gravity data (right plot) from Sparlin et al. (1982) and Pankratz and Ackermann (1982).

3. CONCLUSIONS

In this work, we presented a reservoir modeling workflow aimed to quantitatively interpret well log and surface geophysical measurements. The workflow includes a rock physics model to link the rock and fluid properties to elastic attributes such as seismic velocity and density; whereas, the seismic modeling includes a convolutional model and a linearized approximation of the reflection coefficient model to estimate the seismic signature of the reservoir rocks. This forward model is calibrated at the well location and can be integrated in an inversion workflow to estimate rock and fluid properties from geophysical measurements, such as surface seismic and eventually electromagnetic and gravity data. The study also aims to assess the ability of time-lapse seismic data to monitor dynamic changes in the reservoir fluids. In particular, time-lapse seismic differences can be used to estimate the spatial distribution of water and steam at different time steps of the production process.

REFERENCES

Aki, K., and Richards, P. G.: Quantitative seismology: *W. H. Freeman & Co* (1980).

Bakshi, R., and Ghassemi, A.: Geomechanical Characterization of Rock Core from the Proposed FORGE Laboratory on the Eastern Snake River Plain, Idaho: 41st workshop on Geothermal Reservoir Engineering, Stanford University, Stanford, CA (2016).

Doherty, D.J., McBroome, L.A., and Kuntz, M.: Preliminary geological interpretation and lithologic log of the exploratory geothermal test well (INEL-1), Idaho National Engineering Laboratory: *U.S. Geological Survey*, **9**, Open File Report, (1979), 79–1248.

Drew, D.L, Bindeman, I.N., Watts, K.E., Schmitt, A.K., Fu, B. and McCurry, M.: Crustal-scale recycling in caldera complexed and rift zones along the Yellowstone hot spot track: O and Hf isotopic evidence in diverse zircons from voluminous rhyolites of the Picabo volcanic field, Idaho: *Earth and Planetary Science Letters*, **381**, (2013), 63–77.

Dvorkin, J., Gutierrez, M., and Grana, D.: Seismic reflections of rock properties: *Cambridge University Press* (2014).

Hastie, T., Tibshirani, R., and Friedman, J.: The elements of statistical learning: *Springer* (2009).

Mavko, G., Mukerji, T., and Dvorkin, J.: The rock physics handbook: *Cambridge University Press* (2009).

McCurry, M., and Rodgers, D.W.: Mass transfer along the Yellowstone hotspot track I: Petrologic constraints on the volume of mantle-derived magma: *Journal of Volcanology and Geothermal Research*, **188**, (2009), 86–98

Neupane, G., Mattson, E.D., Cannon, C.J., Atkinson, T.A., Mcling, T.L., Wood, T.R., Dobson, P.F., and Conrad M.E.: Potential Hydrothermal Resource Temperatures in the Eastern Snake River Plain, Idaho: Plummer, M., Palmer, C.D., Mcling, T., and Sondrup A.J.: Modeling Heat Flow in the Eastern Snake River Plain Aquifer: 41st workshop on Geothermal Reservoir Engineering, Stanford University, Stanford, CA (2016).

Pankratz, L.W., and Ackermann, H.D.: Structure along the northwest edge of the Snake River Plain interpreted from seismic refraction: *Journal of Geophysical Research: Solid Earth*, **87**, (B4), (1982), 2676-2682.

Plummer, M., Palmer, C.D., Mcling, T., and Sondrup A.J.: Modeling Heat Flow in the Eastern Snake River Plain Aquifer: 41st workshop on Geothermal Reservoir Engineering, Stanford University, Stanford, CA (2016).

Podgorney R., Snyder, N., and Roy, M.: A Snake River Plain Field Laboratory for Enhanced Geothermal Systems: an Overview of the Snake River Geothermal Consortium's Proposed FORGE Approach and Site: 41st workshop on Geothermal Reservoir Engineering, Stanford University, Stanford, CA (2016).

Sparlin, M.A., Braile, L.W., and Smith, R.B.: Crustal structure of the eastern Snake River Plain determined from ray trace modeling of seismic refraction data: *Journal of Geophysical Research: Solid Earth*, **87**, (B4), (1982), 2619-2633.

Yilmaz, Ö.: Seismic data analysis: *Society of exploration geophysicists* (2001).